CHALMERS
UNIVERSITY OF TECHNOLOGY

Permanent magnet synchronous machine using ferrite vs rare earth magnets-how do they compare?

Master's thesis in Electric Power Engineering

Nikhil Manakshya, Praveena Pandurangan

DEPARTMENT OF ELECTRICAL ENGINEERING

CHALMERS UNIVERSITY OF TECHNOLOGY
Gothenburg, Sweden 2021
www.chalmers.se

Master's thesis 2021

Permanent magnet synchronous machine using ferrite vs rare earth magnets-how do they compare?

Nikhil Manakshya
Praveena Pandurangan

CHALMERS
UNIVERSITY OF TECHNOLOGY

Department of Electrical Engineering
Division of Electric Power Engineering
Chalmers University of Technology
Gothenburg, Sweden 2021

Permanent magnet synchronous machine using ferrite vs rare earth magnets-how do they compare?
Nikhil Manakshya and Praveena Pandurangan

Supervisor: Torbjörn Thiringer, Chalmers University of Technology and Bharadwaj Raghuraman, Volvo cars
Examiner: Torbjörn Thiringer, Chalmers University of Technology

Master's Thesis 2021
Department of Electrical Engineering
Division of Electric Power Engineering
Chalmers University of Technology
SE-412 96 Gothenburg
Telephone +46 31 772 1000

Typeset in LaTeX
Printed by Chalmers Reproservice
Gothenburg, Sweden 2021

Permanent magnet synchronous machine using ferrite vs rare earth magnets- how do they compare?
Nikhil Manakshya and Praveena Pandurangan
Department of Electrical Engineering
Chalmers University of Technology

Abstract

Permanent magnet synchronous machines (PMSM) are considered as viable options for automotive and traction applications. Rare earth magnets such as Neodymium Iron Boron (NdFeB) is the most common choice in the PMSM for electric vehicles in order to achieve high power density machines. However, rare earth magnets are problematic from ethical and sustainability perspectives. From these perspectives, there are better magnet alternatives, such as ferrites. Ferrite magnets on the other hand are known to have lower environmental impact, lower cost, and exist in abundance. Due to a lower residual flux density of a ferrite magnet than that of a rare earth magnet, a larger amount of ferrite magnets are needed to achieve the same performance.

This master thesis is aimed to compare a PMSM using NdFeB magnets with a PMSM using ferrite magnets in terms of different performance parameters such as torque production, power factor, drive cycle efficiency, losses, cost, and environmental impact. The machines are designed based on the Volvo XC40 vehicle requirements.

In order to make a comparison, ferrite based machines with various types of rotor structures, such as arc and spoke type configurations, are designed in Ansys Maxwell and compared with the reference PMSM holding NdFeB magnet. A demagnetisation study was performed on the ferrite magnets at lower temperatures in order to investigate the feasibility of the design. In order to reduce the risk of demagnetisation, a parametric analysis of the rotor structure has been conducted. Furthermore, the mechanical integrity was investigated at top speed.

Keywords: Vehicle requirements, drive cycle, design of electric machine using ferrites, different rotor structure, demagnetisation, cost comparison, environmental impacts.

Acknowledgements

We would like to articulate our deepest gratitude to our supervisor and examiner Prof.Torbjörn Thiringer and Luca Peretti for believing in us and providing us a support for the completion of the project. We would like to thank Bharadwaj Raghuraman and Mats Leksell for sharing their valuable knowledge and comments. We would also like to express gratefulness to all Ph.D student of electrical department, Anders Thulin, Per Rundbom, and Viktor Briggner for their help and guidelines. Finally, We would like to take this opportunity to thank our family and friends for their support and encouragement through out this project.

Nikhil Manakshya and Praveena Pandurangan,
Gothenburg, June 2021

Nomenclature

α Angle of inclination of the road

β_s Torque angle

δ_s Load angle

γ_s Current angle

μ_0 Magnetic permeability of free space

μ_{r} relative permeability

ψ_s Flux linkage phasor

$\psi_{1,\mathrm{PM}}$ Peak PM flux linkage

$\psi_{abc,PM}$ permanent magnet flux linkage in abc phase

ψ_d d axis flux linkage

ψ_{PM} Permanent magnet flux linkage

ψ_q q axis flux linkage

ρ Density of air

ρ_{cu} Resistivity of copper

τ_p Winding pole pitch length

θ_{dq} Current angle

θ_r Rotor angle

φ_s Power factor angle

ξ Saliency ratio

a Semi major axis

A_{cu} Cross-sectional area of a copper conductor

b Semi minor axis

B_{max} Maximum amplitude of the flux density

C_D Aerodynamic drag coefficient

d_{ext} End winding overhang length

f Electrical frequency

F_{acc} Acceleration force

F_L Air resistance force

F_{rb} Rolling resistance force of the rear

F_{rf} Rolling resistance force of the front tyre

f_r Rolling coefficient of the wheel

$F_{traction}$ Traction force

F_{xb} Net propulsion force provided by the EM on rear tyre

F_{xf} Net propulsion force provided by the EM on front tyre

H_c coercivity of the magnet

I rms phase current

i_d d-axis inductance

i_q q-axis inductance

i_{d0} center of the voltage ellipse

i_{max} Maximum current flow from inverter

K_c Classical eddy coefficient

K_e Excess or anomalous eddy current coefficient due to magnetic domains

K_h Hysteresis coefficient

K_A Axial scaling factor

K_R Radial scaling factor

K_W Winding factor

L_d	d-axis inductance
L_q	q-axis inductance
L_{abc}	Inductance matrix of abc phase
l_{stk}	Stack length
L_{coil}	Average length of a coil
N_1	Normal force acting on the front tyres
N_2	Normal force acting on the rear tyres
n_s	Number of turn of the conductor
p	No. of pole
p_{loss}	Power loss
q_s	Number of stator slot/pole/phase
R_s	Stator resistance
T_e	Net torque
u_s	Voltage phasor
v	Air velocity(vehicle + wind)
v_{dc}	Dc bus voltage
$v_{a,n}$	a phase voltage
$v_{b,n}$	b phase voltage
$v_{c,n}$	c phase voltage
v_d	d axis voltage
v_{max}	Peak phase voltage
v_q	q axis voltage
w	electrical speed

Contents

1

Introduction

1.1 Introduction

Electrical machines have been around for centuries. They have been used extensively in many applications such as pumps, fans, power generation etc. But in recent years they have gained popularity in their usage in the automotive industry. Emissions from combustion engine causes numerous problems including lung diseases, global warming, pollution, etc. that possess serious health challenges for the future generation. The depleting natural reserves of gas and oil is also one of the major drivers of the change from a combustion engine to an electric machine in vehicles. The electric machines are highly efficient when compared to an internal combustion engine, with an efficiency as high as 95% for some machines. Almost all automotive manufacturers have decided to electrify their vehicles in the coming years. This has lead to an increased demand for electric machines. Recently permanent magnet synchronous machines (PMSMs) containing rare earth magnets have gained popularity for electric and hybrid vehicles. Interior permanent magnet synchronous machines use rare earth magnets which have some advantages, such as wide speed range, high torque and power density, high efficiency, etc. Due to fluctuation in the price of rare earth magnets and mining issues, it would be desirable electrical machines could be designed with less or no magnets in traction applications [1]. The switched reluctance motor is one of the alternative EMs without magnets, however it has some disadvantages of having low power factor, vibration and noise. Another alternative is the synchronous reluctance machine which is also magnet free but its torque, power and power factor are inferior as compared to the PMSM. In order to obtain similar performance as the PMSM, a sufficient amount of permanent magnets are added to the synchronous reluctance machine, thereby improving the torque and power density, giving a permanent magnet assisted synchronous reluctance machine(PMAsyRM). By using low cost magnets such as ferrites in the PMAsyRM, the rotor structure is altered to achieve high torque, power, efficiency and a wide speed range in EV applications. However, the ferrite magnet based EM is reported to be sensitive to irreversible demagnetisation in cold conditions as well as a difficulty to maintain the mechanical strength of the rotor at maximum speed [2].

1.2 Background

Rare earth magnets such as Neodymium Iron Boron (NdFeB) is the most common choice in the PMSM for electric vehicles to achieve high power density machines. However, rare earth magnets are problematic from ethical and sustainability perspectives. From these perspectives, there are better magnet alternatives, such as ferrite magnet. Ferrite magnets are well known for lower environmental impact, abundance, low eddy current losses in low frequency application and low cost[2]; however, they have less BH energy than the rare earth magnets. In order to get the same performance as with NdFeB magnets, more ferrite magnets can be used.

In the reference PMSM, the rotor is magnetised using interior rare earth magnets. Due to increase in the price of rare earth magnets and environmental impact, it has become interesting to investigate other types of magnets that are less expensive and sustainable. One of the possibilities is using ferrite magnets, which will be investigated in this project. Replacing NdFeB magnets with ferrite magnets will require a new design of the rotor. The ferrites have lower remanence flux density and lower coercivity than NdFeB magnets. The location of permanent magnets can be chosen according to the requirements of the application. The surface mounted magnets are a good choice for application with fast dynamic response and high overload torque requirement. Interior magnet machines have advantage over rotor surface magnet machine in the field weakening mode[2]. The possible configurations of rotor structure is the arc type configuration having different number of flux barrier and the spoke type configuration. The spoke type configuration has large magnets with alternating tangential magnetisation, i.e. the same magnet poles face each other. This allows the flux from a large area of the PM to be directed into a rotor pole, i.e. flux concentration can be acheived. The arc type configuration is different from the spoke machine since it uses many barriers along the d-axis flux path to actively utilize the reluctance torque.

1.3 Research questions

The purpose of this thesis is to compare a NdFeB based PMSM with a ferrite magnet machine in terms of machine performance parameters and the vehicle performance. The losses are mapped for the entire speed range of the electric machine and again compared from an efficiency point of view. This thesis investigates if a ferrite machine is capable of replacing a NdFeB machine. Several research papers are available that explain the design procedure of the rotor in order to increase the reluctance torque but insufficient information is available in terms of how a ferrite magnet machine compares with a rare earth magnet based machine for traction application.

Different barrier shapes such as arc, spoke, banana, V-shape, etc. has to be considered and for some chosen geometries, a deeper evaluation is to be done. Also, the machine parameters are to be extracted and a control strategy is to be designed for controlling the PMaSynRM, which is built in Ansys Maxwell.

2

Theory

In Chapter 2, the theory behind working of PMSM machines will be presented. All the parameters that is necessary to understand the results of this thesis will be discussed in this chapter.

2.1 Drive cycle

The drive cycle is the velocity profile of the vehicle with respect to time. It is often standardised according to different regions and driving conditions. The velocity profile for different drive cycles is the representation of different road conditions. Maximum required vehicle speed and acceleration is used for sizing of an electric powertrain. One must design an EM that can fulfill all the demanded requirements.

2.2 Vehicle dynamics

Vehicle dynamics is the study of the vehicle behaviour in the longitudinal and lateral direction. The vehicle parameters that are used to study the longitudinal dynamics includes vehicle velocity, acceleration, and resistive forces. These parameters are dependent on several other components of the vehicle such as tyres, aerodynamics, motors, gearbox, etc.

To meet the requirement on the speed and torque needed for the motor, a powertrain simulation is needed to be performed. The input to the simulation is the required velocity of the vehicle. The velocity can be given as a standard drive cycle or from a reference velocity generator. The reference velocity generator is the velocity profile of the vehicle given its maximum acceleration and deceleration. The reference velocity demanded by the user can now be converted in the form of torque requirement and subtracted from the resistive forces to get the required vehicle performance. The EM must fulfill this torque requirement. The torque is required by the vehicle to accelerate and to overcome the rolling resistance, drag resistance, and road gradient forces. These forces are shown in Fig.2.1 where F_{rf} and F_{rb} are the rolling resistance forces of the front and the rear tyre, F_L is the air resistance force, N_1 and N_2 are the normal forces acting on the front and the rear tyres, F_{xf} and F_{xb} are the net propulsion forces provided by the EM, m is the vehicle mass, and α is the angle of inclination of the road.

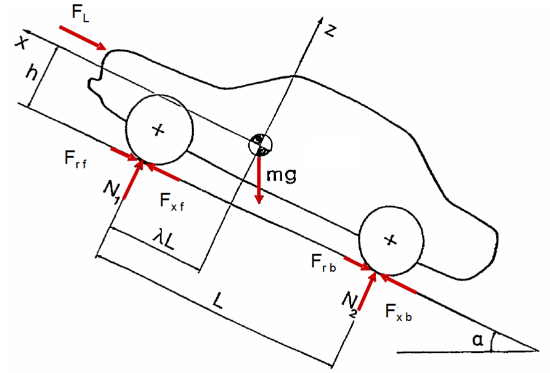

Figure 2.1: Forces acting on a vehicle

2.2.1 Rolling resistance

Rolling resistance is caused by the deformation of the tyre when the vehicle is in motion. One side of the tyre get compressed while the other side get decompressed when the wheel rotates. This phenomenon creates resistance in the vehicle motion. The rolling resistance force is described as

$$F_r = mgf_r \cos\alpha \tag{2.1}$$

where m is the mass of the vehicle, and f_r is the rolling coefficient of the wheel..

2.2.2 Air resistance

The force experienced by the vehicle due to the air drag during its motion is known as the air resistance force. It is given by

$$F_L = \frac{1}{2}\rho v^2 C_D A \tag{2.2}$$

where ρ is the density of air, v is the air velocity (vehicle + wind), C_D is the aerodynamic drag coefficient, and A is the frontal area.

2.2.3 Gradient force

When the vehicle is driven in a road that has some inclination, it experiences a force component in the direction opposite to its motion due to its own weight. This force is expressed as

$$F_a = mg \sin \alpha \tag{2.3}$$

2.2.4 Acceleration force

This force is one of the major factor in the sizing of an electrical machine and describes the dynamics of the vehicle. Higher the acceleration requirement from a vehicle, higher will be the power requirement from the EM. The acceleration force is expressed as

$$F_{acc} = m\frac{dv}{dt} \tag{2.4}$$

2.2.5 Traction force

Calculation and measuring of the motion resistance and its components is the basis to map a vehicles performance properties. From (2.1-2.3), the equation of motion of the vehicle can be expressed as

$$F_{traction} = F_{acc} + F_a + F_L + F_r \tag{2.5}$$

This traction force is the force required to be produced by the EM.

2.3 Permanent magnet synchronous machine

2.3.1 Equivalent circuit of PMSM

The PMSM is mainly studied in the dq system. The advantage of the dq axes system is that it is a stationary axis system with respect to the rotating vector. The d-axis of the rotor as per definition is aligned with the d-axis of stator (see Fig.2.2). This axis is responsible for the magnetisation of the rotor while the q axis is the quadrature axis of the rotor and produces the PM torque.

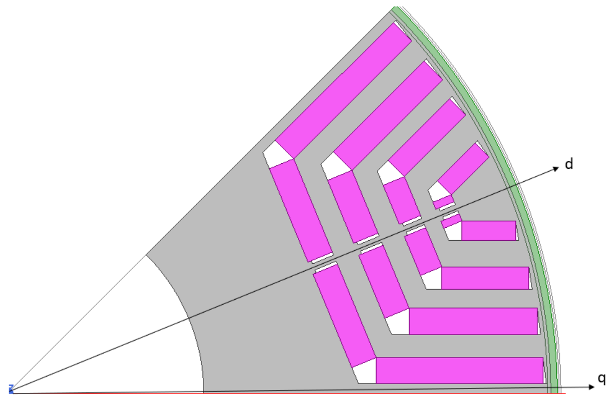

Figure 2.2: dq axes of a PMSM

The physical quantities such as current, voltage, flux linkage, etc. can be transformed to the $alpha - beta$ system and then it can be converted to the dq system. A transformation matrix that allows the transformation between the abc system to the dq system is

$$\mathrm{T}_{dq0,abc} = \frac{2}{3}\begin{bmatrix} \cos\left(\frac{p\theta_r}{2}\right) & \cos\left(\frac{p\theta_r}{2} - 2\pi/3\right) & \cos\left(\frac{p\theta_r}{2} + 2\pi/3\right) \\ -\sin\left(\frac{p\theta_r}{2}\right) & -\sin\left(\frac{p\theta_r}{2} - 2\pi/3\right) & -\sin\left(\frac{p\theta_r}{2} + 2\pi/3\right) \\ 1/2 & 1/2 & 1/2 \end{bmatrix}$$

where θ_r is the rotor angle, p is the number of pole. This mean that the dq current is $\mathbf{i}_{dq0} = \mathbf{T}_{dq0,abc}.\mathbf{i}_{abc}$ where $\mathbf{i}_{dq0} = [i_d i_q i_0]^T$ and dq voltage is $\mathbf{v}_{dq0} = \mathbf{T}_{dq0,abc}\mathbf{v}_{abc}$ where $\mathbf{v}_{dq0} = [v_d v_q v_0]^T$.

The voltage equation of the machine is

$$\mathbf{v}_{abc} = R_s\mathbf{i}_{abc} + \frac{d\boldsymbol{\psi}_{abc}}{dt} = R_s\mathbf{i}_{abc} + \frac{d}{dt}\left(\boldsymbol{\psi}_{abc,PM} + \mathbf{L}_{abc}\mathbf{i}_{abc}\right) \tag{2.6}$$

where $\mathbf{v}_{abc} = [v_{a,n} v_{b,n} v_{c,n}]^T$, $v_{a,n}$, $v_{b,n}$ and $v_{c,n}$ are the phase voltages of a, b, and c phases respectively, R_s is the stator resistance, $\psi_{abc,PM}$ is the permanent magnet flux linkage in abc phases, L_{abc} is the inductance matrix.

After converting (2.6) from abc to dq system it can be expressed as

$$\mathbf{v}_{dq0} = R_s\mathbf{i}_{dq0} + \mathbf{T}_{dq0,abc}\frac{d}{dt}\left(\boldsymbol{\psi}_{abc,\mathrm{PM}} + \mathbf{L}_{abc}\mathbf{T}^{-1}_{dq0,abc}\mathbf{i}_{dq0}\right) \tag{2.7}$$

and after some simplification it can be expressed as

$$\begin{aligned} v_d &= R_s i_d + \tfrac{d\psi_d}{dt} - \omega\psi_q \\ v_q &= R_s i_q + \tfrac{d\psi_q}{dt} + \omega\psi_d \end{aligned} \tag{2.8}$$

where $\psi_d = \psi_{1,\mathrm{PM}} + L_d i_d$, $\psi_q = L_q i_q$, and $\psi_{1,\mathrm{PM}}$ is the peak PM flux linkage. The equivalent circuit corresponding to (2.8) is shown in Fig. 2.3.

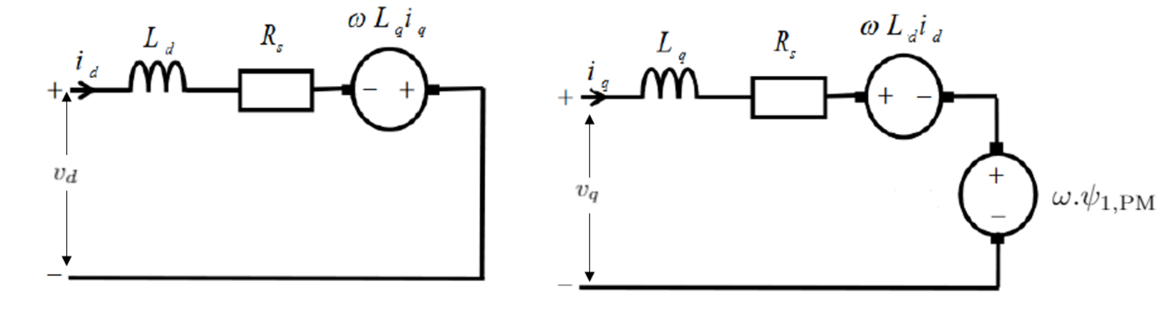

(a) d - axis equivalent circuit (b) q - axis equivalent circuit

Figure 2.3: equiv. circuits for d and q axes in a PMSM

2.3.2 Voltage and current limitation

The motor is supplied with a three phase voltage from the inverter. The voltage and current limitation from the inverter can be expressed as

$$\sqrt{v_d^2 + v_q^2} \leq \frac{v_{\mathrm{dc}}}{\sqrt{3}} \tag{2.9}$$

$$\sqrt{i_d^2 + i_q^2} \leq i_{max} \tag{2.10}$$

where v_{dc} is the maximum dc voltage from the battery, $\frac{v_{\mathrm{dc}}}{\sqrt{3}}$ is the maximum peak phase voltage, and i_{max} is the maximum current from inverter.

When (2.8) is substituted into (2.9), a voltage ellipse can be dervied and expressed as

$$\begin{aligned} \frac{(i_d - i_{d0})^2}{a^2} + \frac{i_q^2}{b^2} &= 1 \\ a &= \frac{v_{max}}{\omega_r L_d} \\ b &= \frac{v_{max}}{\omega_r L_q} \\ i_{d0} &= -\frac{\psi_{PM}}{L_d} \end{aligned} \tag{2.11}$$

where a is the semi major axis, b is the semi minor axis, i_{d0} is the center of the ellipse. (2.10) and (2.11) defines the basis for the motor control strategy.

2.3.3 PM torque and reluctance torque

The torque produced by a PMSM is the combination of PM torque and reluctance torque. The torque equation is written as

$$T_e = \frac{3p}{4} \left(\psi_{1,\mathrm{PM}} i_q + (L_d - L_q)\, i_d i_q \right) \tag{2.12}$$

where the first term of (2.12) is the PM torque while the second term is the reluctance torque. The PM torque is produced by the q-axis current and magnet flux. So the machines having higher PM flux linkage can produce a higher PM torque. The reluctance torque contribution comes from the difference in the d and q axes inductance. From Figure 2.2, it can be noticed that the magnetic reluctance along the d axis is very low due to the introduction of the barriers while the inductance along the q axis is high.

The rotating current vector when resolved in the d and q axes, it can be expressed as

$$\begin{aligned} i_d &= i_{max}\cos(\theta_{dq}) \\ i_q &= i_{max}\sin(\theta_{dq}) \end{aligned} \tag{2.13}$$

where θ_{dq} is the current angle. When (2.13) is substituted in (2.12), we get

$$T_e = \frac{3p}{4}\left(\psi_{1,\mathrm{PM}} i_{max}\sin(\theta_{dq}) + (L_d - L_q)\, i_{max}^2 \sin(\theta_{dq})\cos(\theta_{dq})\right) \tag{2.14}$$

A typical behaviour of the torque curve with the current angle for nominal current is shown in Fig.2.4.

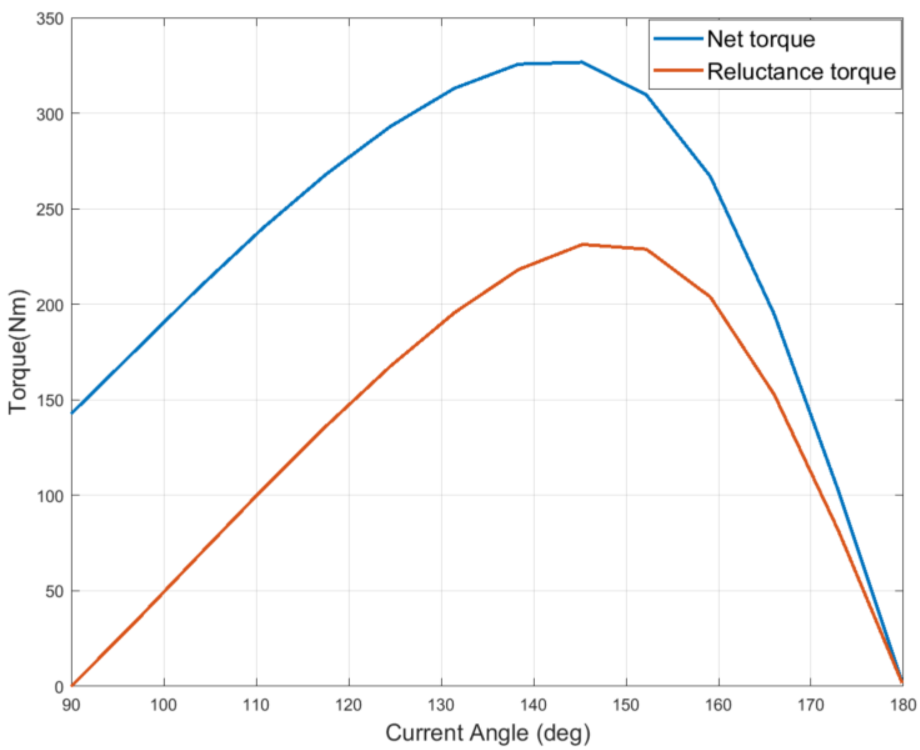

Figure 2.4: Net torque and reluctance torque of the PMSM

2.4 PMSM control strategy

To drive the motor without damaging any component of the drivetrain and to utilize the maximum possible torque for the supplied current, Maximum Torque Per Ampere (MTPA) and a field weakening strategy of the motor is needed. The MTPA control strategy tries to minimize conduction losses below the base speed while the field weakening strategy ensures the safe operation of the machine above the base speed.

2.4.1 Maximum Torque Per Ampere (MTPA)

MTPA is the control strategy used in the region before the base speed of the machine. Fig.2.5 shows the MTPA control strategy.

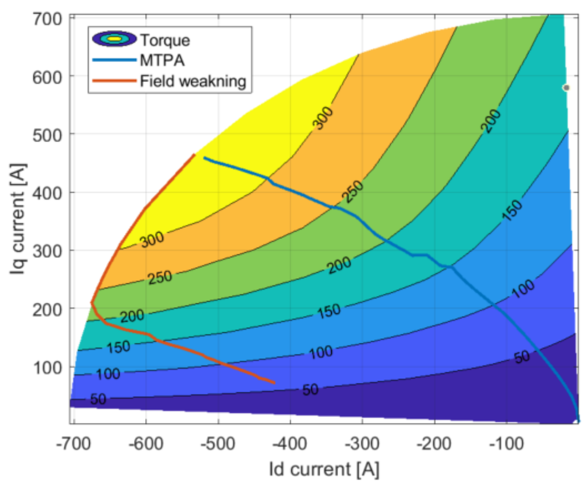

Figure 2.5: MTPA control strategy

The contour plots represents the torque obtained at different current magnitudes. This current magnitude is chosen such that a minimum possible current is used to produce required torque. The minimum current magnitude is obtained at certain current angle, also known as MTPA current angle. The effect of current magnitude and current angle on torque production is also evident from (2.14). Equation (2.14) can be differentiated to calculate the optimal current angle for a given magnitude of current such that the maximum torque is obtained

$$\cos\theta_{dq} = \frac{\psi_{1,\mathrm{PM}}}{4\,(L_d - L_q)\,i_{max}} - \sqrt{\frac{1}{2} + \left(\frac{\psi_{1,\mathrm{PM}}}{4\,(L_d - L_q)\,i_{max}}\right)^2} \tag{2.15}$$

2.4.2 Field weakening

The field weakening strategy is applied after the inverter has reached its voltage limitation. The voltage is then maintained constant by increasing the magnitude of the d axis current such that it counteracts the increase in the back emf. This phenomenon can be observed from the equivalent circuit shown in Fig 2.3,(b). The back emf ($w\psi_{1,\mathrm{PM}}$) increases with the speed of the machine while the increased d axis current counteracts the increase in the back emf.

Once the current limit can no longer be maintained due to very high speed of the machine, Maximum Torque Per unit Voltage (MTPV) strategy is used. At this speed the voltage ellipse becomes very small and the operating point of the machine enters inside the current circle as shown in Fig 2.5. A voltage ellipse describing the mentioned theory is shown in Figure 2.6.

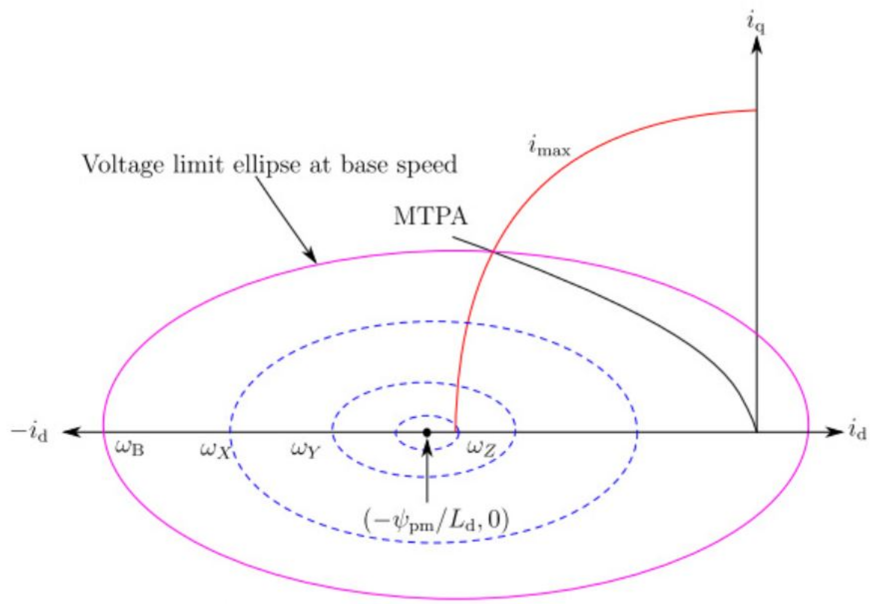

Figure 2.6: Voltage ellipse and current circle

2.5 Power factor and saliency ratio

The saliency ratio is a very important parameter for a PMSM. It is defined as

$$\xi = \frac{L_q}{L_d} \tag{2.16}$$

It was shown in [3] that with the increase in the saliency ratio of the machine, the power factor of the machine also increases. To increase the saliency ratio of the machine, the insulation ratio plays an important role. The insulation ratio is the ratio of amount of air to the amount of iron.

Based on (2.8), a phasor diagram can be made and it is shown in Fig.2.7 where β_s is the torque angle, ψ_s is the flux linkage phasor, i_s is the current phasor, u_s is the voltage phasor, δ_s is the load angle, γ_s is the current angle, and φ_s is the resulting angle between the current and voltage phasor.

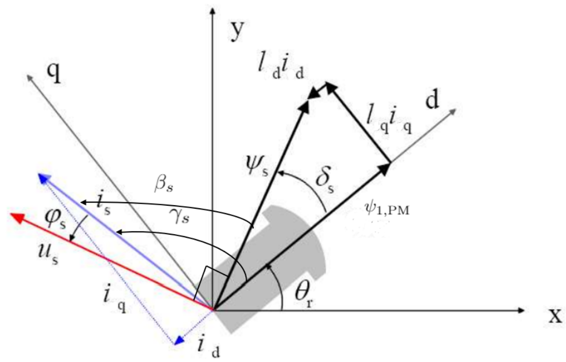

Figure 2.7: Phasor diagram for a PMaSynRM

It can be realised from Fig.2.7 that having good PM flux linkage increases the power factor. This is one of the reason why PMSM is preferred over SynRM. From Fig.2.7 the following relations holds true for the defined angles,

$$\begin{aligned} \tfrac{\pi}{2} + \delta_s &= \gamma_s + \varphi_s \\ \gamma_s &= \beta_s + \delta_s \end{aligned} \tag{2.17}$$

Using (2.17), we can write power factor as

$$\begin{aligned} PF &= \cos \varphi_s \\ \varphi_s &= \tfrac{\pi}{2} + \delta_s - \gamma_s \\ PF &= \cos\left(\tfrac{\pi}{2} + \delta_s - \gamma_s\right) \\ \tan\left(\tfrac{\pi}{2} + \delta_s - \gamma_s\right) &= \cot(\gamma_s - \delta_s) \end{aligned} \tag{2.18}$$

$\cot(\gamma_s - \delta_s)$ can be written as

$$\cot(\gamma_s - \delta_s) = \frac{\cot \gamma_s \cot \delta_s + 1}{\cot \delta_s - \cot \gamma_s} \tag{2.19}$$

where $\cot \gamma_s = \frac{i_d}{i_q}$ and $\cot \delta_s = \frac{\psi_{1,\mathrm{PM}} + L_d i_d}{L_q i_q}$. Substituting the value of $\frac{\pi}{2} + \delta_s - \gamma_s$, the power factor is obtained as

$$PF = \cos\left(\arctan\left(\frac{\frac{\psi_{1,\mathrm{PM}} + L_d i_d}{L_q i_q} + \frac{i_q}{i_d}}{\frac{\psi_{1,\mathrm{PM}} + L_d i_d}{L_q i_d} - 1}\right)\right) \tag{2.20}$$

2.6 Magnet characteristics

A permanent magnet contains several magnetic domains as shown in Fig 2.8.

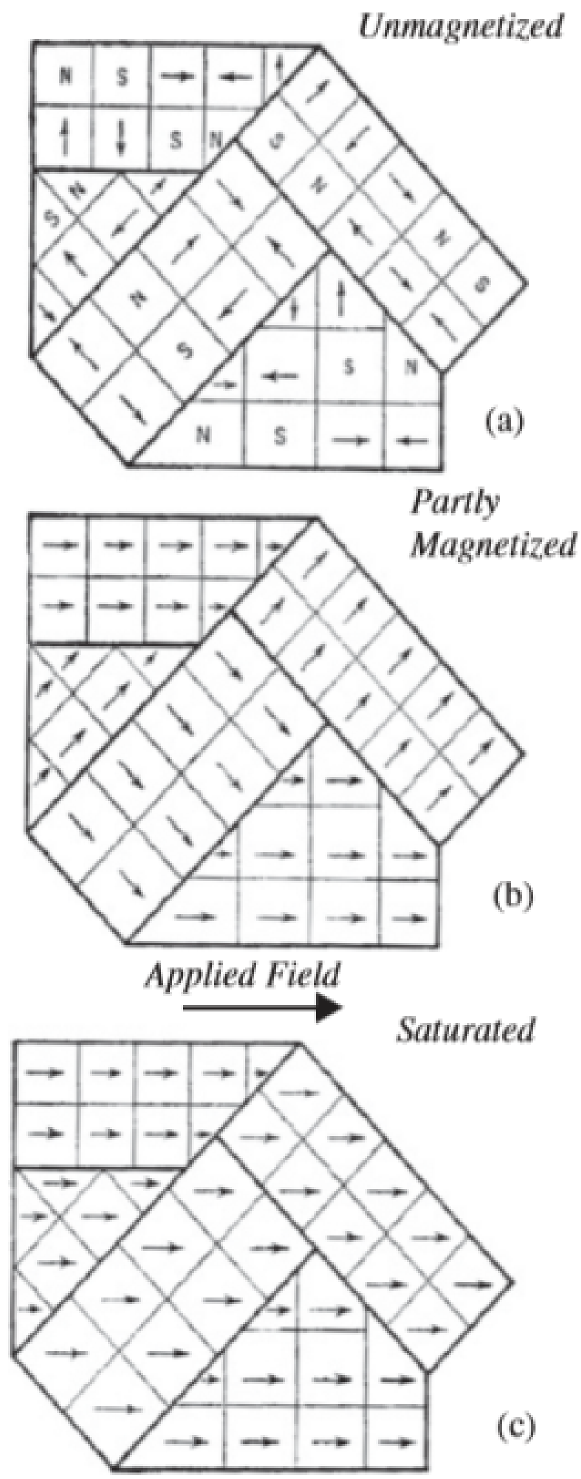

Figure 2.8: Successive stage of magnetisation of a PM [4]

The domains are aligned in random manner in Fig 2.8(a) where they cancel the magnetic field of each other resulting in a net zero magnetic field. In Fig 2.8(b) when an external field is applied, some of the domains get aligned in the direction of the field while others don't. Finally in Fig.2.8(c) all the domains gets aligned when a large external magnetic field (H) is applied and the magnet gets saturated.

The magnetic flux density depends on magnetic field intensity as

$$\boldsymbol{B} = \mu_0 \mu_\mathrm{r} \boldsymbol{H} \tag{2.21}$$

where μ_0 is the magnetic permeability of free space and μ_r is the relative permeability. A typical BH curve for a permanent magnet is shown in Fig.2.9.

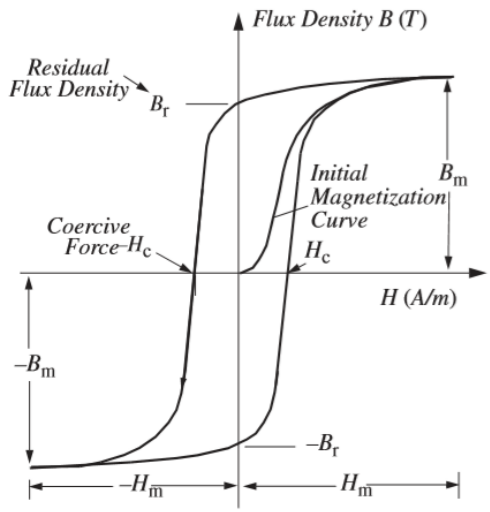

Figure 2.9: Hysteresis loop [4]

If the applied field to the specimen is first increased until saturation and then decreased, the flux density (B) decreases but it lags behind the applied magnetic field. When the applied magnetic field (H) reaches zero, all the magnetic domains are unable to retain their original orientation and a net magnetic flux density is left in the magnet. This value of B when H is zero is known as the remanence or residual flux density.

The phenomenon of B field lagging behind H field is known as hysteresis. At the point of coercivity (H_c) the magnet is susceptible to irreversible demagnetisation.

2.7 Short-circuit current and demagnetisation

The PMSM is the preferred choice over the induction machines because the conduction losses in the rotor is eliminated. However, PM machines are subjected to irreversible demagnetisation under short-circuit conditions. Some parts of the magnets get permanently demagnetised if the magnet experience the magnitude of magnetic field intensity higher than its coercivity value. The magnitude of the short-circuit current that will be generated during the short-circuit can be calculated by substituting v_d and v_q as zero in (2.8) such that

$$\begin{aligned} R_s i_d + \frac{d\psi_d}{dt} - \omega\psi_q = 0 \\ R_s i_q + \frac{d\psi_q}{dt} + \omega\psi_d = 0 \end{aligned} \tag{2.22}$$

For steady state condition, the change in d and q axes flux linkage is zero. The magnitude of steady state short-circuit current is

$$\begin{aligned} i_d = \frac{\omega^2\psi_{1,pm}L_q}{R_s^2+\omega^2 L_d L_q} \\ i_q = \frac{\omega\psi_{1,pm}R_s}{R_s^2+\omega^2 L_d L_q} \end{aligned} \tag{2.23}$$

To calculate the transient short-circuit current, PM flux linkage, d axis inductance, and q axis inductance is assumed to be constant. Substituting the d and q axes flux linkage in (2.22), we get

$$\begin{aligned} \dot{i_d} = \frac{wL_q i_q - R_s i_d}{L_d} \\ \dot{i_q} = -\frac{wL_d i_d + R_s i_q + w\psi_{1,pm}}{L_q} \end{aligned} \tag{2.24}$$

This equation can be solved in MATLAB with the help of an ODE solver to get the result for the transient short-circuit current. The demagnetisation of the magnets are affected mostly by the d axis current in the machine because the magnets are initially magnetised in the direction opposite to that of the negative d axis current. It was shown in [5] that when a negative d axis current is applied to the machine, the d axis flux linkage of the machine reduces and the magnetic domain of the magnets starts to change their direction of magnetisation. Fig 2.10 shows how the magnetic flux density vector reverse their direction based on the external magnetic field intensity. The red arrow shows the initial direction of the magnetic flux density vector when the external field is zero.

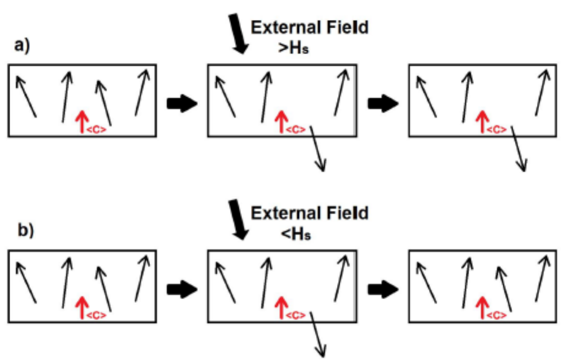

Figure 2.10: Sketch of the model: the arrows represent the magnetization of each magnet. (a) and (b) Condition of the magnet after initial saturation. Then, (a) shows the application of a demagnetizing field $H_{ext} > H_S$, while (b) shows a demagnetizing field $H_{ext} < H_S$. [5]

In Fig 2.10(a), the applied external field is high enough to induce an irreversible rotation of some domains, while this does not occur in (b). The magnetic field intensity at which irreversible demagnetisation occur is known as the knee point of the magnet in the B-H curve. For ferrite magnet the knee point value increases with the temperature meaning that it is more difficult to demagnetise a ferrite magnet at high temperature while the case is opposite for NdFeB magnets.

2.8 Losses in the electrical machine

The major losses in the EM is copper (conduction) and core losses. conduction losses comes mainly from copper winding while the core losses comes from the steel lamination in the machine. Steel laminations are axially stacked together in smaller thickness to minimize core losses. Core loss comprise of eddy current and hysteresis loss. The phenomenon of hysteresis was explained in section 2.6.

To calculate conduction loss, the resistance of the machine/phase is calculated. Fig.2.11 depicts a general circuit for a single phase of the machine where c_s denote the number of parallel branches of each phase, and $\frac{p}{2c_s}$ denote number of series connected pole pairs.

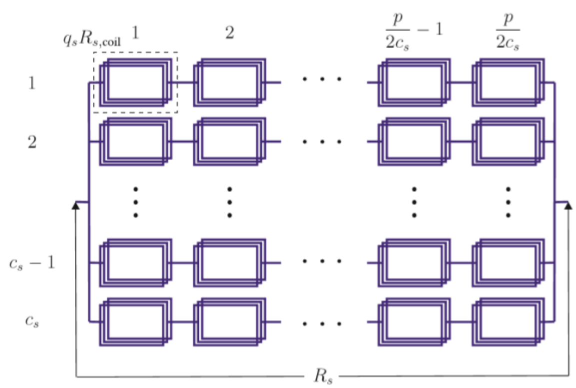

Figure 2.11: General stator winding arrangement for phase A of a Y connected coils

For a 8 pole machine and 4 parallel path, one will have 1 series connected pole pair/phase. To calculate the resistance of the phase winding, initially the resistance of the series connection and then the resistance of the parallel connection can be calculated. The resulting resistance formula obtained is

$$R_s = \frac{\rho_{\text{cu}} p n_s q_s L_{\text{coil}}}{2A_{\text{cu}} c_s^2} \tag{2.25}$$

where L_{coil} is the average length of a coil , A_{cu} is the cross-sectional area of a copper conductor and ρ_{cu} is the resistivity of copper, n_s is the number of turn of the conductor, and q_s is the number of stator slot/pole/phase. The average length of the coil is a combination of stack length and overhang length. The procedure to calculate the average coil length was found in [6] as

$$L_{coil} = 2\left(l_{\text{active}} + l_{\text{passive}}\right) = 2\left(l_{stk} + 1.2\tau_p + 2d_{ext}\right) \tag{2.26}$$

where l_{stk} is the stack length, τ_p is the winding pole pitch length, and d_{ext} is the end winding overhang length. The conduction loss formula can be expressed as

$$P_{cu} = 3I^2R_s \tag{2.27}$$

where I is the rms phase current.

3

Method of Analysis

The method of analysis adopted in this thesis is inspired by self-thinking, reviewing different research papers, and also weighting of the advantages and disadvantages of different methods. To design an electrical machine one needs to be sure about the requirements for a vehicle. Once the requirement of the vehicle is set, a reference machine with NdFeB is designed to meet requirements using MATLAB and Ansys Maxwell. Later, to design a ferrite magnet based machine, different rotor shapes were chosen keeping the same volume and same stator parameters as the reference machine. Once the rotor shapes were finalized, both the rotor and the stator were modelled in Ansys Maxwell and the machines were compared using different performance parameters.

3.1 Vehicle parameters

The vehicle parameters were inspired by Volvo XC40 Recharge [7] and they are shown in Table 3.1. Two electrical motors with the same specifications were used one at the front and one at the rear axles. The total installed output power in the vehicle is thus 320 kW. One of the performance requirement of the vehicle is 0 to 100 km/h in 4 *sec*. A MATLAB model was further developed that involves a reference velocity generator, velocity controller, motor model, and vehicle dynamics model to verify that the requirements can be fulfilled. The model is shown in Appendix A.1 as Figures [A.1 -A.4].

Table 3.1: Vehicle parameters

Parameter	Value	Unit
Vehicle curb weight	2200	Kg
Rolling radius	0.31	m
Rolling resistance	0.009	
Coefficient of drag	0.39	
Front area	2.25	m^2
Air density	1.225	kg/m^3
Maximum vehicle speed	180	Km/h
EM base speed	4400	rpm
Peak torque	350	Nm
Mechanical power at base speed	160	kW
Gearbox ratio	10	
No. of electric motors	2	

3.2 Electrical machine sizing

To meet the vehicle requirement, the reference machine is scaled in the axial and radial direction with certain factors [8]. The given reference machine with NdFeB magnets has a peak torque of 320 Nm and peak power of 130 kW before scaling, and it was provided by Volvo Cars. The torque-speed map is shown in Figure 3.1.

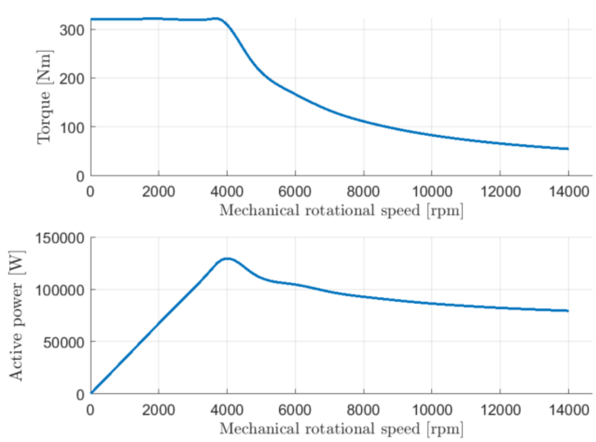

Figure 3.1: Reference machine max torque-speed and power-speed region before scaling

To scale the machine, a scaling methodology provided by Volvo Cars was used that requires certain user input such as RMS current, DC bus voltage, radial scaling factor(K_R), axial scaling factor(K_A) and winding factor(K_W)

$$K_A = \frac{L_{new}}{L_{ref}} \tag{3.1}$$

$$K_R = \frac{S_{new}}{S_{ref}} \tag{3.2}$$

$$K_W = \frac{\frac{N}{c_s}}{\frac{N_o}{c_{so}}} \tag{3.3}$$

where L_{new} is stack length of the new machine, L_{ref} is stack length of the reference machine, S_{new} is cross section dimension of the new machine, S_{ref} is cross section dimension of the reference machine, N is number of turns of the new machine, c_s is number of parallel branches of the new machine, N_o is number of turns of the reference machine, and c_{so} is number of parallel branches of the reference machine. This input is used to modify the existing data in order to scale the machine.
This is an iterative process by which a suitable machine size was obtained with an RMS current of 500 A and a DC bus voltage of 400 V. In addition to this quantity, the axial and radial scaling constants were set to 1.2. The winding factor is set as 0.8 for the field weakening region to start around 4400 rpm as stated in section 3.1. The rotor and stator parameters are listed in Table 3.2.

Table 3.2: Design parameters

Parameter	Value	Unit
Axial length	162	mm
Stator outer diameter	252	mm
Rotor outer diameter	169.3	mm
Air gap length	1	mm
Peak current density	20	A/mm^2

Figure 3.2 represents the scaled reference machine which from here on will be referred to as the reference machine. More detailed stator parameters are presented in Appendix A.2 as Table A.1.

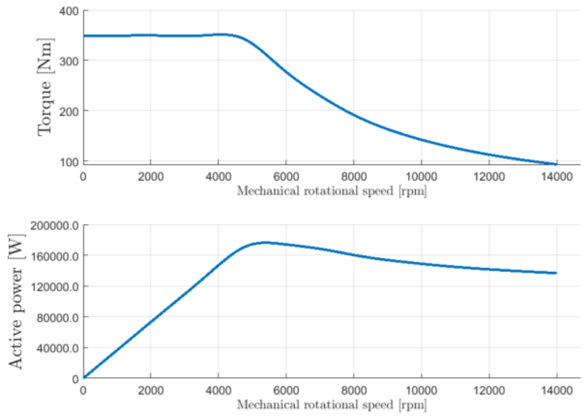

Figure 3.2: Reference machine max torque-speed and power-speed region after scaling

3.3 Electric machine FEM model

To study the resulting performance due to the electromagnetic design for the electrical machines, Ansys Maxwell and Motor-CAD are used as the preferred software in this thesis. The cross section of the reference electric machine is illustrated in Figure 3.3.

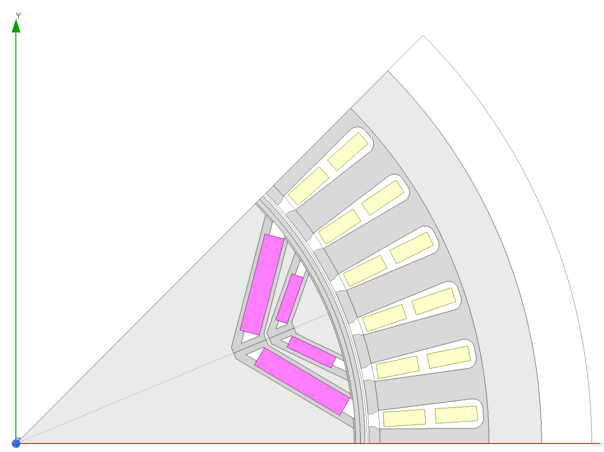

Figure 3.3: Reference machine

3.4 Selection of magnets

To select a ferrite magnet suitable for this thesis, the main criteria was high remanence flux density. Several ferrite magnets were compared, and the Y30BH and NMF12G magnets were found suitable. The properties of the ferrite magnets and NdFeB magnet are listed in Table 3.3. The BH curves at different temperatures are shown in Figure 3.4. The ferrites magnets are very sensitive to low temperature.

Table 3.3: Comparison of magnets

Series	Name	Provider	B_rema -nence (T)	Coercivity (kA/m)	Resistivity ($\Omega.m$)	Mass density (Kg/m^3)
NMF	NMF-12G	Hitachi Magnet	0.5	350	100	5000
C5	Y30BH	Eclipse Magnetic	0.38	223	1e5	5000
NEOMAX	Nd-Fe-B	Hitachi Magnet	1.4	912	1.6e-6	7700

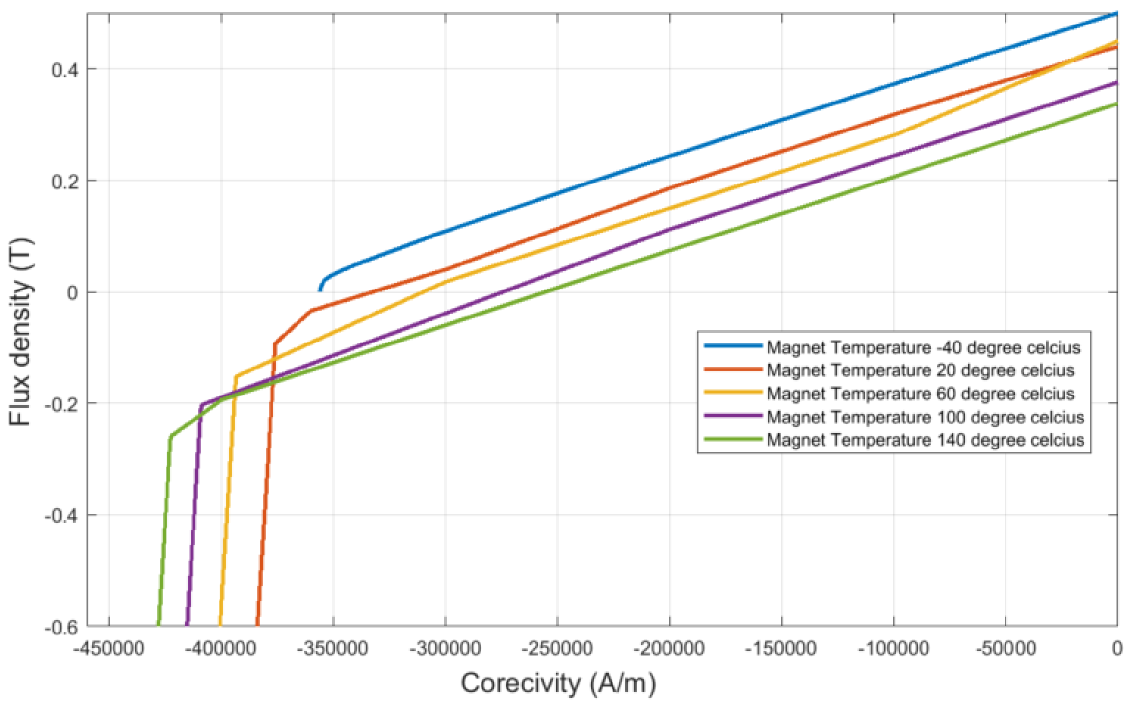

Figure 3.4: BH curve of NMF12G ferrite magnet at different temperature

3.5 Different types of rotor structure

Two different types of rotor structures are considered and designed using ferrite magnets in ANSYS Maxwell. The types of rotor structures are:

- Arc type configuration with three and four-layer barrier
- Spoke type configuration

The volume of the machine is fixed and it has the same stator structure as the reference machine but different rotor structures.

3.6 Arc type configuration

The arc type configuration is based on the insertion of different barriers in the rotor structure. Three different machines were used in [9] and the highest torque was obtained for the machine with 3-barriers because of high reluctance torque. In [9] the designed motor was able to achieve 85 % of the benchmark torque. To achieve the same torque value as the benchmark machine a 27% increase in machine volume was needed. It was also shown that the width of the barrier opening plays an important role for the torque ripple since the interaction of flux between the barrier opening, and stator teeth create harmonics.

In order to understand the barriers design and their influence on the machine, [10] was found to give very detailed information on the design procedure. A 3-layer design was considered and a number of different parametric sweeps were performed for the rotor. It was shown in [10] that having more number of barriers increases the net torque as a result of higher PM flux linkage.

Finally, in [11] a comparison between three different traction motors was performed keeping the same stator. The selected motors used Nd(Dy)FeB, SmCo and Sr-ferrite type magnets in the respective machines. Following the recommendation in the paper and using initial rotor data as stated in Table 3 in [11], an initial rotor geometry having 3-layers was made in Motor-CAD for this thesis. The rotor geometry along with the name of its variables are presented in Figure 3.5 where B_1 is the length of the inner magnets of the first layer, W_1 is the thickness of the inner magnets of the first layer, W_{1O} is the thickness of the outer magnets of the first layer, L_1 is the distance of the magnets from the center of shaft of the first layer, L_{1O} is the length of the outer magnets of the first layer, L_{1b} is the tangential rotor bridge height of the first layer.

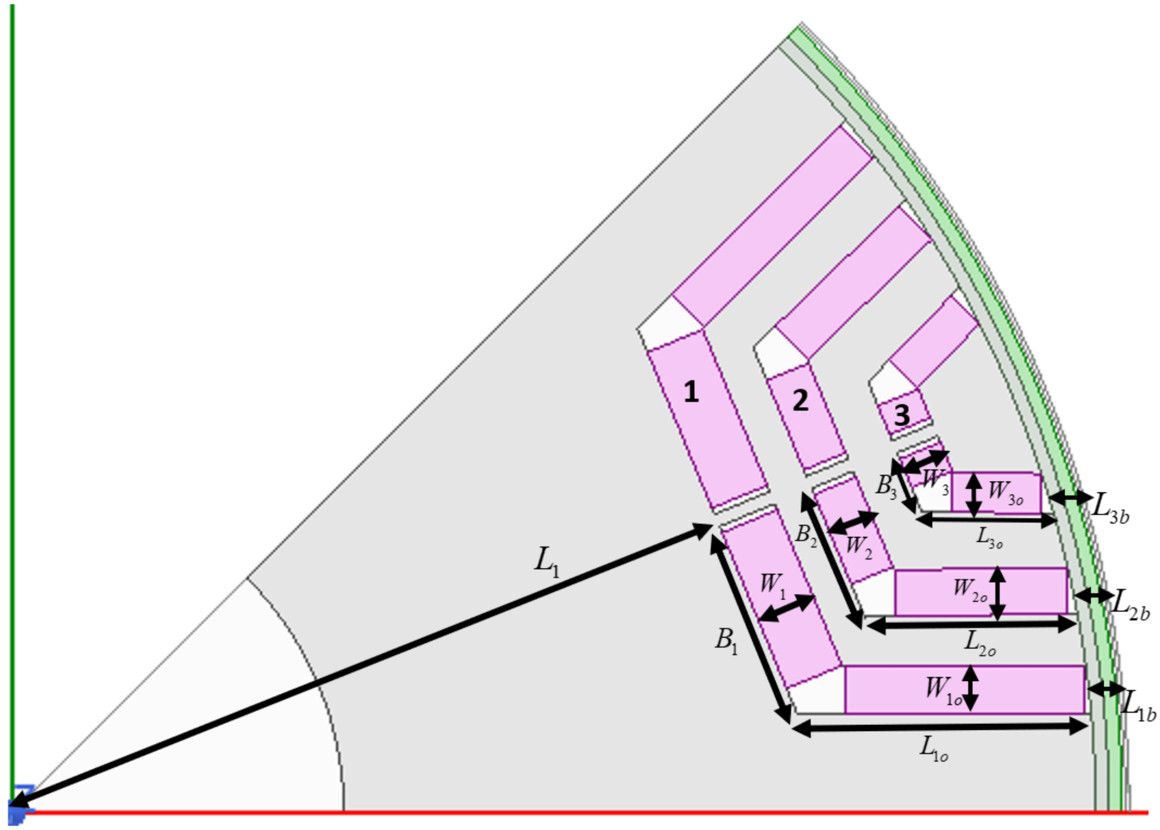

Figure 3.5: Rotor variable names for the 3-layer machine

The dimensions of the machine are listed in Table 3.4.

Table 3.4: Rotor dimension for 3 layer

Layer No.	Parameter	Value	Unit
	B_1	12.7	mm
	W_1	4.5	mm
1	W_{1O}	4.5	mm
	L_1	57.5	mm
	L_{1O}	18	mm
	L_{1b}	2	mm
	B_2	7.3	mm
	W_2	3.4	mm
2	W_{2O}	3.4	mm
	L_2	65	mm
	L_{2O}	13	mm
	L_{2b}	2	mm
	B_3	2.3	mm
	W_3	3.5	mm
3	W_{3O}	3.3	mm
	L_3	72	mm
	L_{3O}	6.7	mm
	L_{3b}	2	mm

From Figure 3.5, it can be seen that radial and tangential rotor bridges have been introduced in each layer. They are initially based on past experience for mechanical strength demands. The value for the radial ribs were chosen to be 1 mm while that for the tangential ribs were chosen to be 2 mm. The air gap that was initially chosen was 1 mm keeping in mind the maximum allowable air gap length. The magnets and the rotor steel will expand during the operation due to thermal expansion and it is necessary to have a sufficient gap between the rotor and the stator. It was understood that shorter the air gap length, higher is the output torque and hence the rotor geometry is subjected to change after the mechanical and thermal analysis.

Once the geometry of the rotor was finalised, it was exported to Ansys Maxwell and a simulation was performed to determine the peak torque of the machine. It was noticed that the 3-layer machine was able to generate 91 % of the peak reference torque.

3.6.1 Parametrization of rotor variables

As mentioned in section 3.6, the parameters chosen for the 3-layer machine are initial parameters and a parametric sweep will be needed in order to investigate the effect of the rotor geometry on the performance parameters. The rotor geometry that was initially exported from Motor CAD was a fixed geometry that could not be updated in Ansys Maxwell. Keeping this in mind a 4-layer geometry was built in Ansys Maxwell that allowed complete freedom over the rotor variables. Figure 3.6 shows the variables used for parametrization.

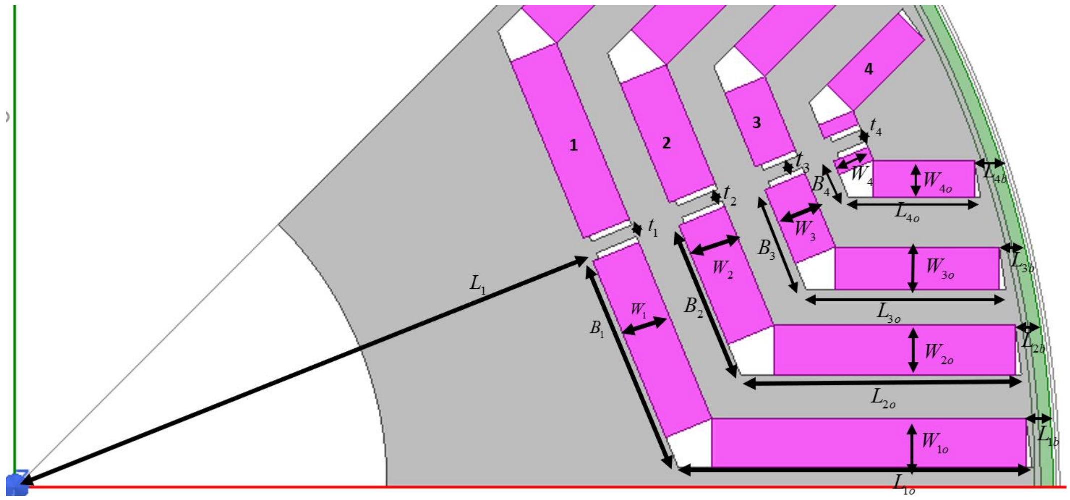

Figure 3.6: Rotor variable names for 4-layer machine

The geometry of the 4-layer machine was developed in Ansys Maxwell using trigonometric relationship and the python script was recorded simultaneously for the 1^{st} layer of the machine. The script was further updated for the other layers and once executed, it could draw the rotor geometry. In Figure 3.7, a closeup section of the 1^{st} layer is visible that will be used to explain the procedure followed for deriving the formulas.

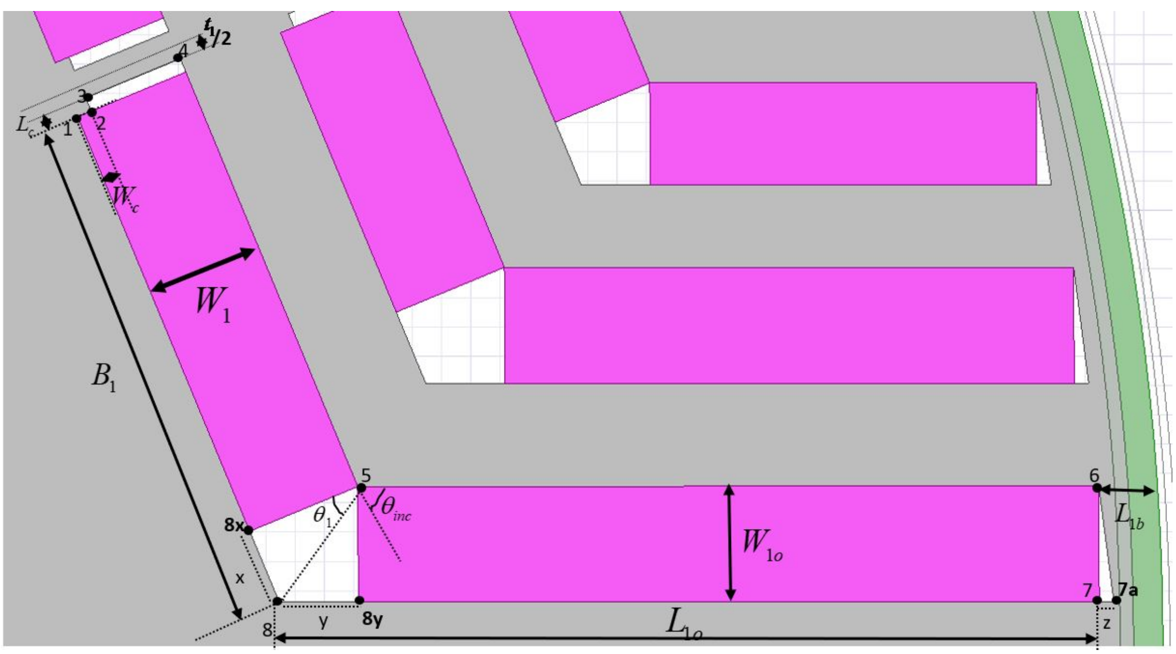

Figure 3.7: Close view of the 1^{st} layer of a 4-layer machine

In Figure 3.7, number $1, 2, 3, 4, 5, 6, 7, 8, 8x, 8y$ *and* $7a$ are the vertices of the 1^{st}

barrier whose x and y coordinates needs to be determined. All the rotor parameters except x, y, θ_1, L_{1o} are known and thus they can be changed to alter the rotor geometry. To determine x, y, and θ_1, the triangle with vertices $(8x,\ 5\ ,\ 8)$ and $(8y,\ 5\ ,\ 8)$ were observed where the angle $\angle 8x58y$ is equal to angle θ_{inc} such that

$$W_{10}\cos(\theta_{inc}-\theta_1) = W_1\cos(\theta_1) \tag{3.4}$$

The angle θ_1 can now be calculated as

$$\theta_1 = \arctan\left(\frac{1}{\sin(\theta_{inc})}\left(\frac{W_1}{W_{1o}} - \cos(\theta_{inc})\right)\right) \tag{3.5}$$

Finally the variable x and y are

$$\begin{aligned} x &= W_1\tan(\theta_1) \\ y &= W_{1o}\tan(\theta_{inc}-\theta_1) \end{aligned} \tag{3.6}$$

Once the variables x,y, θ_1 are obtained, we can derive the variable L_{1o} given that L_{1b} as shown in Figure 3.7 is 2 mm and vertex number 6 always maintains a tangential rotor bridge length of 2 mm such that

$$\left(\left(\frac{t_1}{2}+L_c+B_1-\mathrm{x}\right)+\left(\left(L_{1o}-\mathrm{y}\right)\cos(\theta_{inc})\right)\right)^2+\left(\left(L_1+W_1\right)+\left(\left(L_{1o}-\mathrm{y}\right)\sin(\theta_{inc})\right)\right)^2 = (R_r-L_{1b})^2 \tag{3.7}$$

where R_r= Rotor radius, $\left(\frac{t_1}{2}+L_c+B_1-x\right)$=A, and $\left(L_1+W_1\right)$=C. Finally, solving the quadratic equation for L_{1o} in (3.7),

$$L_{1o} = y-(A\cos(\theta_{inc})+C\sin(\theta_{inc}))+\sqrt{(A\times\cos(\theta_{inc})+C\sin(\theta_{inc}))^2-(C^2+A^2-(R_r-L_{1b})^2)} \tag{3.8}$$

In order to derive the x and y co-ordinate of vertex 1 the angle θ_1' as shown in Figure 3.8 needs to be obtained. This is the angle of inclination of coordinate 1 from the origin.$\angle$ θ_m is the angle at which the rotor geometry is being analysed i.e at $\angle 22.5°$.

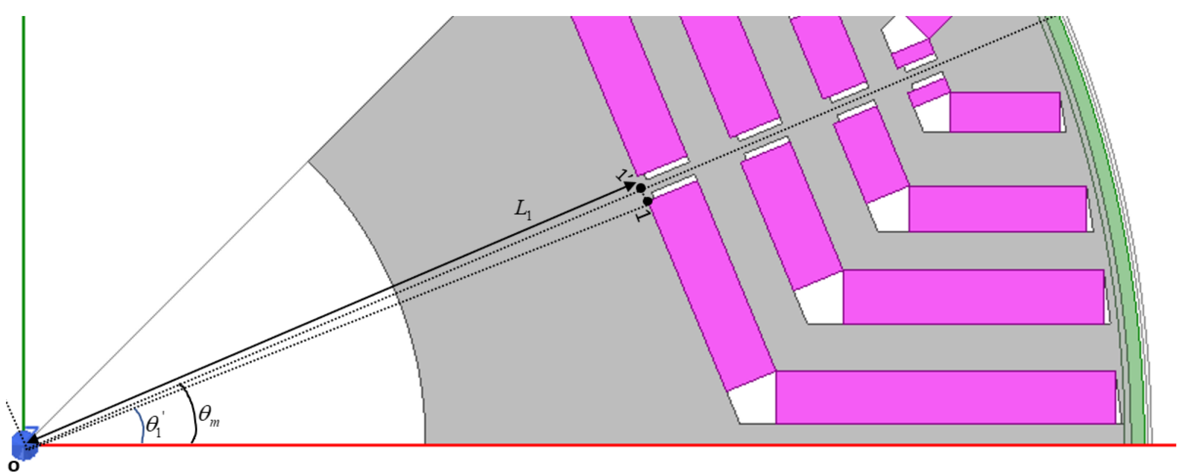

Figure 3.8: Angle of inclination of co-ordinate 1 from the origin

The triangle 1'o1 is a right angle triangle and hence

$$\begin{aligned}\angle 1'o1 &= \arctan\frac{\frac{t_1}{2}+L_c}{L_1}\\ \theta_1' &= \angle\theta_m - \angle 1'o1\end{aligned}\tag{3.9}$$

Using (3.9) and resolving the hypotenuse of the triangle 1'o 1 upon x and y axis, the co-ordinate of vertex 1 is obtained as

$$\begin{aligned}co_{x1} &= \sqrt{(\frac{t_1}{2}+L_c)^2+(L_1)^2}\cos\theta_1'\\ co_{y1} &= \sqrt{(\frac{t_1}{2}+L_c)^2+(L_1)^2}\sin\theta_1'\end{aligned}\tag{3.10}$$

For the remaining vertices a similar approach can be followed and the coordinates for all the other vertices numbers could be obtained. In Table 3.5, the initial rotor parameters for a 4-layer machine are given.

Table 3.5: Rotor dimension for the 4-layer

Layer No.	Parameter	Value	Unit
1	B_1	18	mm
	W_1	4	mm
	W_{1O}	4	mm
	L_1	55	mm
	L_{1O}	23	mm
	L_{1b}	2	mm
	t_1	1	mm
	L_c	0.5	mm
	W_c	0.5	mm
	θ_{inc}	67.5	deg
2	B_2	13	mm
	W_2	4	mm
	W_{2O}	4	mm
	L_2	62.5	mm
	L_{2O}	18	mm
	L_{2b}	2	mm
	t_2	1	mm
	L_c	0.5	mm
	W_c	0.5	mm
	θ_{inc}	67.5	deg
3	B_3	8.7	mm
	W_3	3.5	mm
	W_{3O}	3.5	mm
	L_3	70	mm
	L_{3O}	10.5	mm
	L_{3b}	2	mm
	t_3	1	mm
	L_c	0.5	mm
	W_c	0.5	mm
	θ_{inc}	67.5	deg
4	B_4	3.12	mm
	W_4	3	mm
	W_{4O}	3	mm
	L_4	76	mm
	L_{4O}	5	mm
	L_{4b}	2	mm
	t_4	1	mm
	L_c	0.5	mm
	W_c	0.5	mm
	θ_{inc}	67.5	deg

3.7 Spoke type configuration

The spoke type PMSM is an attractive topology for a high-performance vehicle traction application[12]. The proposed spoke type configuration can be an effective substitute for the reference machine which requires low torque ripple and high efficiency. In particular, the spoke type PMSM motor has low acoustic noise and vibration compared to the v-shape PMSM motor[13]. The proposed spoke type permanent magnet synchronous motor contains radially distributed ferrite magnets (see Fig.3.9). Despite the low remanence flux density of the ferrite magnet, one can actively utilize the magnet torque in such machines due to its radial arrangement of magnets. The reluctance torque is properly utilized by altering the rotor structure but this affects the magnet torque. In [14], the results indicates that the performance loss from the ferrite magnets can be compensated by utilizing the reluctance torque in a spoke type PMSM.

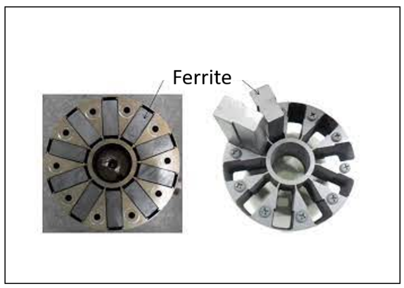

Figure 3.9: Spoke type configuration

Spoke-type PMSMs are effective for generating flux from the magnets due to the fact that they have a larger magnet size than other types of PMSMs and this results in a higher magnetic torque. While designing a spoke machine type it is important to consider [12]:

- to prevent irreversible demagnetization resulting from the low coercivity of the ferrite magnets.
- to prevent rotor stress resulting from inserting large size magnets into the rotor.

Table 3.6: Design parameters for the spoke type machine

Parameter	Value	Unit
Axial length	162	mm
Stator outer diameter	252	mm
Rotor outer diameter	169.3	mm
Thickness	12	mm
Width	65	mm
Rib	3	mm
Nonmagnetic material	2	mm

3.7.1 Design of spoke type machine:

The proposed design of the spoke type configuration consists of a three-phase stator with double layer distributed winding. It has the same size as the reference machine and it is designed in Ansys Maxwell Rmxprt. In this spoke structure, two different geometry are analysed to obtain the rated torque (see Table 3.1). The proposed spoke type configurations use the design parameters that are mentioned in Table 3.6. Furthermore, MTPA control strategy was used in order to operate the machine at the most efficient point and to minimise the losses while achieving the required torque. The design of the spoke machine also includes evaluation of irreversible demagnetisation at maximum current density and mechanical integrity at top speed.

3.7.1.1 Machine without triangular cutouts

It is a basic type of spoke PMSM having rectangular shaped magnets with small ribs to suppress the leakage flux in the rotor[12]. In the field weakening region, the outer edges of the magnets in the radial direction get easily demagnetised. In order to reduce the risk of demagnetisation, non-magnetic material such as glass is used in the rotor as shown in Figure 3.10. It provides path for the flux during the field weakening operation. The non-magnetic material of arbitrary size is included in the rotor structure in the form of a rectangle which can be altered based on the demagnetisation effects. The results will be shown in section 5.11.

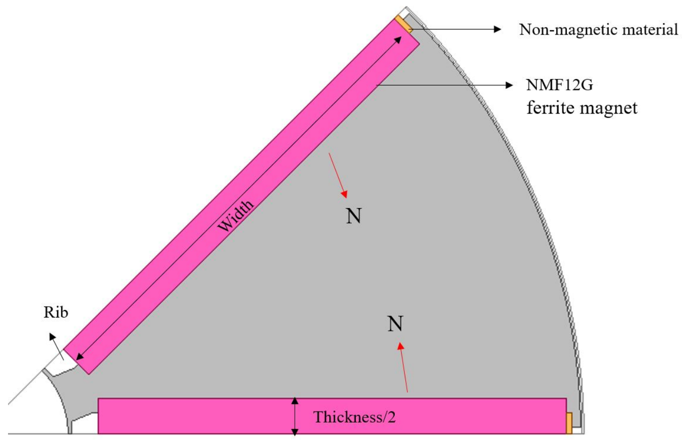

Figure 3.10: Spoke type-Machine without triangular cuts

3.7.1.2 Machine with triangular cutouts

The machine shown in Figure 3.11 has the same specifications as the machine without triangular cutouts (see Fig.3.10), but it also has triangular cutouts in the outer surface of the rotor to utilise the reluctance torque. Some arbitrary dimensions are chosen to cut the triangular shape from the rotor structure for initial analysis because the magnetic resistance along d-axis magnetic flux path was increased. It would be expected to have a higher saliency ratio when compared with the machine in section 3.7.1.1, therefore it would generate more reluctance torque.

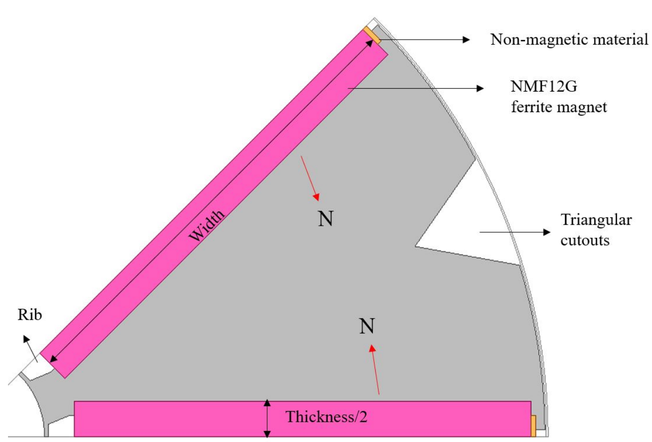

Figure 3.11: Spoke type-Machine with triangular cuts

3.7.2 Analysis of spoke type machine:

The rotor structure was altered based on the iteration process. For the purpose of comparison with the reference machine, the proposed design is analysed in terms of air gap flux density, permanent flux linkage, power factor, saliency, torque, reluctance torque, losses and efficiency. The results are explained in detailed in Chapter 5. A parametric study was carried out in which the dimensions of the triangular cut was altered to see the effects of certain parameters like saliency, power factor, reluctance torque, etc. The width and thickness of the magnet were varied to reduce the torque ripple and to meet the desired torque of the reference machine. The size of the magnet and non-magnetic material were altered in order to reduce the demagnetisation effects.

4

Results for the ARC type configuration

The arc type machine will be compared with the reference machine for a number of different performance parameters. On several occasions the machines will be analysed at a peak current of 707 A while varying the current angle from 90° to 180°.

4.1 Initial parametric sweep of the rotor geometry

The values given in Table 3.4 and 3.5 were initial parameters. To reach optimal rotor parameters, the machine was analysed at a speed of 1000 rpm and peak phase current. The following parameters were altered for the analysis:

- Average torque
- Torque ripple

Distance of the magnets (Y30BH) from the center of the shaft i.e. $L_1 - L_4$ were varied according to the Table 4.1 and the results are listed in it.

Table 4.1: Rotor parametric sweep for the 4-layer machine

Experiment No.	$L_1(mm)$	$L_2(mm)$	$L_3(mm)$	$L_4(mm)$	Average Torque (Nm)	Torque ripple(Nm)
1	50	57.5	65	71	312	22
2	51	58.5	66	72	312	27
3	52	59.5	67	73	312	33
4	53	60.5	68	74	312	41
5	54	61.5	69	75	310	46
6	55	62.5	70	76	309	51

The average torque was similar in all cases but the torque ripple was minimum for experiment no.1. Hence the distance of the magnets from the center of the shaft was chosen as in experiment no.1 in Table 4.1. Similar to the sweep in Table 4.1, a parametric sweep for W_1, W_2, W_3, W_4, W_{1O}, W_{2O}, W_{3O}, and W_{4O} was also performed but the value listed in Table 3.5 were found to be optimal for them. When the final geometry was simulated with the NMF12G magnets, a maximum torque of 350 Nm was obtained. Since the focus of this thesis is to compare different ferrite magnet-based machines with the Nd magnet based reference machine, the following parameters were chosen for the comparison

- Air gap flux density
- Permanent magnet flux linkage
- Saliency ratio
- Net torque and Reluctance torque
- Power factor

4.2 Air gap flux density

The air gap flux density is evaluated in the middle of the air gap. The stator current was set to zero while the simulation was performed with the magneto static solver. The final results were plotted for the air gap flux density with the rotor position for one pole.

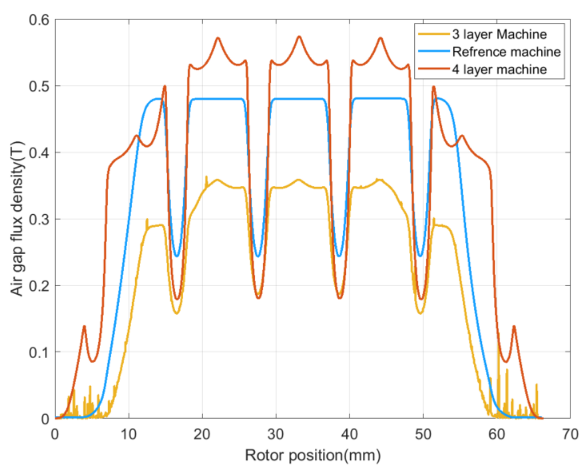

Figure 4.1: Air gap flux density comparison at no load

As can be seen from Fig.4.1 the flux density is highest for the 4-layer machine. The flux density for the reference machine is between the 4-layer and the 3-layer machine.

The difference in magnitude is due to the amount of magnets that is used in the 4-layer and 3-layer machine. The comparison of the magnet mass and magnet area for the three different machines are presented in Table 4.2.

Table 4.2: Magnets mass per pole comparison

Machine Type	No. of magnets	Area of the magnet(mm2)	Density(Kg/m3)	Mass(Kg)
Reference Machine(NdFeB)	4	295	7700	0.38
3 Layer (Ferrite)	12	435	5000	0.35
4 Layer (Ferrite)	16	747	5000	0.60

The air gap flux density due to PM is an indicator of the magnetic shear stress that is derived through Maxwell stress tensor ([4],page 388). Magnetic shear stress is the maximum average force acting per unit area of the air gap surface. The magnitude of magnetic shear stress for a 4-layer machine is 30 kN/m^2.

4.3 Permanent magnet flux linkage

The permanent magnet flux linkage varies with the q-axis current. Simulation was carried out at constant current angle of 90°while changing the peak current magnitude from 0 to 700 A in several steps. Since the d-axis current is zero, the flux linkage along the d-axis is only due to the PM. The result is shown in Figure 4.2.

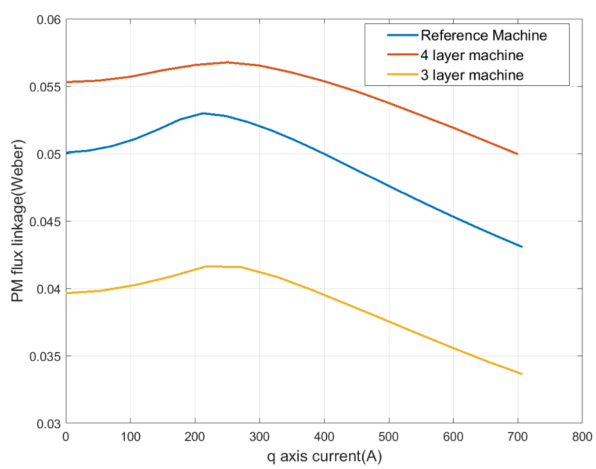

Figure 4.2: Permanent magnet flux linkage

The magnitude of the permanent magnet flux linkage is a very important parameter indicating the contribution of the PM torque. It also indicates the possibility of a better power factor for higher PM flux linkage. From Figure 4.2 it is clear that the PM flux linkage is highest for 4-layer machine due to high amount of magnets that are used as shown in Table 4.2.

4.4 Net torque and reluctance torque

To plot the net torque and the reluctance torque, the magnitude of the peak phase current was kept constant at 707 A for all the machines while the current angle was swept from 90°to 180°. Equation 4.1 was then used to evaluate the net torque and the reluctance torque.

$$\tau_{em} = \frac{3}{4} p \left(\psi_{PM} i_d + \left(L_d - L_q \right) i_d i_q \right) \tag{4.1}$$

The net torque of the 4-layer machine is very similar to the reference machine and it is possible to meet the peak torque demand of the reference machine (see Figure 4.3) with the 4-layer machine keeping the same machine volume as the reference machine. The reluctance torque of the ferrite based machine was also very similar to that of the neodymium based machine as shown in Figure 4.4.

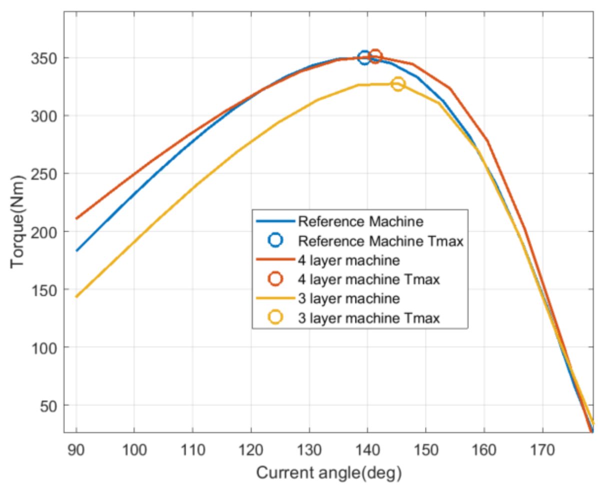

Figure 4.3: Net torque comparison

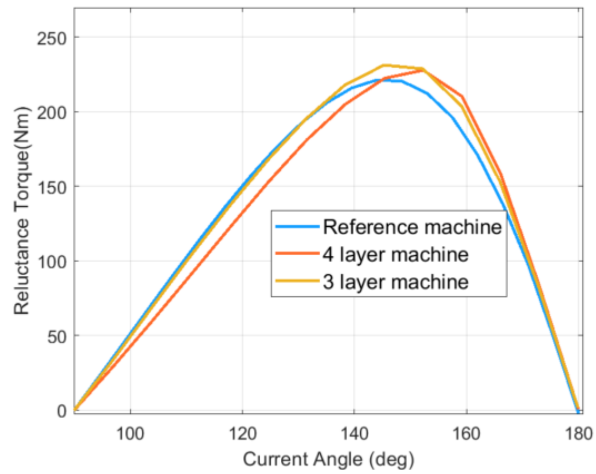

Figure 4.4: Reluctance torque comparison

The 3-layer machine was able to achieve a peak torque of 327 Nm which is 93 % of the required torque. The amount of magnets used should also be kept in mind since the 3-layer machine has almost half the magnet weight/pole as compared to a 4-layer machine (see Table 4.2).

4.5 Saliency ratio

To plot the saliency ratio, the magnitude of the peak phase current was kept constant at 707 A for all the machines while the current angle was swept from 90°to 180°. The saliency ratio increases with the current angle as presented in Figure 4.5. It is highest for the 4-layer machine in the field weakening region which starts around 140°. The sharp increase in the saliency ratio of a 4-layer machine is due to the usage of more layers and hence a higher insulation ratio ([3],page 23). The ratio of the amount of air used with respect to the amount of iron is known as insulation ratio. This parameter has a great effect on the power factor of the machine. Machines with better saliency ratio is able to generate more active power for the same amount of apparent input power. It was mentioned in [3] that with an increase in the saliency ratio, the PM flux linkage reduces and vice versa.

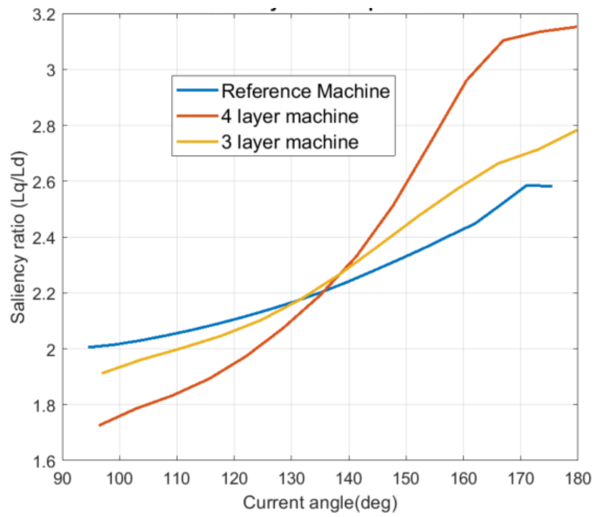

Figure 4.5: Saliency ratio

4.6 Power factor

To plot the power factor, the magnitude of the peak phase current was kept constant at 707 A for all the machines while the current angle was swept from 90°to 180°. The relevant parameters were then calculated and substituted in

$$Powerfactor = \cos\left(\arctan\left(\frac{((\psi_{PM} + L_d \times i_d) / (L_q \times i_q) + (i_q/i_d))}{(\psi_{PM} + L_d \times i_d) / (L_q \times i_d) - 1}\right)\right) \tag{4.2}$$

where L_d is the d-axis inductance, L_q is the q-axis inductance, i_d is the d-axis current, i_q is the q-axis current. As expected 4-layer machine has higher power factor than the other two machines. This can be seen in Figure 4.6

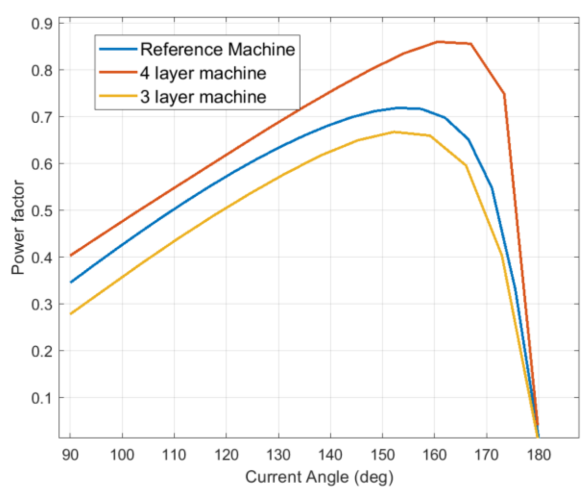

Figure 4.6: Power factor comparison

As shown in (4.2), power factor depends both on the PM flux linkage and the saliency ratio. Both the factors were high for the 4-layer machine. Despite having a higher saliency ratio for the 3-layer machine than the reference machine, the power factor is low because of its low PM flux linkage. The power factor at base speed for each machine is shown in Table 4.3.

Table 4.3: Power factor at base speed and maximum torque

Machine Type	Base Speed(rpm)	Power factor
Reference Machine(Nd)	4400	0.66
3 Layer (Ferrite)	4400	0.63
4 Layer (Ferrite)	4947	0.76

The plots in Figure 4.7-4.9 show the power factor and torque matrix contour for the full machine.

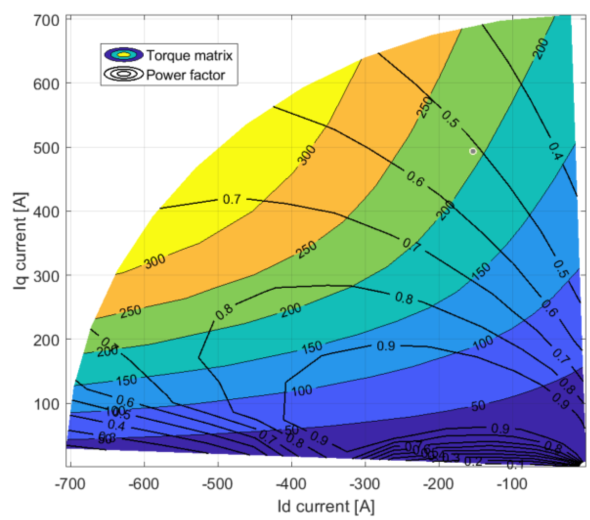

Figure 4.7: Power factor contour on top of torque contour for the reference machine

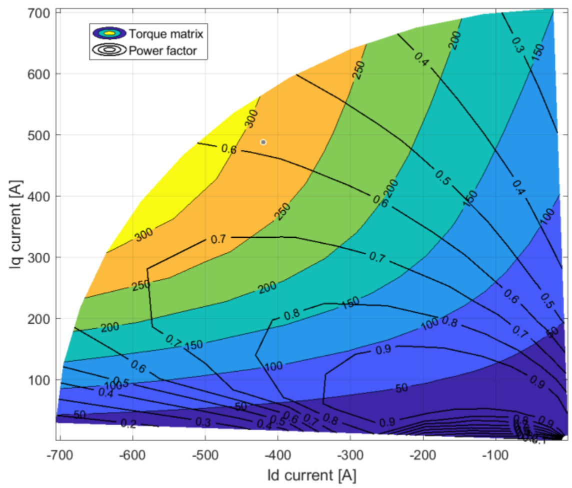

Figure 4.8: Power factor contour on top of torque contour for the 3-layer machine

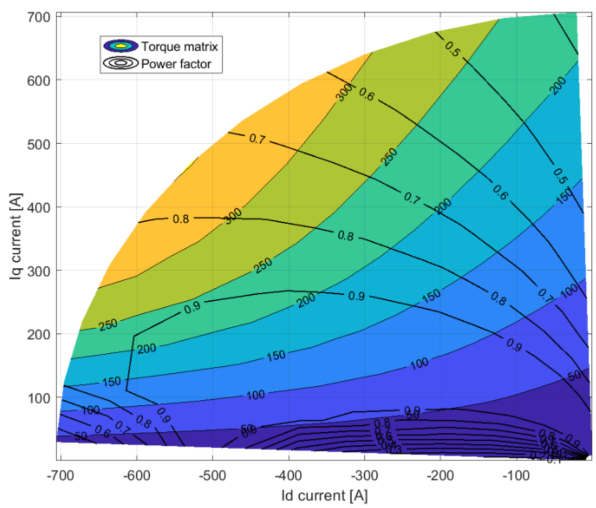

Figure 4.9: Power factor contour on top of torque contour for the 4-layer machine

4.7 Control strategy

To evaluate the control capability of different machines, the voltage and current limit was checked for each data point in the maximum torque-speed region. The maximum torque speed region is shown in Figure 4.14. MTPA strategy was applied in the region below base speed while the field weakening and MTPV strategy were applied after the base speed. The results are shown in Figures 4.10-4.12.

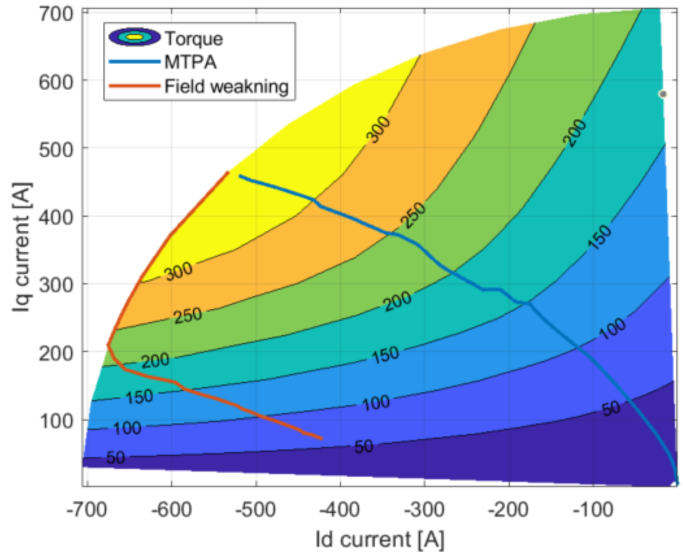

Figure 4.10: MTPA and field weakening region for the reference machine

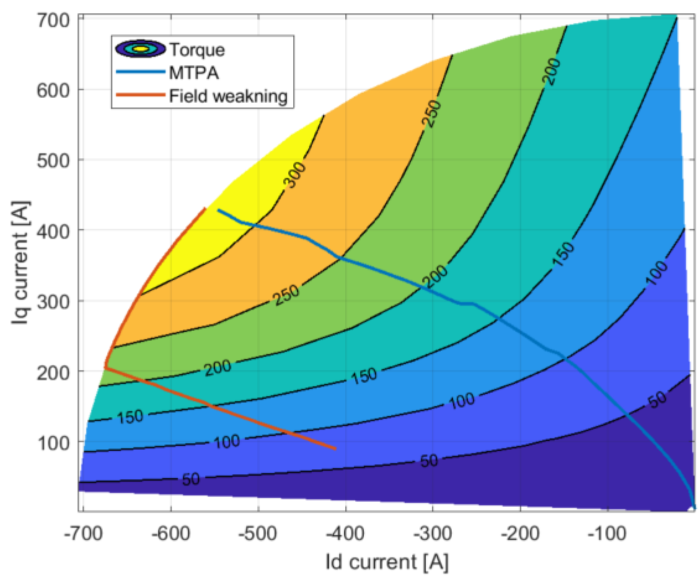

Figure 4.11: MTPA and field weakening region for the 3-layer machine

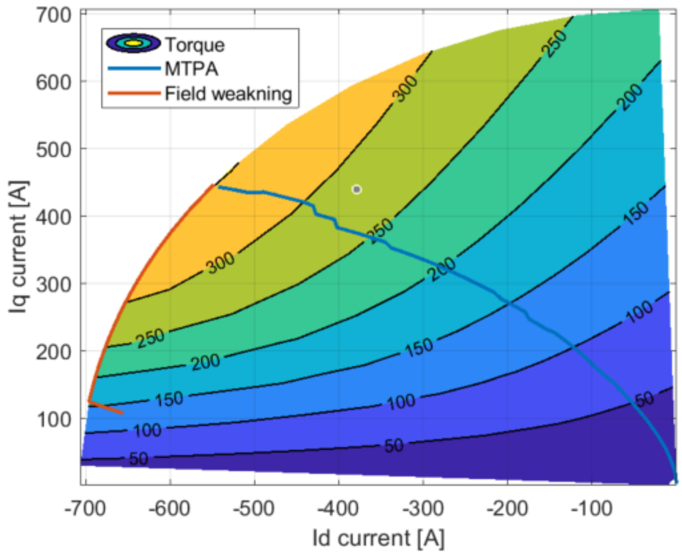

Figure 4.12: MTPA and field weakening region for the 4-layer machine

The 4-layer machine has a higher base speed than the other two machines because the voltage limit is reached for such a machine at a higher base speed. The maximum voltage ellipse intersection with the current circle determines the base speed. It is shown in Figure 4.13 that the major and minor axes of all the ellipse is almost similar (semi major axis=1050 A, semi minor axis=455 A).

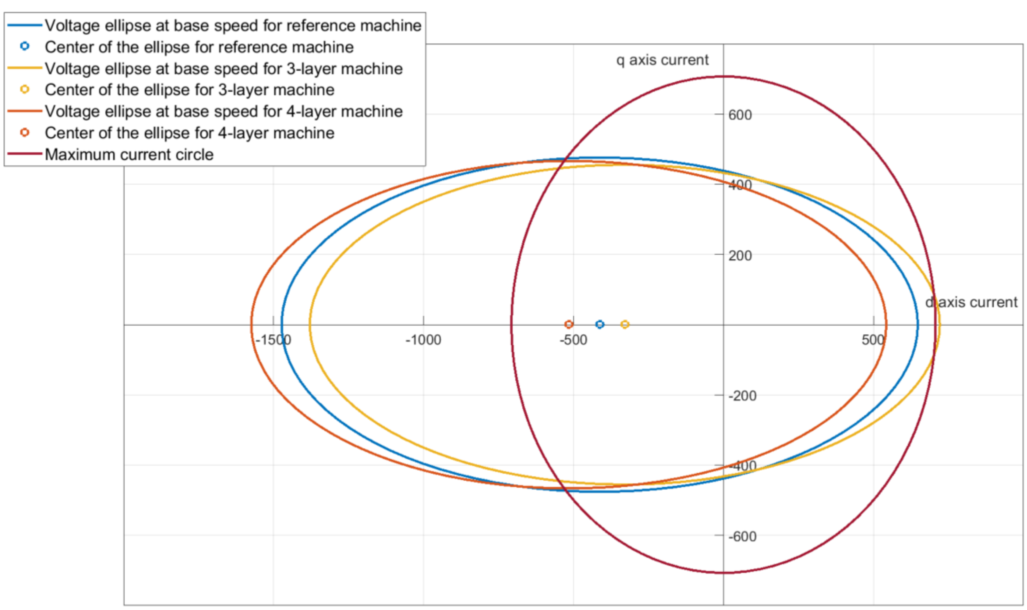

Figure 4.13: Voltage ellipse and current circle at base speed

The equation of the semi major and minor axes (4.3) indicates that for the machines with the same semi major and semi minor axes and a similar voltage limitation (u_s), the one having the lowest d and q-axes inductance would have the highest base speed. The center of the ellipse is shifted depending on the machine.

$$\begin{aligned} \frac{(i_d - i_{d0})^2}{a^2} + \frac{i_q^2}{b^2} = 1 \\ a = \frac{u_s}{\omega_r L_d} \\ b = \frac{u_s}{\omega_r L_q} \\ i_{d0} = -\frac{\psi_{PM}}{L_d} \end{aligned} \tag{4.3}$$

Since the 4-layer machine has the lowest d-axis inductance and highest PM flux linkage of the investigated machines, its center is shifted most towards the negative d-axis. The 4-layer machine also has a wider field weakening region (see Figure 4.12). The summary of the graphs are presented in Table 4.4.

Table 4.4: Speed when maximum voltage is reached (base speed or speed at end of MTPA) and when maximum current cannot be maintained (speed at the end of field weakening and start of MTPA)

Machine Type	Base Speed(rpm)	Speed when max current not reached(rpm)	Peak Torque(Nm)
Reference Machine(Nd)	4400	7438	350
3-Layer (Ferrite)	4400	6470	330
4-Layer (Ferrite)	4947	11947	350

To calculate the MTPA and field weakening region for the entire machine a total of 11×11 combination of d-axis and q-axis current were chosen. The d-axis and q-axis currents were limited to 707 A respectively. Further, the data was collected for all the combinations from ANSYS and MATLAB analysis was performed using a fmincon function that maximizes or minimizes a given function (Current or Torque) based on certain linear and non linear inequalities (Voltage, Current and Torque limitations). This analysis allows to operate the machine at optimal points in the entire torque-speed region.

4.8 Torque-speed mapping

The control strategy stated above is used for the torque-speed mapping. The d-axis and q-axis current values were taken from Figures 4.10-4.12 and the corresponding value of torque was captured for all the machines at different speed. The result of the simulation is shown in Figure 4.14.

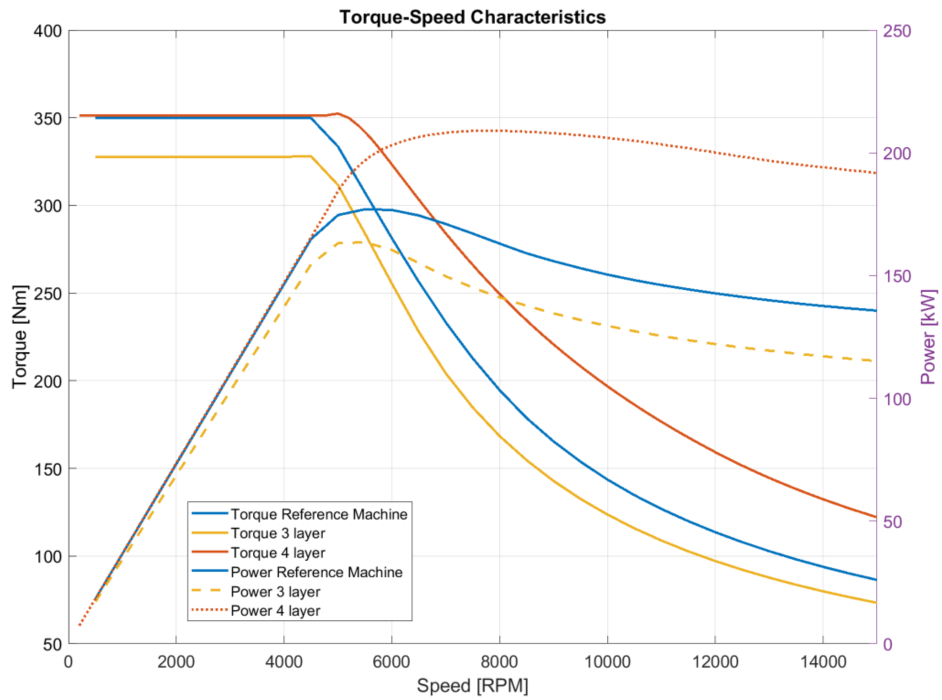

Figure 4.14: Torque-speed characteristics

Due to high power factor, the 4-layer machine is able to generate higher power in the field weakening region. Its ability to provide torque is also better in the field weakening region. This leads to a ferrite machine whose weight of the magnet/pole is high but some saving in weight of the steel lamination will occur due to use of multiple barrier. The performance of the 3-layer machine is also quite appreciable given the fact that it has lower PM flux linkage (see Fig.4.2). Instead the 3-layer machine has used more reluctance torque than the other two machines (see Fig. 4.4). A more rigorous sweep of the geometry of the 3-layer machine may enhance it's performance as will be seen in the upcoming section where the magnets of the 4^{th} layer of a 4-layer machine will be converted to steel in the simulation and its performance will be analysed (see Fig. 4.38).

4.9 Losses comparison

To evaluate the losses in the machines, they were determined in the entire torque-speed region as for an example shown in Figure 4.15.

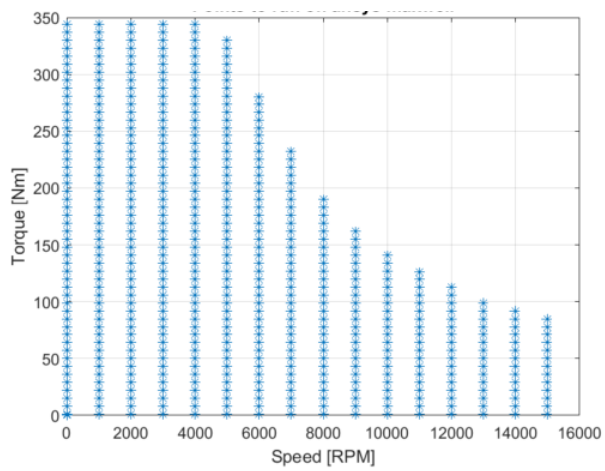

Figure 4.15: Points to run on Ansys Maxwell

Each point in Figure 4.15 is a result of the control strategy mentioned in section 4.7. Ansys simulations were conducted for all the points and the data for the losses were collected. The steel lamination that was used was Sura NO30-1600 grade non-oriented electrical steel. The eddy current and hysteresis constant that was used is shown in Appendix A, Figure A.6. This enables calculation of core losses based on different frequencies and flux density magnitudes. The loss model used by ansys is

$$p_{loss} = K_h B_{\max}^2 f + K_c \left(B_{\max} f\right)^2 + K_e \left(B_{\max} f\right)^{1.5} \tag{4.4}$$

where p_{loss} is the power loss, K_h is the hysteresis coefficient, K_c is the classical eddy coefficient, K_e is the excess or anomalous eddy current coefficient due to magnetic domains, B_{max} is the maximum amplitude of the flux density, and f is the electrical frequency.

To calculate conduction losses, the magnitude of the winding resistance/phase was calculated. This calculation was done by scaling the value of resistance from the 130 kW machine as mentioned in section 3.2. The value of the resistance is mentioned in Appendix A, Table A.1. Figure 4.16 and 4.17 shows the comparison of the 4-layer machine and 3-layer machine with the reference machine for total losses. The contour with black colour indicates that the losses for both the machines are same in those regions and hence the difference is zero.

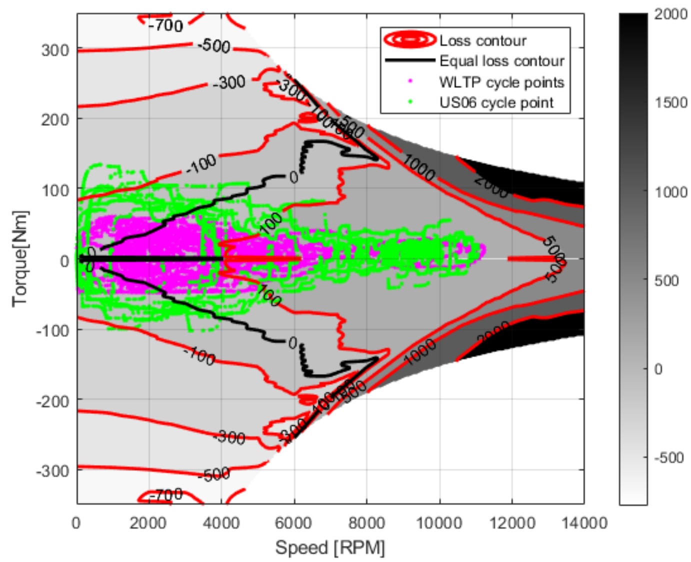

Figure 4.16: Total power loss comparison $[w]$: Reference machine minus 3 layer machine where a negative contour value indicates 3-layer machine has more losses than the reference machine while a positive contour indicates reference machine has more losses.

For Figure 4.16, on the right side of the zero contour plot i.e. the region with high speed and low torque, have contours with positive values while the region with low speed and high torque has negative contour values. Positive contour indicate regions where the ferrite based machine has less losses than the reference machine. Figure 4.16 also shows the WLTP and US06 drive cycle in the torque speed region. This indicates the working points of an EM for such cycles. Most of the working points falls in the positive contour value region for Figure 4.16 indicating that the 3-layer machine will have less energy loss than the reference machine.

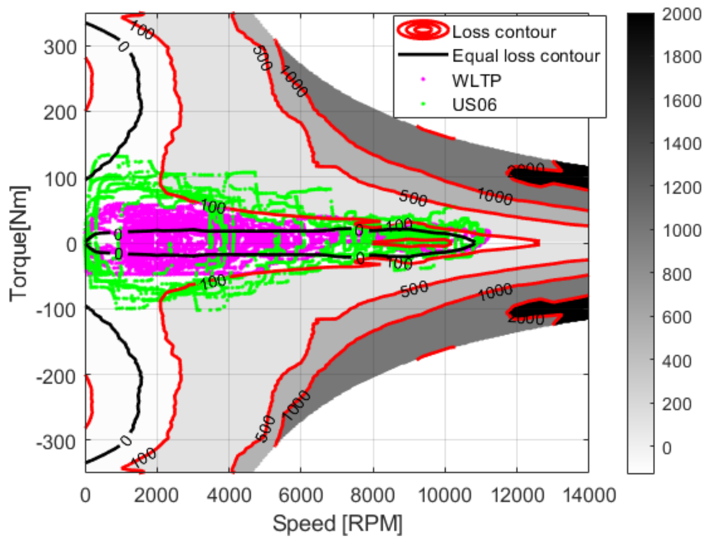

Figure 4.17: Total power loss comparison $[w]$: Reference machine minus 4 layer machine where a negative contour value indicates 4-layer machine has more losses than the reference machine while a positive contour indicates reference machine has more losses.

For Figure 4.17, most of the working points of the WLTP and US06 cycle falls in the white colour map that has negative losses indicating that the 4-layer machine will have more energy loss than the reference machine. Since the value of the contours are very small, ranging between 0-100 W for the drive cycles, the difference is insignificant.

The 4-layer and 3-layer machine was also compared with the reference machine based on different drive cycles. The torque demand by the drive cycle was fulfilled by two electrical machines where the torque was divided equally between the two machines. The drive cycle based losses for individual machines are mentioned in Figure 4.18 and corresponding drive cycles are mentioned in Figure 4.19.

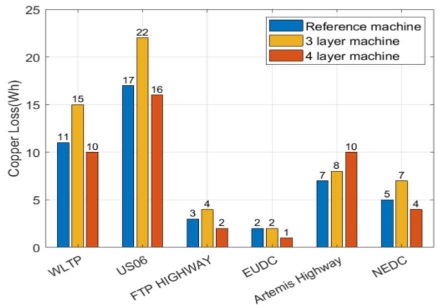

(a) conduction loss for different drive cycle

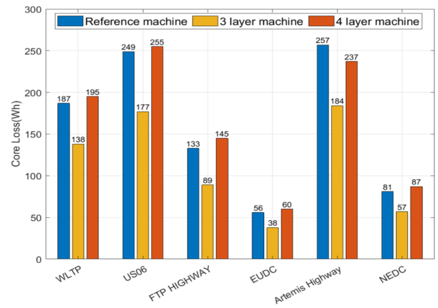

(b) Core loss for different drive cycle

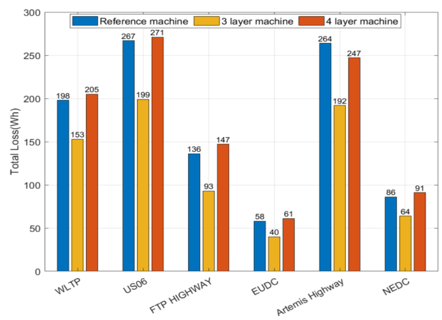

(c) Total loss for different drive cycle

Figure 4.18: Losses for individual EM for different drive cycle when using both rear and front EM equally

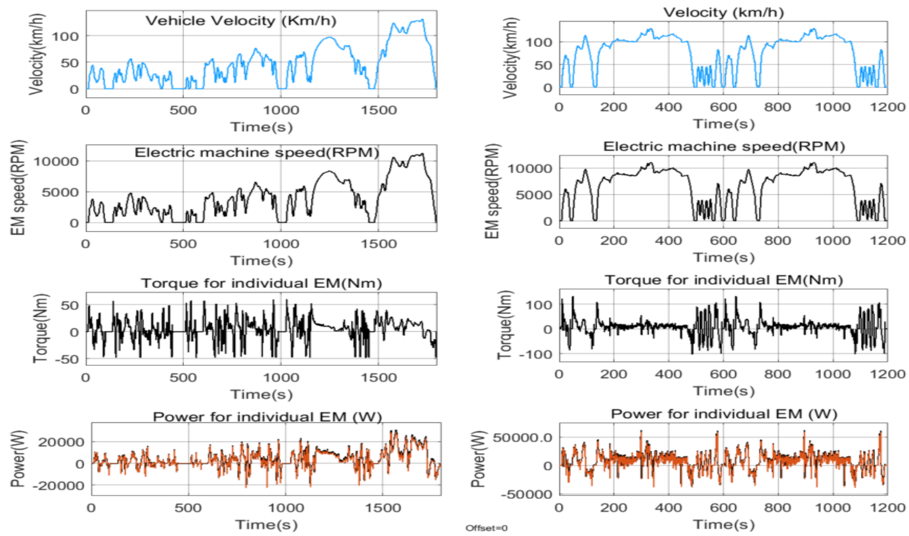

(a) EM performance for WLTP drive cycle

(b) EM performance for US06 drive cycle

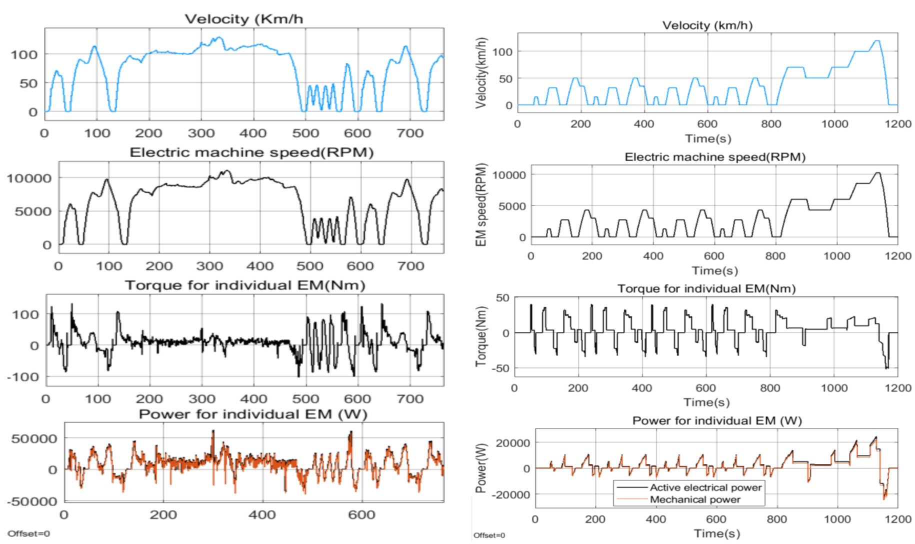

(c) EM performance for FTP highway drive cycle

(d) EM performance for NEDC drive cycle

Figure 4.19: EM performance for different drive cycle

It can be noticed from Figure 4.18 that the core losses are much higher than the conduction losses for all the machine. Figure 4.16 and 4.17 combined with Figure 4.19 indicates that the working region of the machine is limited to 100 Nm of torque for the entire speed range while the machine is capable of providing 350 Nm of torque. In this region the conduction losses are very low and core losses are relatively high. The conduction and core losses of the all the machines are shown in Figure 4.20.

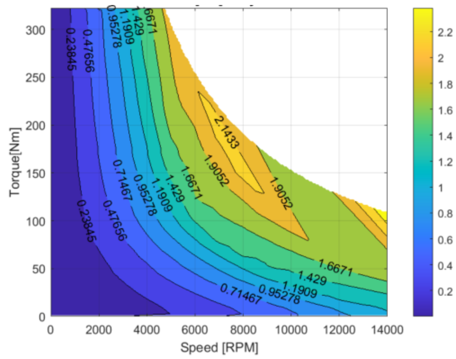

(a) Core loss for 3 layer machine

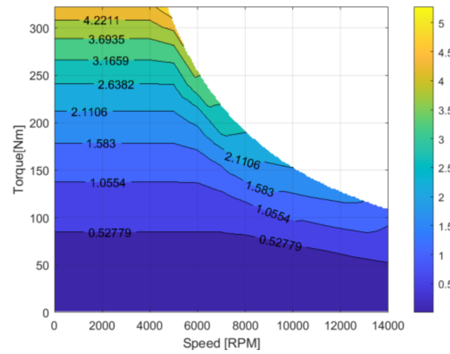

(b) conduction loss for 3 layer machine

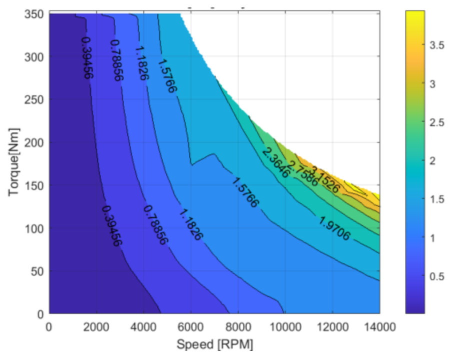

(c) Core loss for 4 layer machine

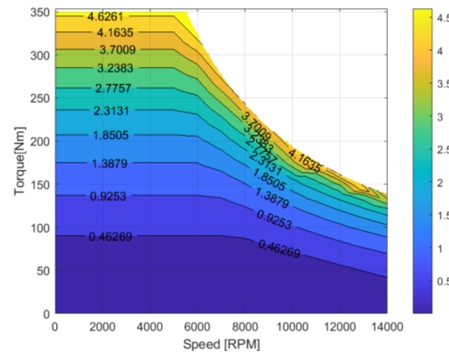

(d) conduction loss for 4 layer machine

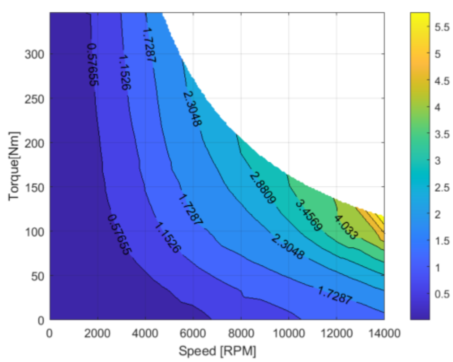

(e) Core loss for reference machine

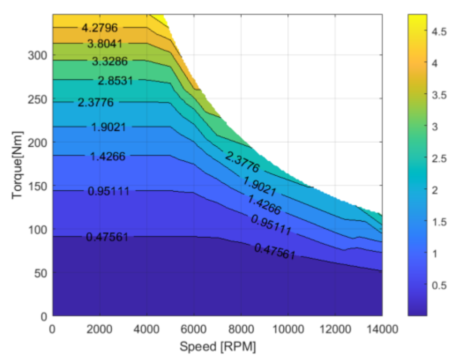

(f) conduction loss for reference machine

Figure 4.20: conduction and Core losses for different machines (kW)

It is also evident from Figure 4.18 that for a 3-layer machine which has less PM flux linkage, more current will be needed to produce the same amount of torque as the reference machine. This will increase conduction losses in the low speed and high torque region. In the low torque and high speed region the 3-layer machine machine will have less core losses since less amount of d-axis current will be needed to demagnetise the magnets as compared to the reference machine. The opposite is true for a 4-layer machine. The 4-layer and reference machines are comparable in terms of losses since they have almost the same PM flux linkage (see Fig. 4.2, PM flux linkage is only slightly higher) and PM torque. This is the reason why conduction and core losses of the 4-layer and the reference machine are distributed equally.

As already mentioned, two electrical machines of equal ratings are installed in the vehicle but for most part of the drive cycle only rear EM can be used. It is also useful to see losses for such scenario when only rear EM is used.

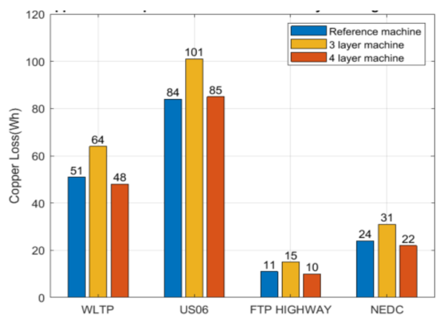

(a) conduction loss for different drive cycle

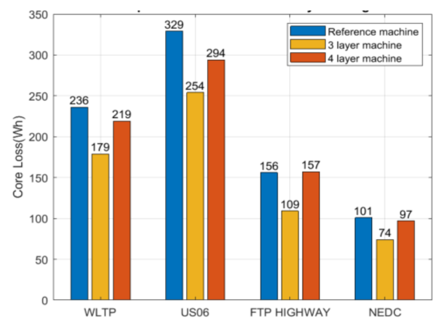

(b) Core loss for different drive cycle

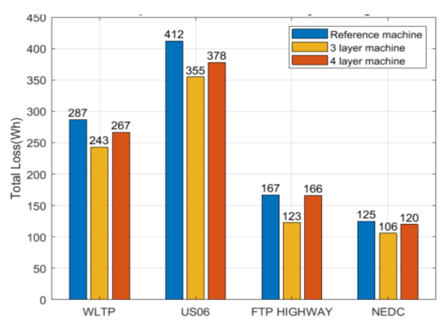

(c) Total loss for different drive cycle

Figure 4.21: EM losses for different drive cycle when only rear EM is used

When the total drive cycle losses (including both front and rear EM) in Fig.4.18 is compared with losses in Fig. 4.21, it is noticed that its beneficial to operate single EM if a single EM is enough to meet the torque requirement. The total drive cycle losses in Fig.4.18 is higher than in Fig. 4.21.

Since different drive cycles run for different distance, the drive cycle losses/km is also shown in Fig.4.22.

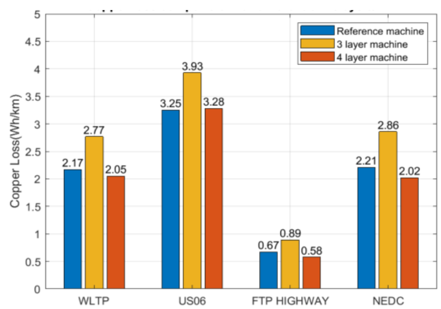

(a) conduction loss for different drive cycle

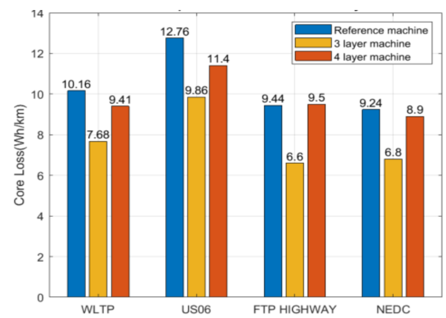

(b) Core loss for different drive cycle

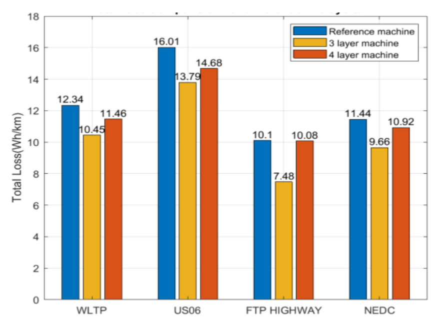

(c) Total loss for different drive cycle

Figure 4.22: EM losses/km for different drive cycle when only rear EM is used

4.10 Efficiency

The efficiency calculation was based on the ratio of the mechanical power to the electrical power for the motoring mode. It is plotted in Figure 4.23.

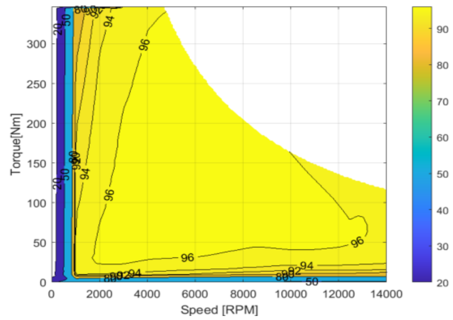

(a) Efficiency of the Reference machine

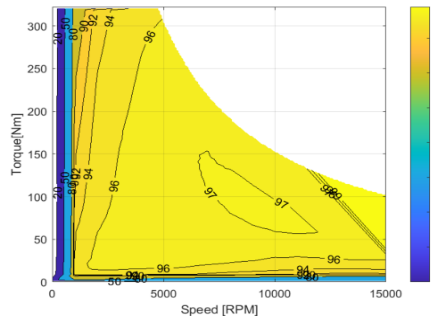

(b) Efficiency of the 3-layer machine

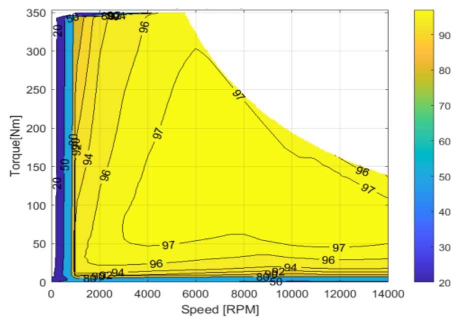

(c) Efficiency of the 4-layer machine

Figure 4.23: Efficiency of EM

For the WLTP drive cycle shown in Fig.4.24, the drive cycle efficiency was calculated to be around 95 % for the 4-layer and 3-layer machine, when only the rear wheel drive was activated. The torque and power now demanded by the vehicle from the rear axle electrical machine is shown in Fig.4.24.

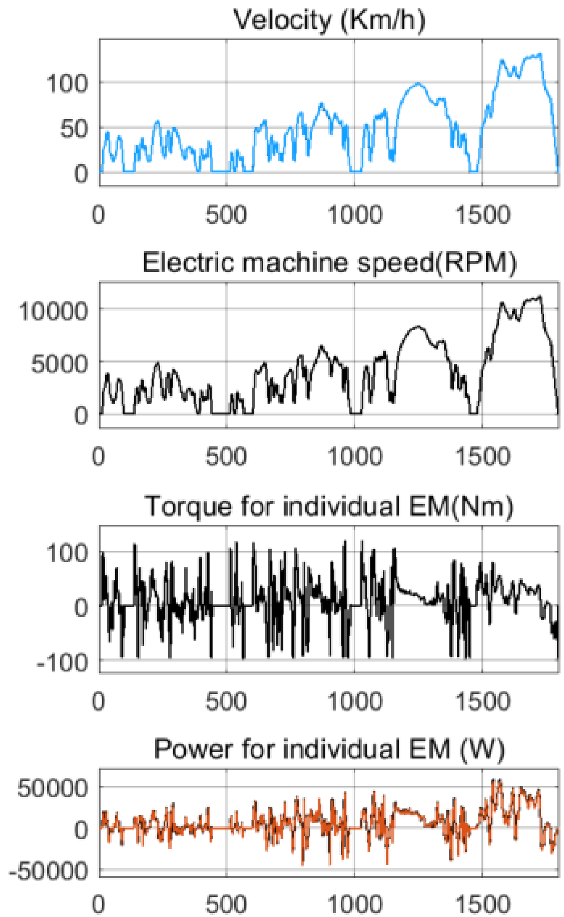

Figure 4.24: WLTP Drive cycle performance using rear axle EM only

The torque and power has clearly doubled when compared to the WLTP drive cycle shown in Fig.4.19. A similar analysis was performed for different drive cycles and the results for the drive cycle efficiency are listed in Tables 4.5 and 4.6.

Table 4.5: Efficiency in motoring mode

S.No.	cycle	3-layer machine			4-layer machine			Reference machine		
		Mech energy (Wh)	Electr-ical energy (Wh)	Effici-ency	Mech energy (Wh)	Electr-ical energy (Wh)	Effici-ency	Mech energy (Wh)	Electr-ical energy (Wh)	Effic-ency
1	NEDC	1804	1931	0.93	1804	1949	0.93	1804	1957	0.92
2	US06	6375	6694	0.95	6375	6725	0.95	6375	6758	0.94
3	WLTP	4386	4608	0.95	4386	4636	0.95	4386	4658	0.94
4	FTP Highway	2448	2572	0.95	2448	2618	0.94	2448	2623	0.93

Table 4.6: Efficiency in generating mode

S.No.	cycle	3-layer machine			4-layer machine			Reference machine		
		Mech energy (Wh)	Electr-ical energy (Wh)	Effic-iency	Mech energy (Wh)	Electr-ical energy (Wh)	Effic-iency	Mech energy (Wh)	Electr-ical energy (Wh)	Effic-iency
1	NEDC	589	554	0.94	589	555	0.94	589	552	0.94
2	US06	2026	1927	0.95	2026	1928	0.95	2026	1918	0.95
3	WLTP	1343	1278	0.95	1343	1275	0.95	1343	1269	0.95
4	FTP Highway	286	272	0.95	286	270	0.94	286	269	0.94

4.11 Vehicle performance

The EM was designed based on the requirement listed in Table 3.1. To check how the vehicle performed with the different machines, the velocity and acceleration of the vehicle was compared. A constant acceleration of 12 m/s^2 was demanded from the vehicle and the vehicle performance was observed based on the maximum torque speed graph as mentioned in Figure 4.14. It is to be noted that two electrical machine of equal rating were used at front and rear axle respectively. The performance results are shown in Figure 4.25.

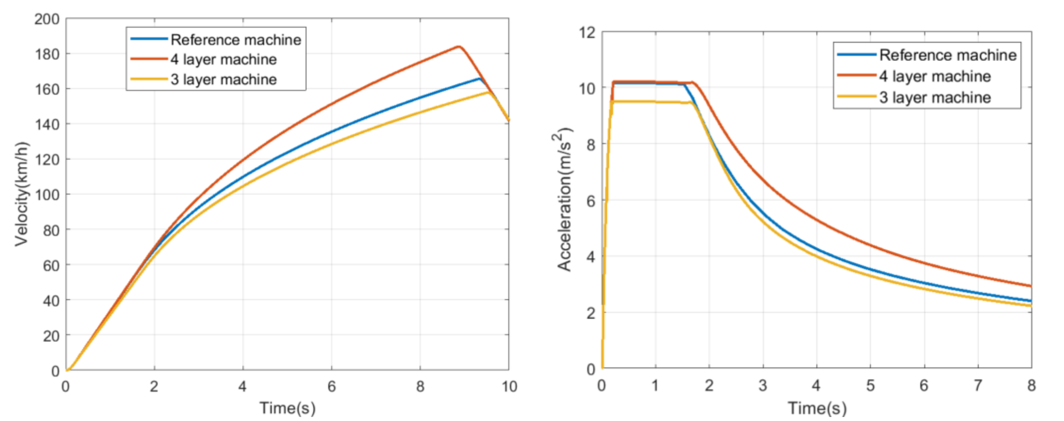

(a) Velocity profile of the vehicle for different machines

(b) Acceleration profile of the vehicle for different machines

Figure 4.25: Performance of the vehicle

4.12 Short-circuit current and demagnetisation

The machine must be protected against the short-circuit current because it has the possibility to demagnetise the magnets. The following could be the reason of such a short-circuit:

- Short-circuit between windings.
- Fault in the DC bus system.
- Fault in the Resolver.
- Fault in the power supply system.

During the short circuit the d-axis and q-axis voltage becomes zero and a large amount of transient current flows through the stator circuit. This current is mainly directed towards the d-axis of the magnets in the direction opposite to the magnets magnetisation direction. This could lead to irreversible demagnetisation of the magnets which will later have an effect on the performance of the machine. To calculate the transient short circuit current the following electrical equations were solved in MATLAB using an ordinary differential solver

$$\begin{aligned} R_s i_d + \frac{d\psi_d}{dt} - w\psi_q = 0 \\ R_s i_q + \frac{d\psi_q}{dt} - w\psi_d = 0 \end{aligned} \tag{4.5}$$

where R_s is the stator resistance, ψ_d is the d-axis flux linkage, ψ_q is the q axis flux linkage, and w is the electrical speed.

It was found that for a 4-layer and 3-layer machine the maximum short-circuit current was generated at the end of the MTPA and start of the field weakening region. It is highlighted as a black dot in Figure 4.26. For the point shown in Figure 4.26, the transient dq current is shown in Figure 4.27. The peak negative d-axis current for the 3-layer and the 4-layer machine is 1200 A and 1500 A respectively. The current angle at the this point is 180°for both the machines.

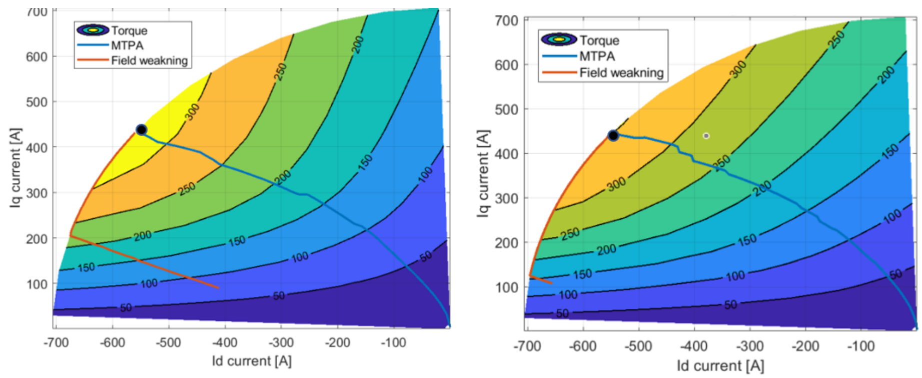

(a) 3 layer machine

(b) 4 layer machine

Figure 4.26: Maximum short-circuit current point in the dq contour

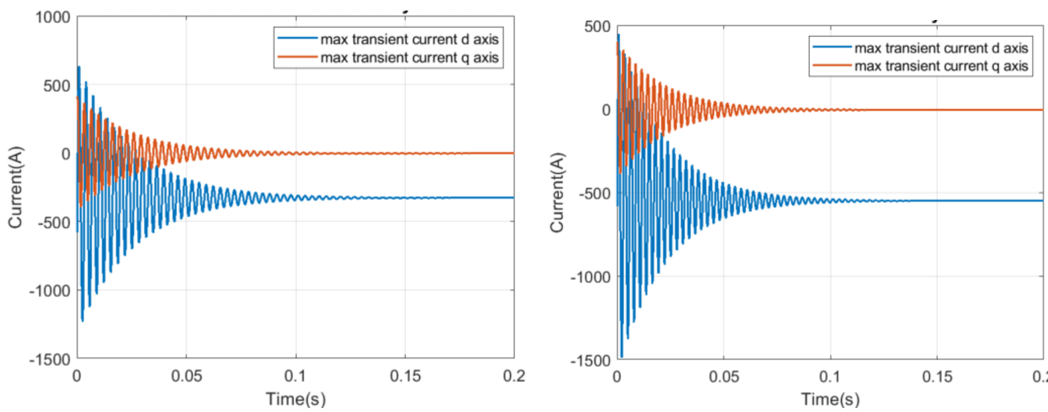

(a) 3-layer machine

(b) 4-layer machine

Figure 4.27: Transient short-circuit current

To analyse the demagnetisation behaviour of the magnet this current can be given as an input to Ansys Maxwell using the design dataset tool. The drawback of using this method is the fact that the d and q-axis inductance remains unchanged during the transient calculation in MATLAB. Alternatively, voltage excitation can also be used in Ansys to calculate transient current. The machine phases could be excited with zero voltage and the initial value of the current (just before short-circuit) is used as an initial condition. A comparison of the transient current obtained from MATLAB and Ansys is made in Figure 4.28.

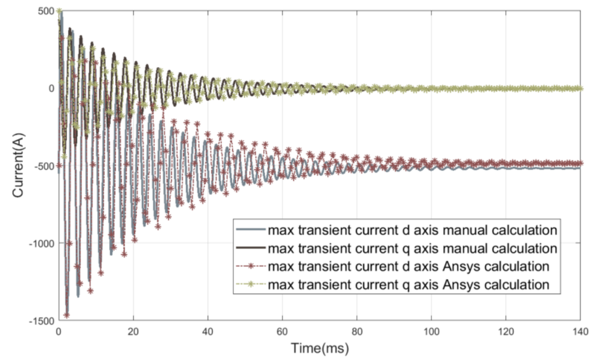

Figure 4.28: Transient short circuit current comparison between Ansys and MATLAB for the 4-layer machine

It is observed that the results from MATLAB analysis relates very well with the Ansys calculation. As evident from Figure 4.27 the peak of the negative d-axis transient current occur at 2.80 ms and 2.10 ms for 3-layer and 4-layer machine respectively. The initial angle by which this machines will be rotated is 70°and 58°respectively at its base speed. Since the ferrite magnets has a low coercivity at low temperature, it was first studied at -40 °C using NMF12G magnets. The knee point of the magnet is 0.020 T at this temperature. The range of the magnetic flux density is shown between 0-0.100 T in Figure 4.29 to observe the effect of the demagnetisation. The blue colour indicates the irreversible demagnetisation of the magnets. As observed from Figure 4.29, the 4-layer machine is demagnetised in its second and third layer while the 3-layer machine is demagnetised in the second layer.

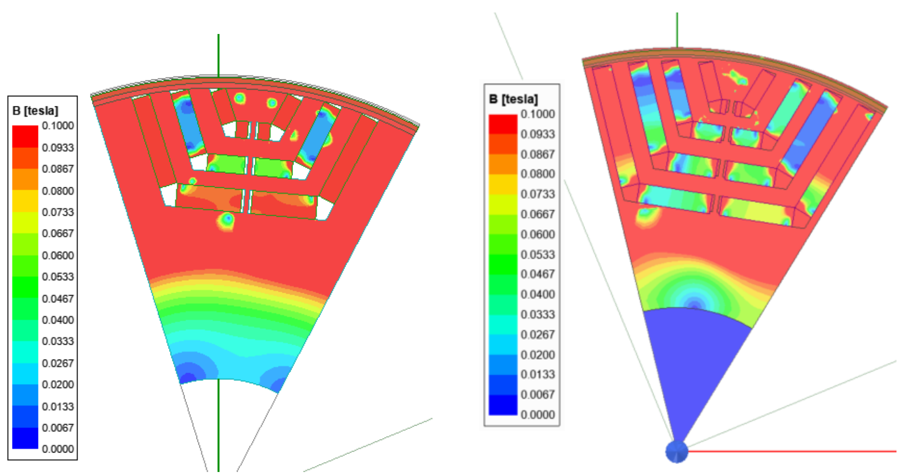

(a) 3-layer machine

(b) 4-layer machine

Figure 4.29: Demagnetisation of the machines at its highest possible d-axis current magnitude for -40 °C magnet temperature

From Fig. 4.27 the current angle at the point of maximum short-circuit (2.80 ms

and 2.10 ms for 3-layer and 4-layer machine respectively) was calculated to be 180°for both the machine. The short-circuit shown in Figure 4.27 took place when the rotor was at its starting position of -3.75°. If the rotor was at some other position when the short-circuit occurs, the peak of the transient current will be experienced by the rotor at some other rotor position rather than at 70°and 58°respectively. To analyze the demagnetisation of the magnet based on the d-axis current magnitude as well as on the position of the rotor, a constant negative d-axis current was given to Ansys model and the demagnetisation was observed for all the position of the rotor. The demagnetisation behaviour for different d-axis current magnitude is shown in Figure 4.30 and 4.31.

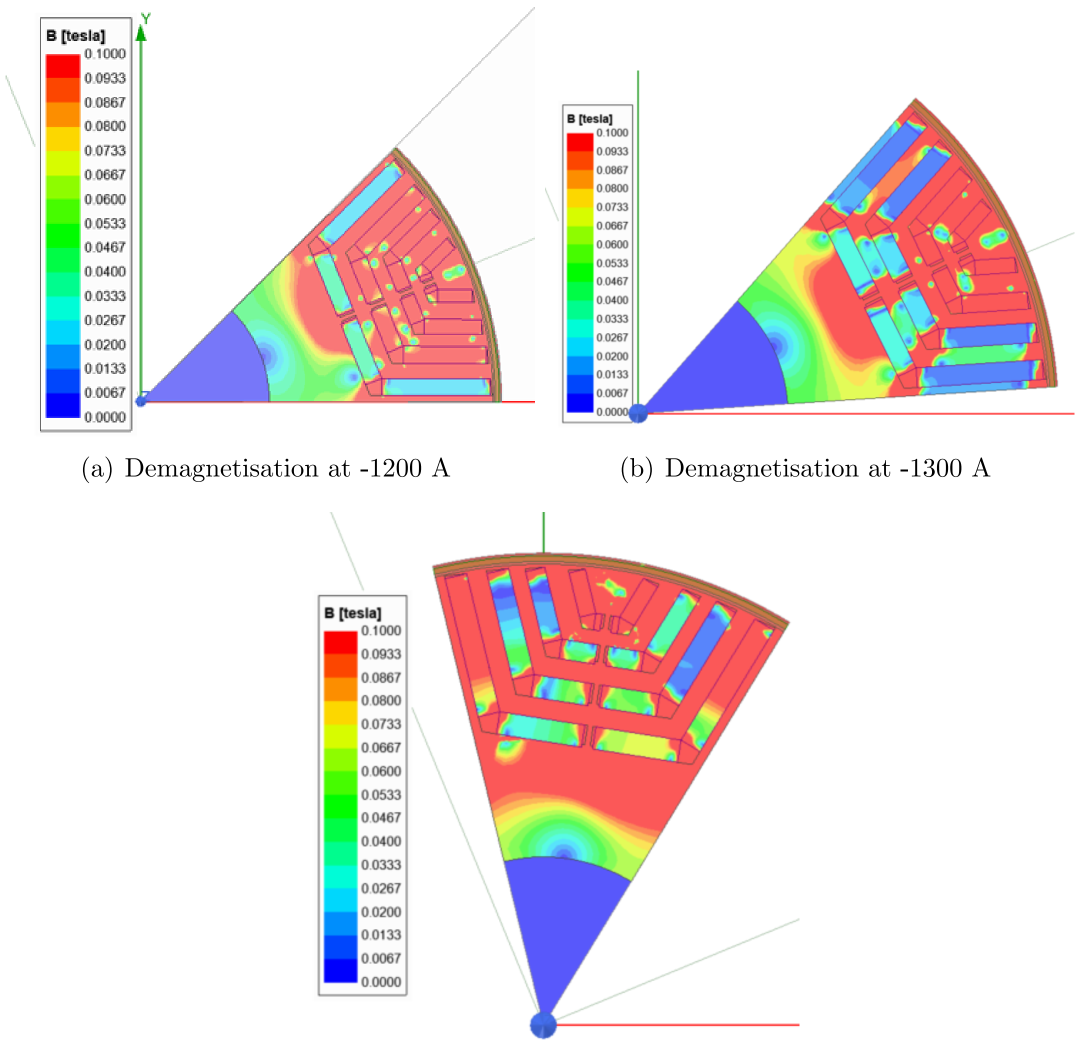

(a) Demagnetisation at -1200 A

(b) Demagnetisation at -1300 A

(c) Demagnetisation at -1500 A

Figure 4.30: Demagnetisation of 4-layer machine at different d-axis current magnitude at -40 °C of magnet temperature

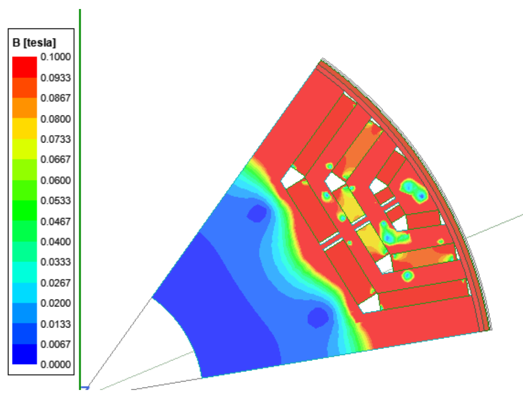

(a) Demagnetisation at -900 A

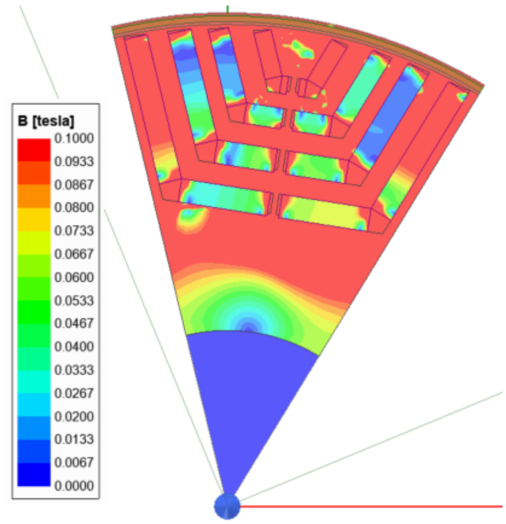

(b) Demagnetisation at -1000 A

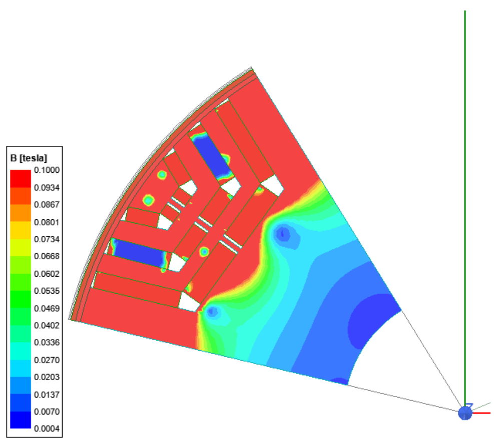

(c) Demagnetisation at -1100 A

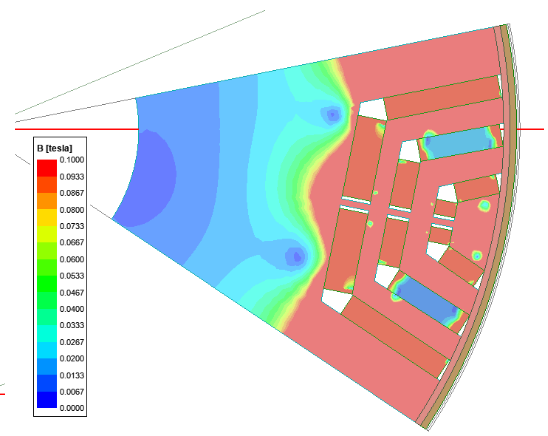

(d) Demagnetisation at -1230 A

Figure 4.31: Demagnetisation of 3-layer machine at different d-axis current magnitude at -40 °C

It was found that no demagnetisation was observed at current below 1200 A for the 4-layer machine and below 900 A for the 3-layer machine. All the points in the torque -speed region that produce a peak d-axis current of 1200 A or more was labelled as an unsafe zone for short-circuit in the 4-layer machine while the rest of the points fall under safe zone. Same is true for the 3-layer machine where the upper limit was 900 A. An unsafe zone is the point where the machine should not be short-circuited. Figure 4.32 and 4.33 show the safe and unsafe point of operation.

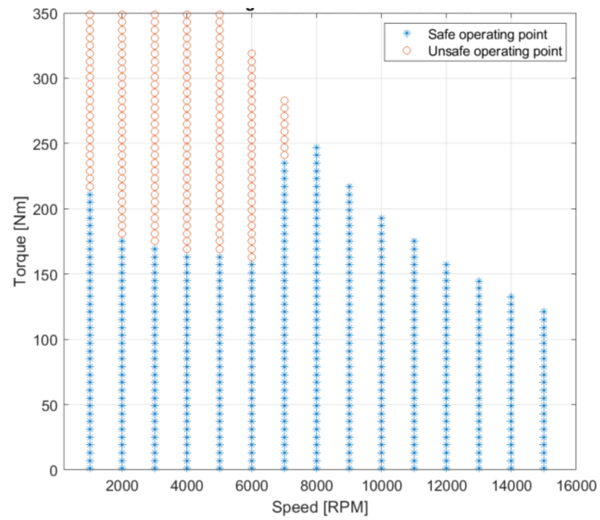

Figure 4.32: Safe and unsafe operating point in the torque-speed region for demagnetisation of the magnets of the 4-layer machine at -40°C

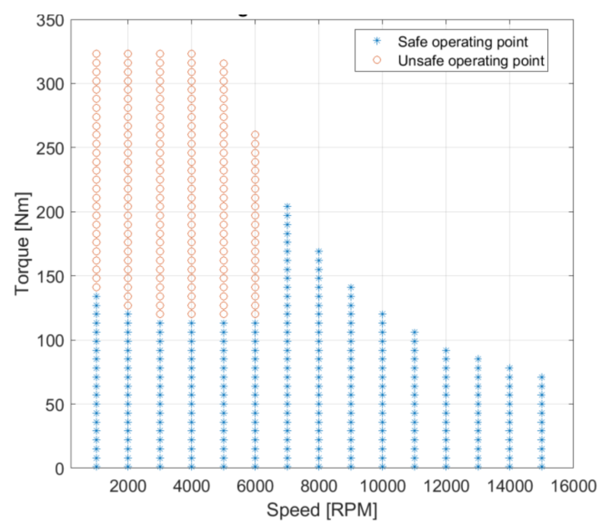

Figure 4.33: Safe and unsafe operating point in the torque-speed region for demagnetisation of the magnets of the 3-layer machine at -40°C

Since we know from Figure 3.4 that with the increase in magnet temperature the ferrite based machine will experience less demagnetisation, all the machines were analysed at different magnet temperature for the BH curve in Figure 3.4. The flux density in the rotor is shown in Figure A.5 at different temperatures where the blue colour indicates irreversible demagnetisation. No irreversible demagnetisation was observed at temperatures above 20 °C for any of the machines.

4.13 Final parametric analysis

As shown in Table 4.1, the distance of the magnets from the center of the shaft was lowered by $5mm$ from their initial position in order to reduce the torque ripple. Further analysis was performed and the 4^{th} layer of the 4-layer machine was moved from its initial position of 71 mm to 78 mm as shown in Fig. 4.38.

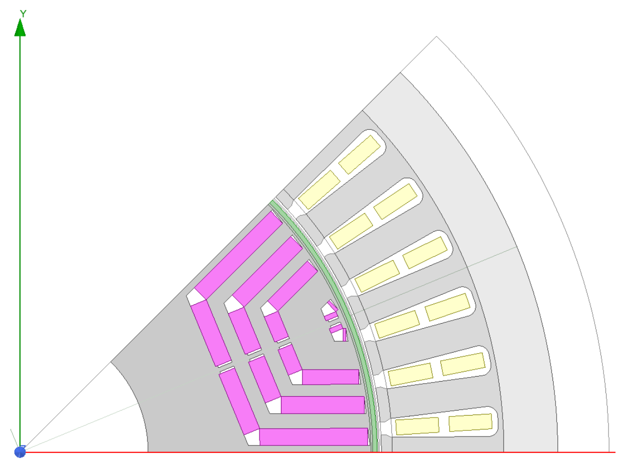

Figure 4.34: 4-layer machine with L4=$78mm$

The result of this sweep was analyzed through the PM flux linkage and the net torque. The results are shown in Fig. 4.35 and 4.36.

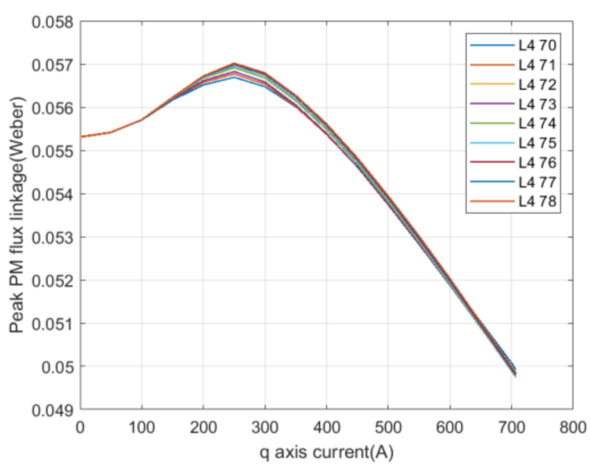

Figure 4.35: PM flux linkage for 4^{th} layer sweep of the 4-layer machine

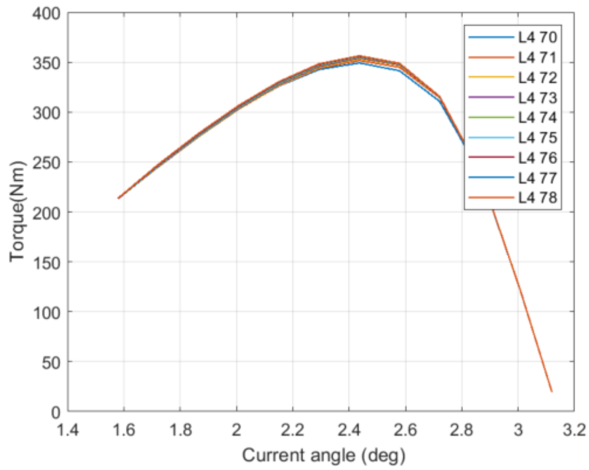

Figure 4.36: Net torque for 4^{th} layer sweep of the 4-layer machine

It is evident from the results that both the PM flux linkage and net torque is increased when L4 is 78 mm. It is also noticed that the magnet in the 4^{th} layer has now become irrelevant and hence the magnets from the 4^{th} layer were removed completely.

Another parametric analysis was performed in which the 4^{th} layer was removed completely (see Figure 4.37) and the machine was analysed with the same configuration as mentioned in Table 4.1, experiment no.1. The torque of the machine remained the same (see Figure 4.38) indicating that the 4^{th} layer is not of much importance in the machine when it comes to the peak torque but it is still needed to have better saliency ratio, power factor, and torque-speed characteristics.

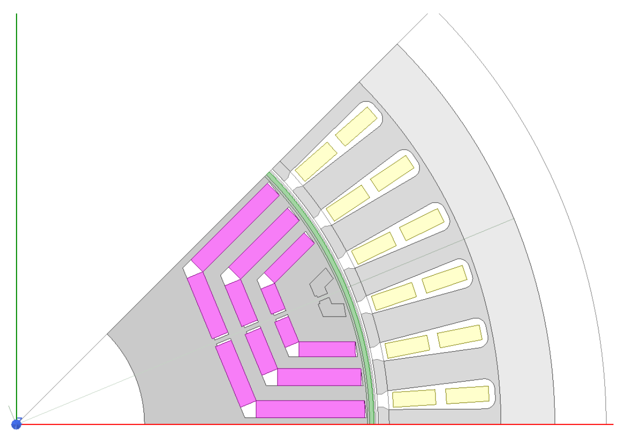

Figure 4.37: 4-layer machine modified to 3-layer

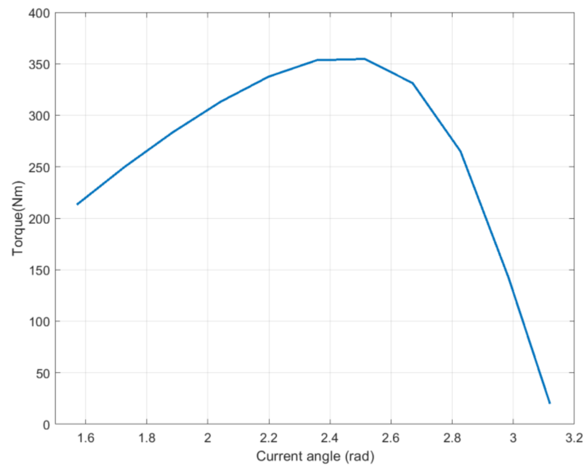

Figure 4.38: Net torque of the 4-layer machine modified to the 3-layer

4.14 Mechanical Integrity

The ferrite machines designed in this thesis are high speed machines having maximum speed close to 15000 rpm. The 4-layer machine was reviewed by experts from Volvo Cars and some changes in the future designs were suggested. Fig 4.39 shows the places where modification is needed. The red circles highlight the places where a change in the design is required.

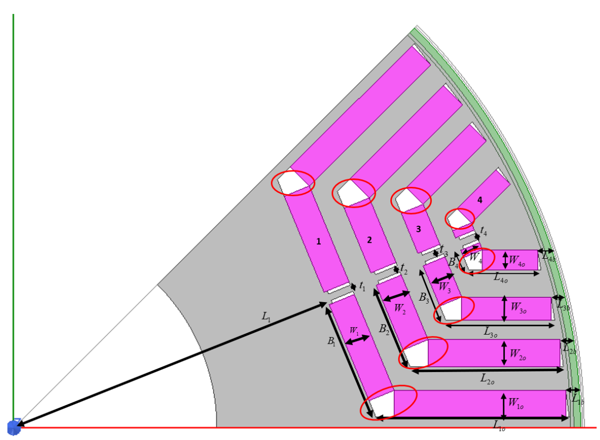

Figure 4.39: Places in the 4-layer machine that are most susceptible to structural failure

At least 1 mm of the steel bridge thickness is needed between the two magnets. This will affect the overall performance of the machine because of the leakage flux through the bridge.

5

Results for the spoke type configuration

The proposed motor was analysed by using Ansys Maxwell 2D. MATLAB was used for the control strategy and parametric analysis. The magnet temperature and the winding temperature was set to -40°C and 20°C respectively. The DC voltage and current was assigned to the spoke machine as mentioned in section 3.2 and the motor design parameters are specified in the Table 3.6. The motor was designed to have a peak power of 160 kW at a base rotation of 4400 rpm.

5.1 Air gap flux density

The air gap flux density has a high influence on the torque and induced EMF. In the spoke machine, flux per pole is supplied by two adjacent ferrite magnets. Therefore, the air gap flux density will increase due to the flux concentration structure. The air gap flux density is high because of the thickness of the magnets and the rotor would experience bigger magnetic force from the magnets [15]. The air gap length also affects the shape of air gap flux density (see Fig. 5.1), that plays a major role in noise generation and torque ripple production. The electromagnetic sizing of the machine depends on the magnitude of the flux density.

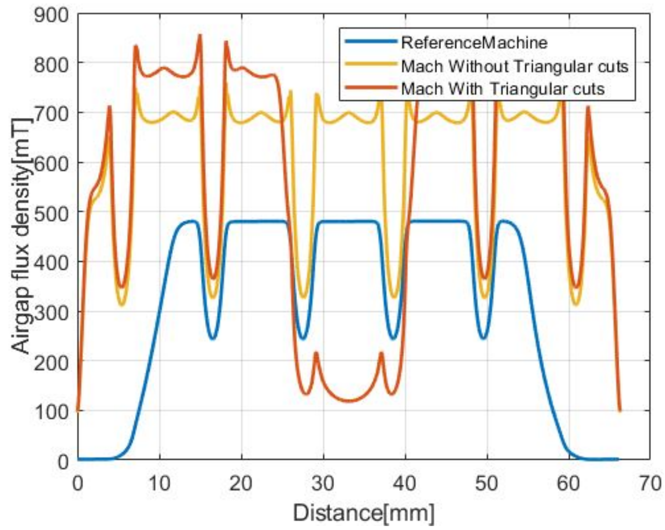

Figure 5.1: Air gap flux density comparison

The air gap flux density was analysed with the magnetostatic solver in Ansys at no load condition in the middle of the air gap. Figure 5.1 presents the resulting air gap flux density for one pole. The higher magnitude of air gap flux density in Figure 5.1 is because of the large amount of magnets and its thickness in the spoke machine. Table 5.1 shows the comparison of the magnets mass and the number of magnets per pole. The machine with triangular cuts has a higher air gap flux density compared to the reference machine because of the large magnet area. It has a sudden drop in the center of the pole due to the triangular cuts which provides the magnetic resistance along d axis as mentioned in section 3.7.1.1.

Table 5.1: Magnet mass per pole

Machine Type	No. of magnets	Area(mm^2)	Density(Kg/m^3)	Mass(Kg)
Reference Machine(NdFeB)	4	295	7700	0.38
Machine without triangular cutouts	1	650	5000	0.53
Machine with triangular cutouts	1	650	5000	0.53

5.2 Permanent magnet flux linkage

To investigate the effects of permanent magnets flux linkage, the d axis current is kept to zero. It is analysed at a constant current angle of 90° while changing the current magnitude from $0A$ to $707A$ in 11 steps.

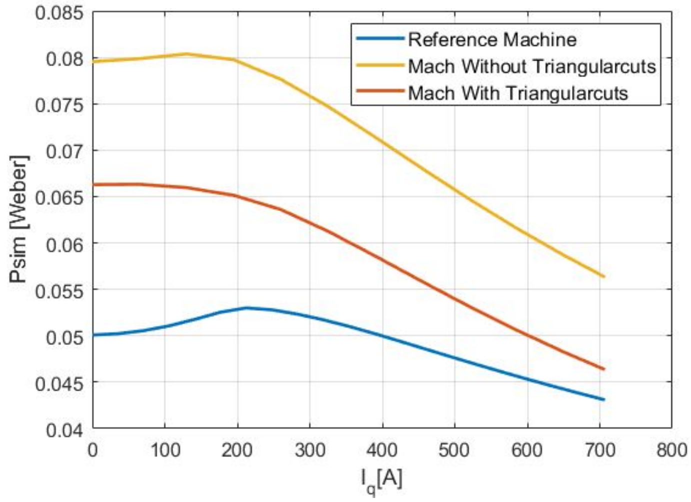

Figure 5.2: Permanent magnet flux linkage comparison

In Figure 5.2, the machine without triangular cuts has the higher ψ_{PM} and it is expected to produce more magnet torque as compared with the reference machine because of its large magnet area. The machine with triangular cutouts has the same magnet area but it has a lower ψ_{PM}, when compared with the machine without triangular cutouts. The triangular cut will affect ψ_{PM} negatively but it is beneficial for the reluctance torque production.

5.3 Torque and reluctance torque

The generated torque varies according to the motor parameters such as magnet thickness (quantity of magnet), permanent magnet flux linkage ψ_{PM} and saliency ratio. The method used for evaluating torque and reluctance torque was to keep a constant current of $707A$ and operate the machine by sweeping the current angle from 90° to 180° in Ansys. The i_d, i_q, ψ_d and ψ_q values were obtained from Ansys and substituted in (5.1). The calculated total torque and reluctance torque are presented in Figure 5.3.

$$\tau_{em} = \frac{3}{4} p \left(\psi_{PM} i_d + \left(L_d - L_q \right) i_d i_q \right) \tag{5.1}$$

where L_d is d-axis inductance, L_q is q-axis inductance, i_d is d-axis current, and i_q is q-axis current.

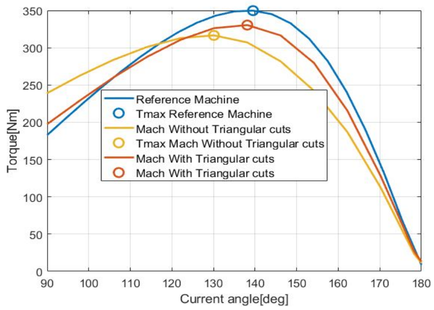

(a) Net torque comparison

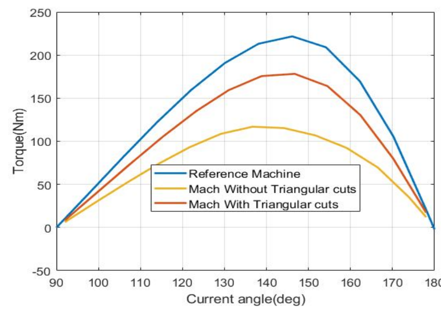

(b) Reluctance torque comparison

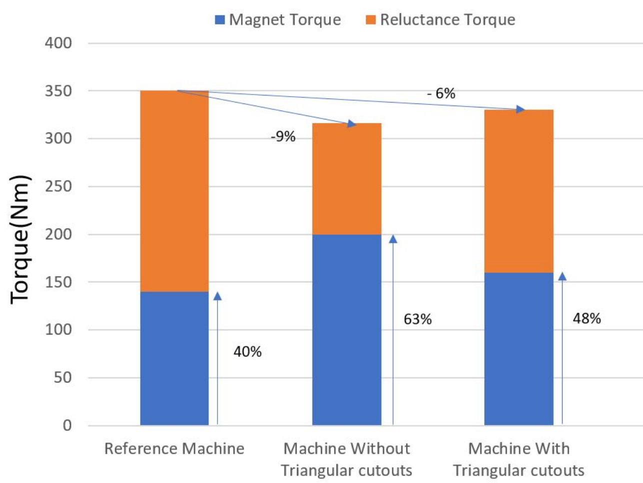

(c) Total torque comparison for all three machine

Figure 5.3: Torque comparison

The ratio of magnet torque to total torque for the machine without triangular cutouts is 63% (see Fig 5.3). As previously said, the spoke machine is capable of producing more magnet torque due to larger magnet; however, in order to actively utilize the reluctance torque, the machine with triangular cuts are designed. In Figure 5.3, it is clear that the machine with triangular cutouts has more reluctance torque and also, the overall torque increased. However, if the proposed spoke machine with ferrite magnets has the same volume as the reference machine with NdFeB magnet, there is a $6 - 9\%$ total torque reduction.

5.4 Saliency ratio

The saliency ratio of all the machines were plotted at a constant current of 707 A while the current angle was swept from $90°$ to $180°$. Figure 5.4 shows that the saliency ratio varies with the current angle.

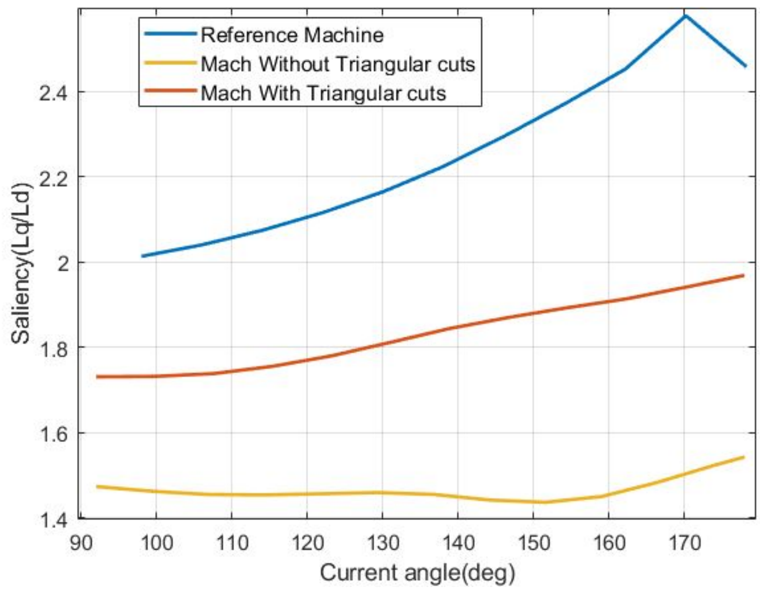

Figure 5.4: Saliency ratio comparison

The reference machine has a higher saliency ratio when compared with the other machines because it generates more reluctance torque and also, it has a more number of barriers and higher insulation ratio. The machine with triangular cutouts has a higher saliency ratio, when compared without triangular cutouts because the triangular cuts provides increased reluctance along the d axis flux path, therefore L_d decreases and, reluctance torque and saliency ratio increases. The saliency ratio was lower for the ferrite based spoke machine when compared with the reference machine due to higher ψ_{PM}.

5.5 Power factor

To calculate the power factor, same procedure was used as mentioned in section 5.3. The data was extracted from Ansys and the power factor is then found from,

$$Powerfactor = \cos\left(\arctan\left(\frac{((\psi_{PM} + L_d \times i_d)\,/\,(L_q \times i_q) + (i_q/i_d))}{(\psi_{PM} + L_d \times i_d)\,/\,(L_q \times i_d) - 1}\right)\right) \tag{5.2}$$

Figure 5.5 shows power factor vs current angle. Even though the machine with and without triangular cutouts has high ψ_{PM}, due to low saliency ratio it achieves a low power factor. This indicates that the saliency ratio plays a high role on the power factor. Table 5.2 shows the power factor for all machines at base speed and at maximum current with optimized current angle.

Table 5.2: Power factor at maximum current and at an optimized current angle

Machine type	Power factor
Reference Machine	0.66
Machine without triangular cutouts	0.59
Machine with triangular cutouts	0.61

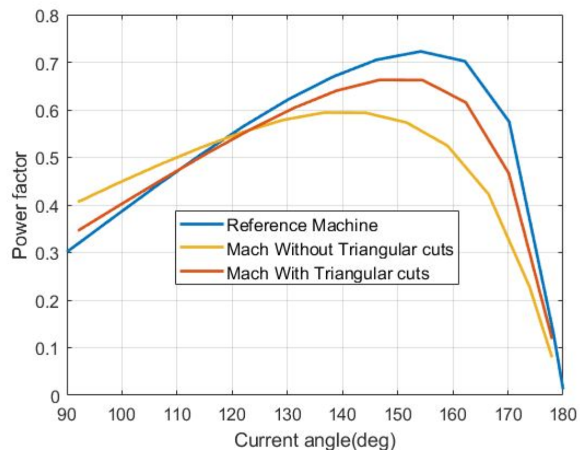

Figure 5.5: Power factor comparison

5.6 Control strategy

A control strategy was used for the spoke machine in order to operate in the most efficient point, to minimise losses while achieving the desired torque, and to evaluate the efficiency map of the machine. This control strategy consists of three parts:

1. Maximum Torque Per Ampere(MTPA) - current trajectory before the voltage limit is reached.

2. Field Weakening(FW) - current trajectory after the voltage limit is reached.

3. Maximum Torque Per Voltage(MTPV) - voltage ellipse shrinks inside the current circle in the high speed region.

To evaluate the control strategy, 11*11 operating points in the $i_d - i_q$ plane at different speed levels with sinusoidal current excitation for two electrical periods are considered. Through interpolation, the data resolution is increased in the $i_d - i_q$ plane, from which the MTPA, FW and MTPV region operating points are found through the fmincon function using MATLAB for the desired torque level within the allowed operating current and voltage limit. The control strategy of the machine without and with triangular cutouts are shown in Fig.5.6 and Fig.5.7 respectively.

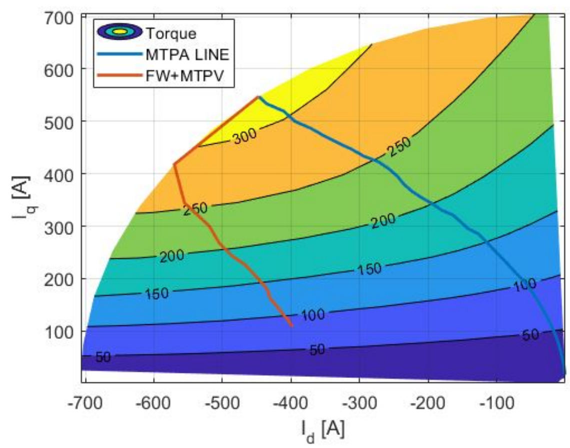

Figure 5.6: Control strategy- Machine without Triangular cutouts

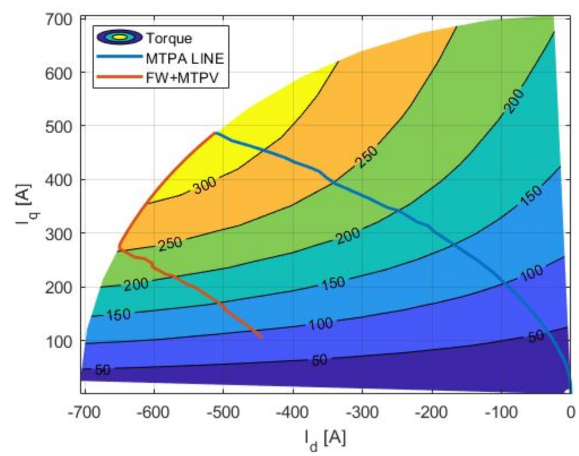

Figure 5.7: Control strategy- Machine with Triangular cutouts

The machine with triangular cutouts (Fig. 5.7) has a wider field weakening region compared to the machine without triangular cutouts, this is due to the saliency ratio. The machine with higher saliency ratio has a broad field weakening area, thanks to the fact that the ellipse can withstand higher speed range without entering the current circle (i.e. shrinking).

Table 5.3: Speed when maximum voltage is reached (base speed or speed at the end of MTPA) and when maximum current cannot be maintained (speed at the end of field weakening and the start of MTPV)

Machine type	Base Speed (rpm)	Speed when max current not reached (rpm)	Peak Torque (Nm)
Reference machine	4400	7400	350
Machine with Triangularcuts	4400	5800	330
Machine without Triangularcuts	4200	5700	315

5.7 Torque-speed characteristics

As previously said, the proposed spoke machine generates a lower torque when compared to the reference machine. Due to low power factor, the ferrite-based machine generates a low active power compare to our machine requirements. Figure 5.8 presents a max torque-power range for all machines for maximum current. The machine with triangular cutouts has a comparable active power to the reference machine thanks to comparably high saliency and power factor.

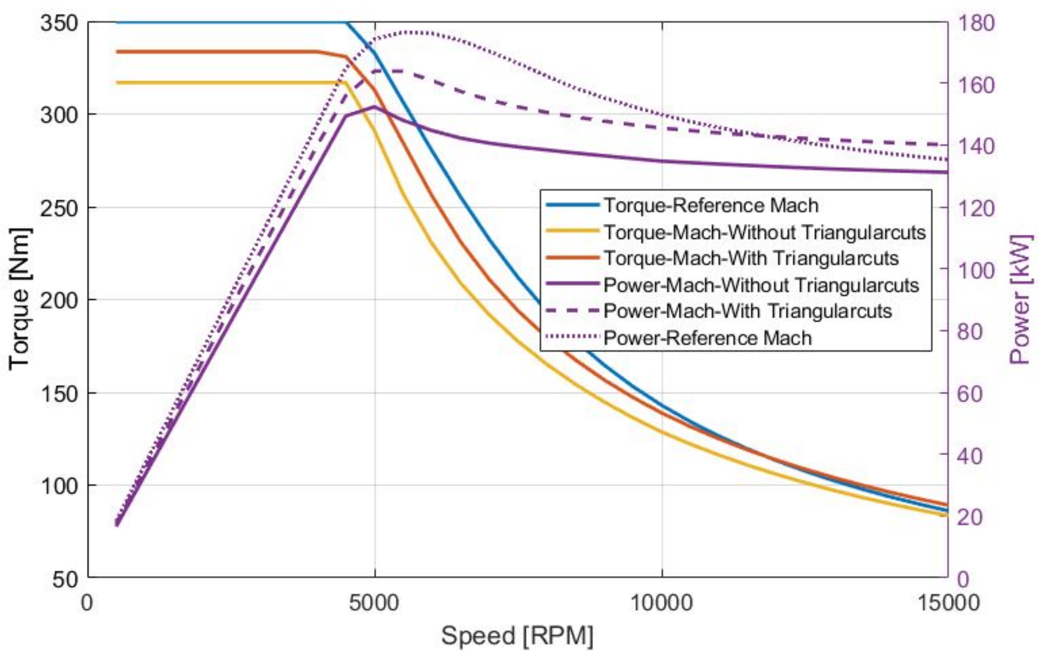

Figure 5.8: Torque-speed characteristics

5.8 Losses mapping

To evaluate the losses in the machines, they were determined in the entire torque-speed region as shown in Figure 5.9. Ansys simulations were conducted for all these points and the data for the core losses were collected. The material property is shown in Figure A.6. For conduction losses calculation, the magnitude of the winding resistance/phase was calculated. The value of resistance is mentioned in Table A.1, and by using (2.27), the conduction losses are calculated.

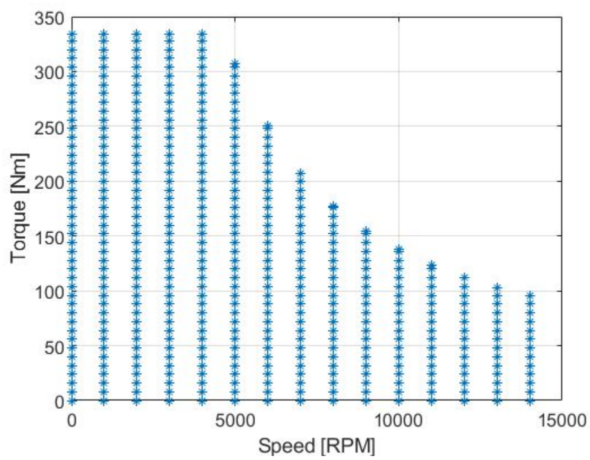

Figure 5.9: Points to run on Ansys Maxwell

Figure 5.10 and 5.11 present the total loss comparison for the machine without and with triangular cutouts, respectively. These machines were compared with the reference machine. In the contour plot, black lines indicate that the losses are same for both the machines. The loss in the region with low speed and higher torque i.e. the left side of the zero contour plots indicate that the proposed spoke ferrite-based machines has lower losses compared to the reference machine. On the other hand, the right side of the contour plot has negative values indicating that the reference machine has lower losses compared to the proposed spoke machine. We can see from Fig. 5.12 that the proposed spoke machine has higher conduction and core losses compared to the reference machine. They occur because the proposed spoke machine has higher PM flux linkage, so it needs more current to demagnetise it in the field weakening region, so conduction losses are quite high in this regions. More current also means more saturation of flux in the rotor thus further increasing core loss. In addition to that, large size magnets give more magnet losses, which will increase the core losses of the machine.

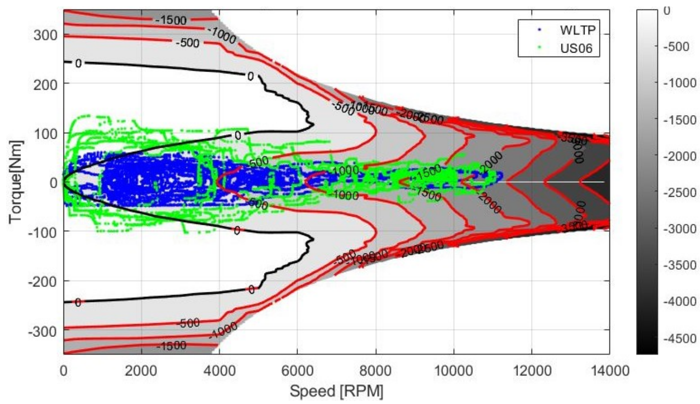

Figure 5.10: Total loss comparison (Reference machine minus Machine without triangular cutouts)

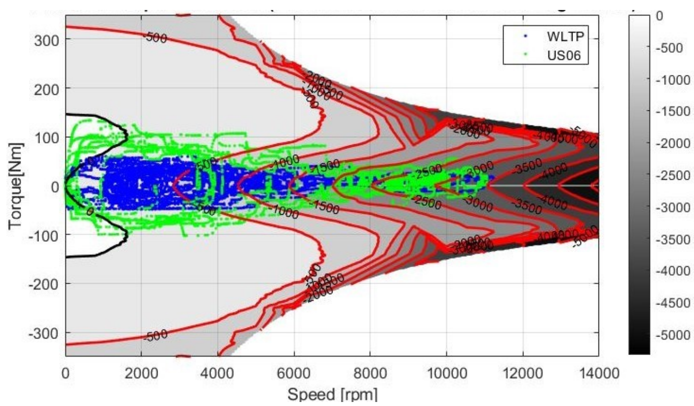

Figure 5.11: Total loss comparison (Reference machine minus Machine with triangular cutouts)

Figure 5.10 and 5.11 also present the working points of the EM in the WTLP and US06 drive cycle. Most of the working points fall on the negative side of the contour meaning that the reference machine has less energy loss compared to the proposed spoke machine. The machine without triangular cutouts has a little wider positive contour region when compared with the machine with triangular cutouts because it has a higher ψ_{PM}. Therefore, high ψ_{PM} requires a lower current in the low-speed and high-torque region and hence, less conduction losses occur.

The machine with triangular cuts has high core losses because the d axis path is restricted and it gets more saturated in the field weakening region. Hence core losses are higher for such machines. The conduction and core losses for all the machines are shown in Figure 5.12.

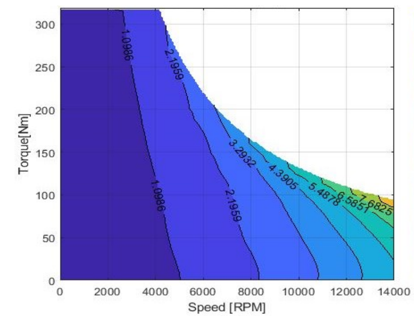

(a) Core loss for Machine without triangular cutouts

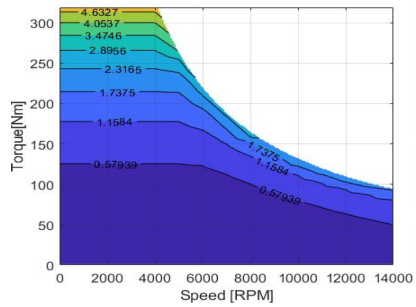

(b) Conduction loss for Machine without triangular cutouts

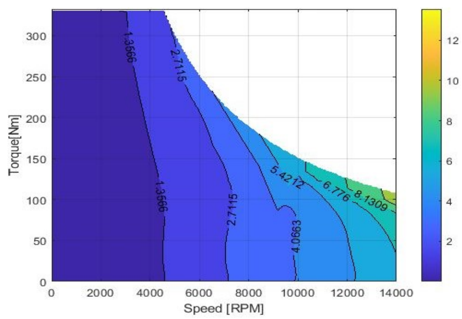

(c) Core loss for Machine with triangular cutouts

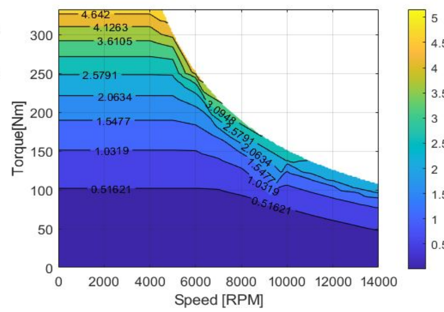

(d) Conduction loss for Machine with triangular cutouts

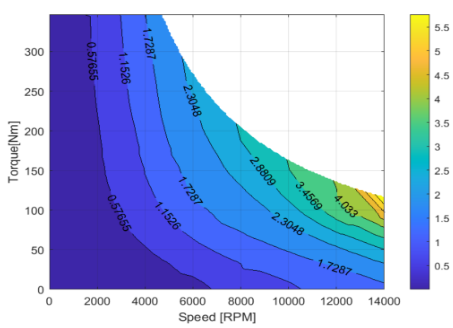

(e) Core loss for reference machine

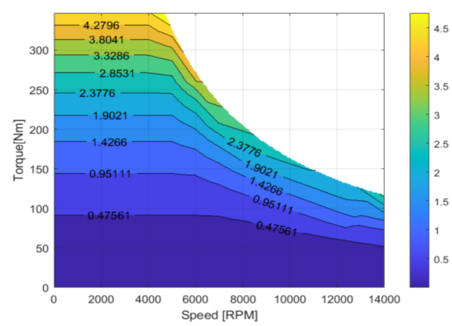

(f) Conduction loss for reference machine

Figure 5.12: conduction and Core losses for analysed machines

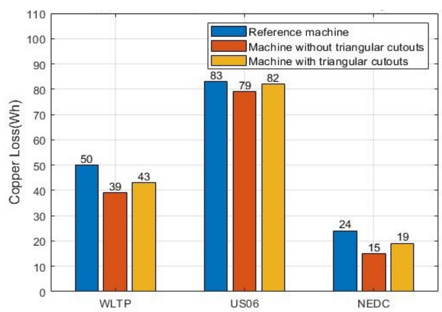

(a) Conduction loss for different drive cycle

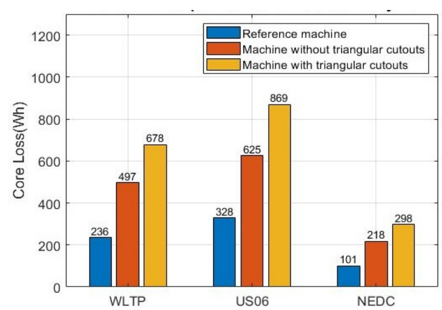

(b) Core loss for different drive cycle

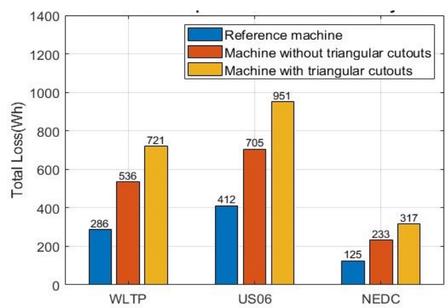

(c) Total loss for different drive cycle

Figure 5.13: EM performance for different drive cycle when only the rear EM is used

Figure 5.13 shows the conduction, core and total losses for different drive cycles when only the rear axle EM drive gets activated. As we can seen from Figure 5.13, the machine with triangular cutouts has higher losses because of the large size magnets and magnetic field saturation. Since the different drive cycles run for the different distances, the drive cycle losses/km for all machines were also shown in Fig.5.14.

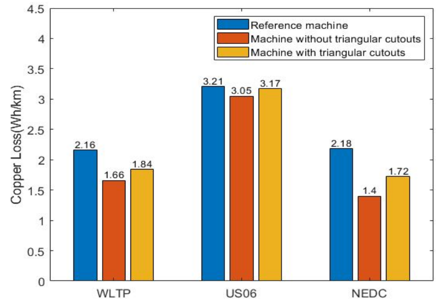

(a) Conduction loss for different drive cycle

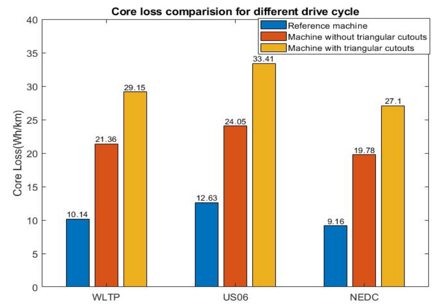

(b) Core loss for different drive cycle

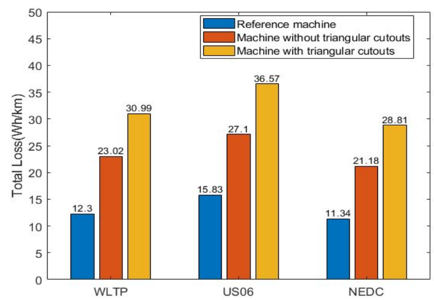

(c) Total loss for different drive cycle

Figure 5.14: EM losses per km for different drive cycle when only rear EM is used

5.9 Efficiency

Fig. 5.15 shows the efficiency map for different machines. The ferrite magnet based machines are generally better in the high speed region because of less core losses. Since the proposed spoke machine has higher loss as explained in section 5.8, the efficiency comparatively gets lower for these machines in drive cycle operating areas.

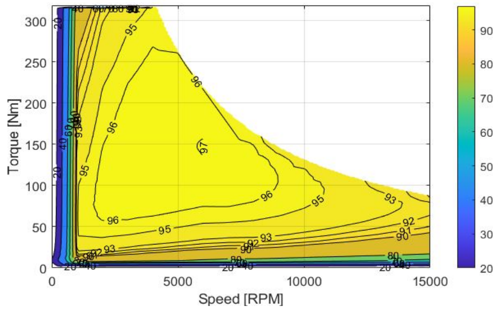

(a) Machine without triangular cutouts

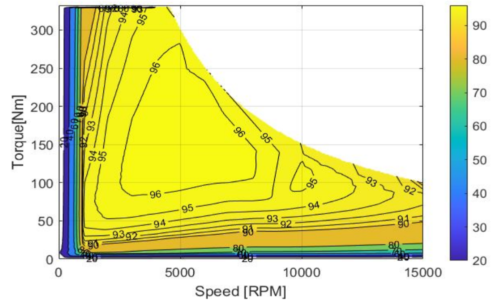

(b) Machine with triangular cutouts

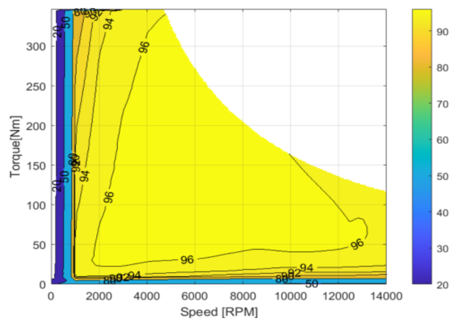

(c) Reference machine

Figure 5.15: Efficiency map

Table 5.4: Drive cycle efficiency for motoring mode

Drive Cycle	Machine without triangular cuts			Machine with triangular cuts			Reference machine		
	Mech energy (Wh)	Electri energy (Wh	Effici-ency	Mech energy (Wh)	Electrical energy (Wh)	Effici-ency	Mech energy (Wh)	Electrical energy (Wh)	Effici-ency
NEDC	1804	2053	0.88	1804	2129	0.85	1804	1957	0.92
US06	6375	7042	0.91	6375	7249	0.9	6375	6758	0.94
WLTP	4386	4922	0.89	4386	5078	0.86	4386	4658	0.94

Table 5.5: Drive cycle efficiency for generating mode

Drive Cycle	Machine without triangular cuts			Machine with triangular cuts			Reference machine		
	Mech energy (Wh)	Electrical energy (Wh)	Effici-ency	Mech energy (Wh)	Electrical energy (Wh)	Effici-ency	Mech energy (Wh)	Electrical energy (Wh)	Effici-ency
NEDC	589	544	0.92	589	534	0.91	589	552	0.94
US06	2026	1885	0.93	2026	1856	0.92	2026	1918	0.95
WLTP	1343	1278	0.95	1343	1275	0.95	1343	1269	0.95

As seen from Table 5.4, the drive cycle efficiency was calculated when only the rear axle wheel drive was activated. The torque and power demanded by the vehicle from the rear axle electrical machine is presented in Fig 4.24. The proposed spoke machine has substantially low drive cycle efficiency because of higher amounts of core and conduction losses. To improve the performance, the rotor structure should have been altered to reduce the magnetic field saturation. Other possibilities would be to use different types of steel material, reduced teeth width, etc.

5.10 Vehicle performance

Figure 5.16 presents the performance results for different machines. The proposed spoke machine was built on the requirements which are mentioned in Table 3.1. A constant acceleration of 12 m/s^2 was demanded from the vehicle and the performance was based on max torque-speed region. It should be noted that the two electric machine of equal rating were used at front and rear axle respectively.

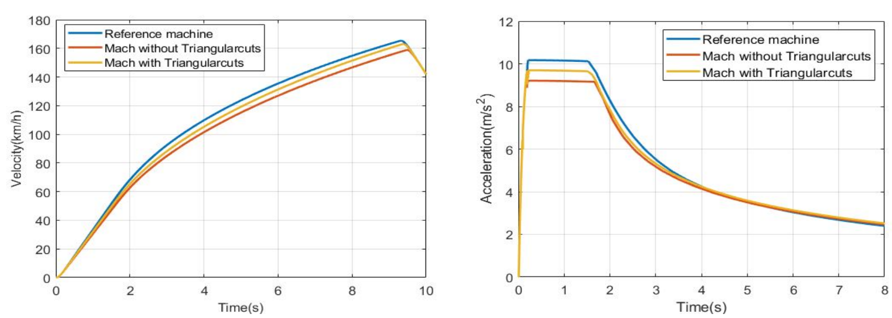

(a) Velocity profile of the vehicle for different machines

(b) Acceleration profile of the vehicle for different machines

Figure 5.16: Performance of the vehicle

5.11 Demagnetisation

As discussed in Chapter 3.4, the ferrite magnets are very sensitive at a low temperature. Hence, care should be taken to protect the magnets from demagnetisation during the normal and adverse operating condition of the machine. Fig.5.17 present the demagnetization curve of NMF12G ferrite magnet at minimum temperature of $-40°C$ which is used for investigation of irreversible demagnetisation.

When the flux density of a ferrite magnet is lower than the critical flux density at the knee of the demagnetization curve, irreversible demagnetisation will occur in the magnets. The knee point of flux density of the magnet is 0.035 T and it has a coercivity of $-350\ kA/m$. This demagnetisation will happen at severe condition, i.e. if a short circuit occurs at very low temperature or a fault happens in the DC bus system or power supply system. This current is mainly directed towards the d-axis of the magnet in the direction opposite to the magnets magnetisation direction. This irreversible demagnetisation will reduce the performance of the machine.

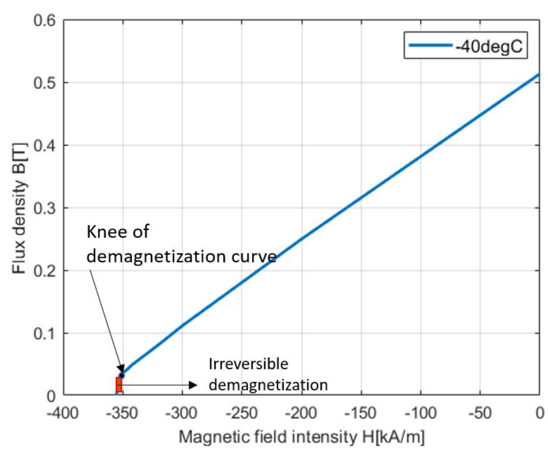

Figure 5.17: Demagnetisation curve of ferrite magnet(NMF12G) at $-40°C$

To perform the short circuit analysis study in Ansys, the coils are excited with zero voltage and with an initial phase current (value of the current just before short circuit occurred). Alternatively, using the MATLAB ODE solver for calculating short circuit current, the d-axis and the q-axis voltage can be set to zero. The transient short circuit current can be estimated using

$$\begin{aligned} R_s i_d + \frac{d\psi_d}{dt} - w\psi_q = 0 \\ R_s i_q + \frac{d\psi_q}{dt} - w\psi_d = 0 \end{aligned} \tag{5.3}$$

where R_s is the stator resistance, ψ_d is the d-axis flux linkage, ψ_q is the q axis flux linkage, and w is the electrical speed.

To visualise the demagnetisation effects, the calculated transient currents were used in Ansys using design dataset tool, but this method doesn't take the transient inductance value into account.

For both the methods, maximum short circuit current occurred at the end of the MTPA and beginning of the field weakening region for both the proposed spoke machines (see Fig. 5.18).

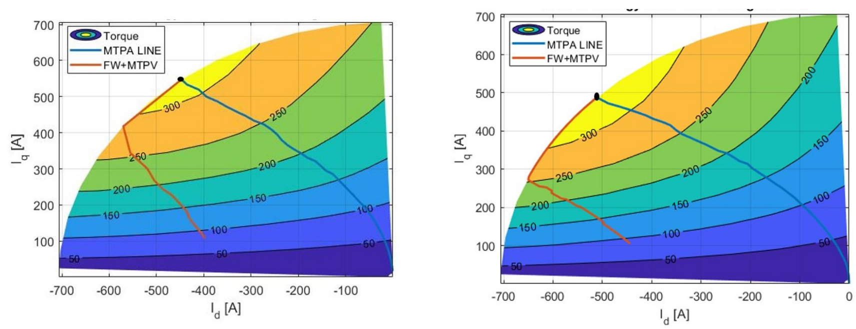

(a) Maximum short-circuit current point for the machine without triangular cutouts

(b) Maximum short-circuit current point for the machine with triangular cutouts

Figure 5.18: Maximum short-circuit current point in the dq contour

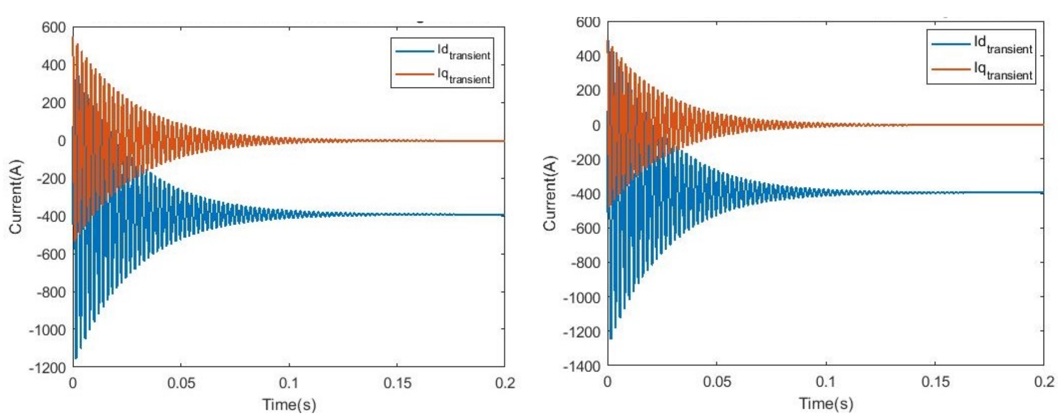

(a) Transient short-circuit current for the machine without triangular cutouts

(b) Transient short-circuit current for the machine with triangular cutouts

Figure 5.19: Transient short-circuit current

From Figure 5.19, it can be seen that the peak negative $d-axis$ current occurs at 2.8 ms for both the machines. From the graph, we can see that the peak negative d-axis current(i_d) for the machine without triangular cutouts and with cutouts occurs at around 1200 A and 1100 A respectively. Figure 5.20 shows the irreversible demagnetisation of the magnets at peak negative d-axis current and at a base speed of 4400 rpm. The range of the magnetic flux density is shown between 0-0.04 T in Figure 5.20 and the black circle shows where the magnets are demagnetised and it was verified from Figure 5.21. Figure 5.21 shows that vector plot of magnetic flux density where the arrow get reversed indicating that the magnets are irreversibly demagnetised. It is briefly explained in section 2.7.

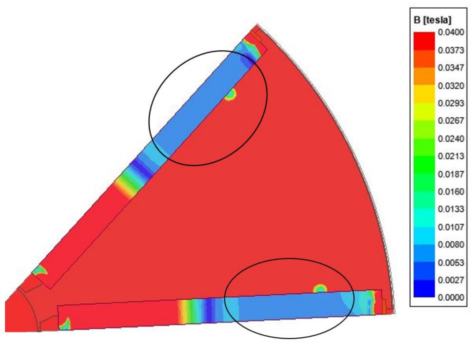

(a) Demagnetisation of the machine without triangular cutouts at $-40°C$magnet temperature

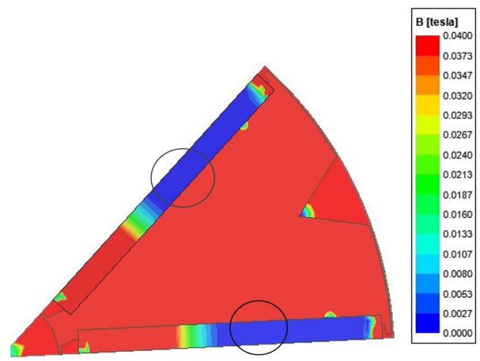

(b) Demagnetisation of the machine with triangular cutouts at $-40°C$ magnet temperature

Figure 5.20: Demagnetisation of the machines at its highest possible $d\ axis$ current magnitude for $-40°C$ magnet temperature

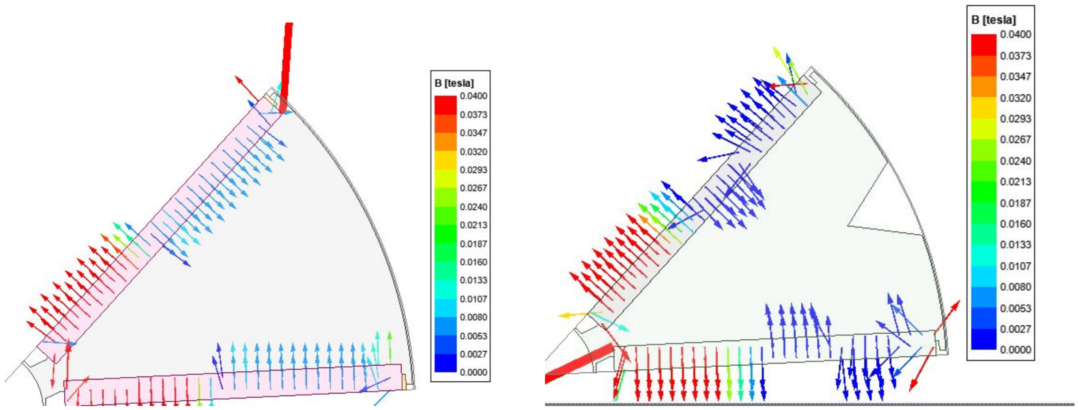

(a) Demagnetisation of the machine without triangular cutouts at $-40°C$magnet temperature

(b) Demagnetisation of the machine with triangular cutouts at $-40°C$ magnet temperature

Figure 5.21: Vector plot for magnetic flux density at its highest possible $d\ axis$ current magnitude for $-40°C$ magnet temperature

As observed from the magnets, half of the magnet is completely demagnetised at this transient current for both the machines. By lowering the d axis current step by step, to check when the demagnetisation starts in the magnet. Figure 5.22 shows that the magnet started to demagnetise at 890 A for the machine with triangular cutouts and at 920 A for the machine without triangular cutouts. In order to find the safe operating points for both the machines, Figure 5.23-5.24 shows the unsafe operating points, where the machines should never be short circuited, otherwise it will lead to demagnetisation of the magnets where it can be in the risk zone.

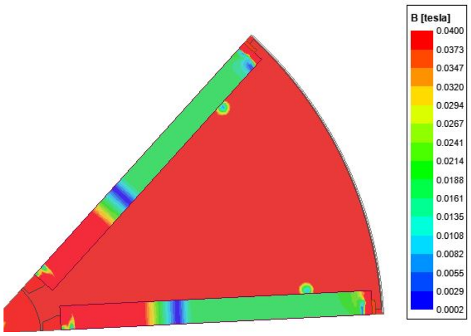

(a) Demagnetisation of the machine without triangular cutouts starts at 920 A investigate at $-40°C$magnet temperature

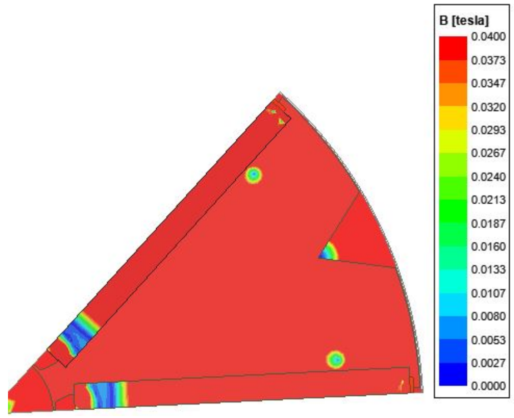

(b) Demagnetisation of the machine with triangular cutouts starts at 890 A investigate at $-40°C$ magnet temperature

Figure 5.22: Demagnetisation of the machines at its highest possible d $axis$ current magnitude for $-40°C$ magnet temperature

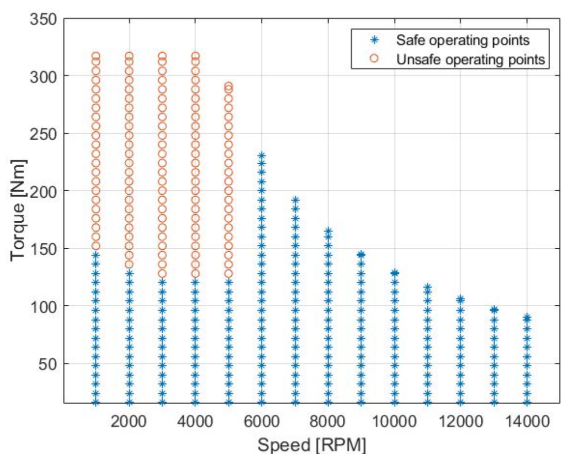

Figure 5.23: Safe and unsafe operating point in the torque-speed region for demagnetisation of the magnets of the machine without triangular cutouts at -40°C

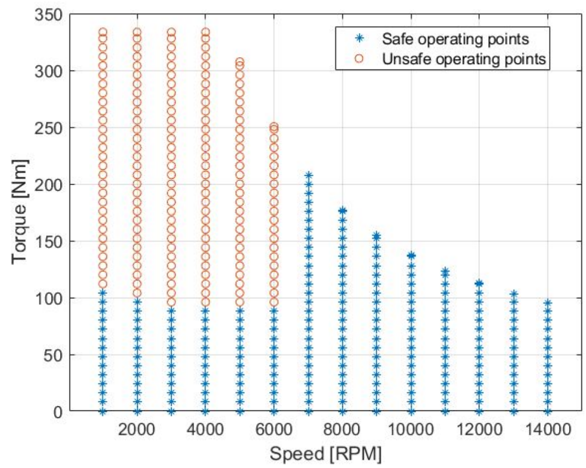

Figure 5.24: Safe and unsafe operating point in the torque-speed region for demagnetisation of the magnets of the machine with triangular cutouts at $-40°C$

In order to reduce the risk of irreversible demagnetisation in the spoke machine at low temperature and to increase the safe operating points, the rotor structure of the spoke machine was moderated by increasing the non magnetic material thereby decreasing the magnet size. Due to this, the overall performance of machine was decreased.

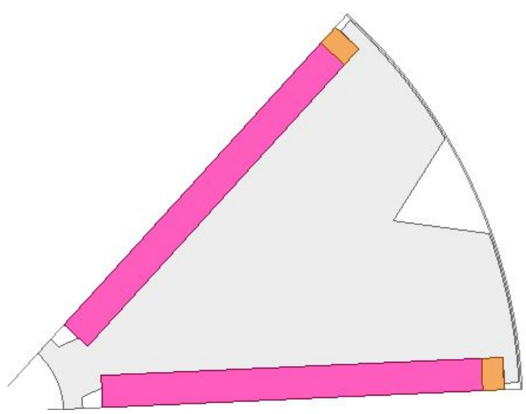

Figure 5.25: Modified machine with triangular cutouts after considering demagnetisation

As seen from Figure 5.25, the moderated spoke machine has the non magnetic material size increased to 4 mm for the initial analysis and the magnet width is reduced from 65 mm to 62 mm. As mentioned in section 3.7.1.1, the non magnetic material protect the magnet in field weakening area. Now, the machine could be able to withstand more short circuit current and the safe operating point is also extended (see Fig. 5.26). To compensate the performance loss we can scale the machine. In order to optimise the rotor for protection against demagnetisation, the parametric analysis might be conducted for entire rotor structure because in this thesis only the length and the width of the magnets are parametrised.

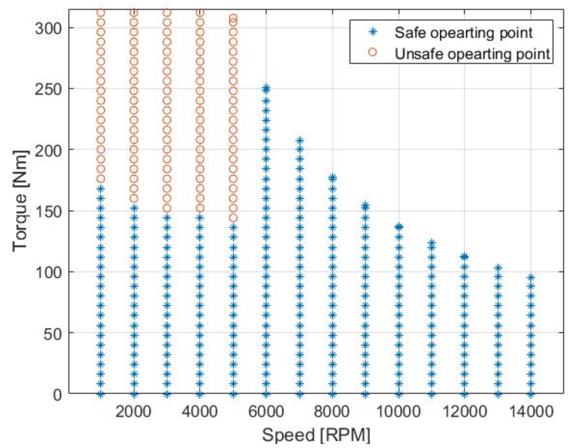

Figure 5.26: Safe and unsafe operating point in the torque-speed region for demagnetisation of the magnets of the modified machine with triangular cutouts at $-40°C$

5.12 Mechanical Integrity

The proposed spoke machine has a maximum speed of 14000 rpm. Due to large size of the magnet, it will be expected to experience more stress. As per suggestion from mechanical design experts, one way to reduce the stress is by increasing the rib length of the spoke machine to handle large stress at top speed. The rib length should be increased to 3-4 mm in both places towards the air gap and near to the shaft.

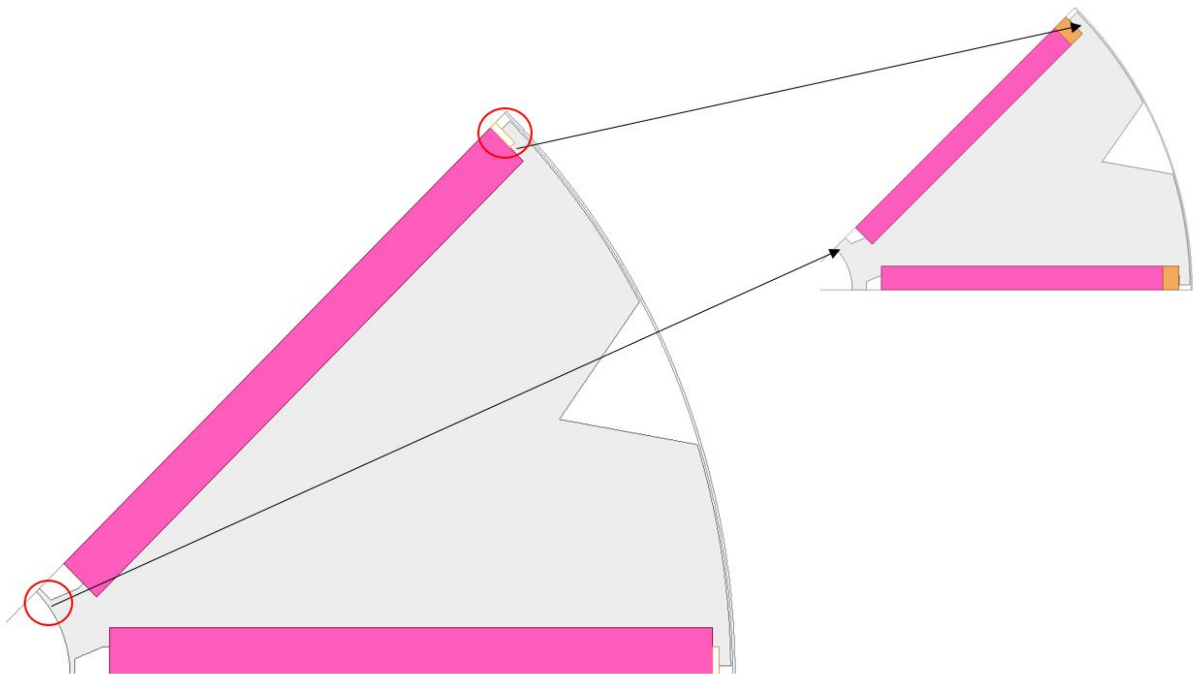

Figure 5.27: Risk zone in mechanical integrity point of view

Figure 5.27 shows that the risk zone for the mechanical stress region and altered spoke machine to handle the stress. This will affect the overall performance of the machine due to the reduction in size of the magnet.

6

Magnet cost estimation and environmental impact

6.1 Magnet cost estimation

The price of both neodymium based rare earth magnets as well as Sr-ferrite based magnets has become very volatile. The price of rare earth magnet is specifically controlled by China. The magnets used in this thesis are mentioned in Table 3.3 and the price of those magnets was difficult to obtain. Alternatively, magnets similar to the one used in Table 3.3 were found and a magnet supplier [16] was contacted for possible magnet price based on mass production of the machine. The property of new magnets for the purpose of price comparison is shown in Table 6.1

Table 6.1: Property of new magnets

S.No.	Name	Provider	Remanence flux density(T)	Coercivity (kA/m)
1	JPM-6N	Compotech	0.45	270
2	JPM-4A	Compotech	0.38	270
3	N40EH	Compotech	1.25	915

The property of the chosen magnet for price comparison is inferior when compared with the magnets in Table 3.3 but it is good enough to find a rough estimate of the magnet price for the reference, arc shape and spoke machine. JPM-6N is comparable with the NMF-12G magnet, JPM-4A is comparable with the Y30BH magnet, and N40EH is comparable with the Nd-Fe-B magnet by Hitachi. The price of these magnets are shown in Table 6.2.

As observed from Table 6.2 the cost of the magnets for the reference machine is more than that of the ferrite based machines. Since the 4-layer machine has more number of magnets in each pole than the spoke machine, the manufacturing cost of the magnets are high for the 4-layer machine. It was shown in [11] that the cost of core and winding is almost similar for a neodymium and ferrite based machine and major cost difference

Table 6.2: Magnet price comparison

Magnet price per rotor(euro)				
Machine Type	Mass (Kg)	N40EH	Y30BH	NMF12G
Spoke machine	4.1	-	50	86
4- layer arc machine	4.6	-	65	123
Reference machine	3.9	603	-	-

comes from the magnet price.

6.2 Environmental impact

Rare earth magnets are essential for electric and hybrid vehicles, solar and wind energy, etc. Around 20% of the rare earth magnets are used for motors and generators [17].

Rare earth magnets consists of neodymium(Nd), prase odymium (Pr), and dysprosium (Dy). The pollution from rare earth mining has created soil erosion, water contamination, and radioactive waste. The extraction of rare earth magnets from magnets causes sulfidic waste. According to china water risk, the clean-up process of mining is very expensive and time consuming it would take 100 years for the environment to recover [11].

According to an industry watch dog organization, China Water Risk, the mining of just one ton of rare earth metals in the country produces as much as 2.1 million cubic feet of waste gas which contains dust, sulfuric and hydro fluoric acid, 7,000 cubic feet of sewage water containing acid, and over a ton of radio active waste. These chemicals would result in climate change and environmental disaster [18].

Ferrite magnets have the chemical composition of Fe_2O_3 and SrO. About 84-91% of the ferrite magnet is Fe_2O_3 while 7.5-10.5 % is SrO [16]. These minerals are much better than the rare earth magnets from an environmental point of view. The amount of CO_2 produced during magnet production is $0.32g\ CO_2\ eq./km$ for $Nd(Dy)FeB$ magnet while it is $0.15g\ CO_2\ eq./km$ for a Sr-ferrite magnet [19]. It is also true that the toxic waste and resource depletion for a machine produced using ferrite magnet is lower than that of the rare earth magnet. It is also possible to recycle ferrite magnets with magnetic properties superior than the property of new ferrite magnets [20].

The induction machine is also one of the choices for EVs but it holds mainly copper. Copper production causes toxic emissions, and the most toxic metals are emitted from the industries and directed into natural water system. High use of copper in electric motors increase the sulfide disposal from material production stage [11].

It is theoretically possible to replace a large part of today's fossil fueled vehicles with EVs in the future. This has a potential to help reduce the global CO_2 emissions and help to slow down the global warming if the electricity is produced in a sustainable manner. Issues such as pollution and climate change have caused people to concern more about environmental impacts.

7

Conclusion

This thesis presents the comparison of a PMSM using NdFeB magnets or ferrite magnets. They are compared in terms of torque, power, efficiency and losses. The proposed different types of structures such as arc and spoke are compared with the reference machine. Irreversible demagnetisation of the ferrite magnet at low temperature in adverse condition is visualised and mechanical integrity at top speed is investigated.

7.1 ARC type configuration

First, the ARC type configuration was analysed in two different shapes i.e. in a 4-layer and 3-layer configuration. The 4-layer machine was able to fulfill the torque requirement when compared to the reference machine. This was possible thanks to the extra amount of magnets that were added in the 4-layer machine. The torque-speed characteristics obtained for different machines indicate that the 4-layer machine produce more active power for the same amount of apparent power in the field weakening region. High power factor for the 4-layer machine when compared with the other machines also support the previous statement. Hence a 4-layer machine will require an inverter whose apparent power rating is low. To obtain high power factor, the saliency ratio and PM flux linkage plays an important role.

It was noticed from the final parametric study that the 4^{th} layer of a 4-layer machine is most important in order to increase the saliency ratio and power factor. The drive cycle losses shows that the loss for the 3-layer machine is lower than for the other machines. This is due to the low PM flux linkage. Low PM flux linkage contributes to lower core losses which are the dominant losses in an electrical machine. The demagnetisation of the machine under short-circuit condition was also studied. It was found that the ferrite machine is most sensitive to demagnetisation at low temperature. Under these circumstances, to avoid demagnetisation, these machines can only be operated at certain zones in the torque-speed region known as the safe zone. Primary study regarding the mechanical integrity of the 4-layer machine shows that to be able to reach a similar performance requirement as the reference machine, the volume of the 4-layer machine needs to be greater than that of the reference machine.

7.2 Spoke type configuration

In this thesis, two different rotor structure of the spoke type configuration are discussed. The proposed spoke machines are compared with the reference machine, and their performance parameters such as total torque especially reluctance torque, saliency ratio, power factor, etc. are inferior to that of the reference machine. In order to meet the performance requirement, the spoke machine has to be scaled in the axial direction. In particular, the proposed spoke machine can generate more magnet torque due to large size magnets and it has higher ψ_{PM}. The machine without triangular cutouts is designed as a basic spoke type PMSM that maximally utilizes magnetic torque. The machine with triangular cutouts is designed to actively utilize the reluctance torque. An Ansys simulation indicates that the machine with triangular cutouts has superior characteristics compared to the machine without cuts in terms of total torque, saliency ratio, and power factor and control strategy. The machine without triangular cutouts has lower drive cycle losses compared to the machine with cuts due to flux saturation in the d axis direction and therefore, the efficiency is higher. In order to reduce the risk of demagnetisation, the rotor structure of the spoke machine is moderated by increasing non magnetic material and it can withstand high short circuit current at a low temperature.

7.3 Cost and sustainability aspects

The analysis regarding the cost of the magnets and its environmental impact shows that the ferrite based machine is cheaper to produce as well as its more sustainable. If the volume of installation of the EM is of little concern, neodymium based machines can be easily replaced by ferrite based machines.

7.4 Future work

Some of the aspects that can be studied in future are,

- A more rigorous parametric sweep of the arc shape machine can be done to optimise the rotor design.
- The rotor of the proposed spoke type configurations can be optimised to reduce drive cycle losses and steps should be taken to increase the drive cycle efficiency.
- Different stator winding configuration can be tried out to reduce the amount of copper and to increase the copper fill factor.
- Thermal analysis and mechanical integrity can be investigated for both the arc and spoke type configuration.

- Care should be taken to prevent the magnets from irreversible demagnetisation by moderating the rotor structure.

Bibliography

[1] Xiping Liu, Ya Li, Zhangqi Liu, Tao Ling, and Zhenhua Luo. Optimized design of a high-power-density pm-assisted synchronous reluctance machine with ferrite magnets for electric vehicles. *Archives of Electrical Engineering*, 66(2), 2017.

[2] Ilya Petrov and Juha Pyrhonen. Performance of low-cost permanent magnet material in pm synchronous machines. *IEEE Transactions on Industrial Electronics*, 60(6):2131–2138, 2012.

[3] Viktor Briggner. Design and comparison of pmasynrm versus pmsm for pumping applications, 2018.

[4] Thomas A Lipo. *Introduction to AC machine design*. John Wiley & Sons, 2017.

[5] S Tizianel and N Novello. Permanent magnet demagnetization process considering the inclination of the demag field. *IEEE Transactions on Magnetics*, 52(8):1–7, 2016.

[6] Emma Arfa Grunditz and Torbjörn Thiringer. Modelling and scaling procedure of a vehicle electric drive system. *Report, Chalmers University of Technology, Sweden, url: https://research. chalmers. se/en/publication*, 2017.

[7] Xc40. *Retrieved from: `https://www.auto-data.net/en/volvo-xc40-recharge-p8-78-kwh-408hp-awd-electric-37882` [2020-10-20]*.

[8] Elisabet Jansson, Emma Grunditz, and Torbjörn Thiringer. Impact of saturation and scaling on the field weakening performance of an interior pm machine. In *2020 International Conference on Electrical Machines (ICEM)*, volume 1, pages 1136–1142. IEEE, 2020.

[9] Haiwei Cai, Bo Guan, and Longya Xu. Low-cost ferrite pm-assisted synchronous reluctance machine for electric vehicles. *IEEE Transactions on Industrial Electronics*, 61(10):5741–5748, 2014.

[10] MN Ibrahim, Peter Sergeant, and EM Rashad. Influence of rotor flux-barrier geometry on torque and torque ripple of permanent-magnet-assisted synchronous

reluctance motors. In *2016 XXII International Conference on Electrical Machines (ICEM)*, pages 398–404. IEEE, 2016.

[11] Emma Arfa Grunditz, Sonja Tidblad Lundmark, Mikael Alatalo, Torbjörn Thiringer, and Anders Nordelöf. Three traction motors with different magnet materials—influence on cost, losses, vehicle performance, energy use and environmental impact. In *2018 Thirteenth International Conference on Ecological Vehicles and Renewable Energies (EVER)*, pages 1–13. IEEE, 2018.

[12] Wataru Kakihara, Masatsugu Takemoto, and Satoshi Ogasawara. Rotor structure in 50 kw spoke-type interior permanent magnet synchronous motor with ferrite permanent magnets for automotive applications. In *2013 IEEE Energy Conversion Congress and Exposition*, pages 606–613. IEEE, 2013.

[13] BOGDAN DUMITRU VĂRĂTICEANU, Paul Minciunescu, and Constantin Nicolescu. Performance comparison between surface, spoke and interior permanent magnet machines designed for traction applications. *Rev. Roum. Sci. Techn.–Électrotechn. et Énerg*, 61(1):3–7.

[14] Keun-Young Yoon and Soo-Whang Baek. Performance improvement of concentrated-flux type ipm pmsm motor with flared-shape magnet arrangement. *Applied Sciences*, 10(17):6061, 2020.

[15] Chao-hui Zhao, Shui-liang Li, and Yang-guang Yan. Influence factor analysis of pmsm air gap flux density. In *2005 International Conference on Electrical Machines and Systems*, volume 1, pages 334–339. IEEE, 2005.

[16] Compotech provider AB Rundbom Per. Certificate of material, 2018.

[17] Lorraine Chaffer et al. Case study: Rare earth elements (ree). *Geography Bulletin*, (HSC Special Issue 1 2020):26, 2020.

[18] Tekedil Zeenat Humsa and RK Srivastava. Impact of rare earth mining and processing on soil and water environment at chavara, kollam, kerala: a case study. *Procedia earth and planetary science*, 11:566–581, 2015.

[19] Anders Nordelöf, Emma Grunditz, Sonja Lundmark, Anne-Marie Tillman, Mikael Alatalo, and Torbjörn Thiringer. Life cycle assessment of permanent magnet electric traction motors. *Transportation Research Part D: Transport and Environment*, 67:263–274, 2019.

[20] Alberto Bollero, Javier Rial, Melek Villanueva, Karol M Golasinski, Ana Seoane, Judit Almunia, and Ricardo Altimira. Recycling of strontium ferrite waste in a permanent magnet manufacturing plant. *ACS Sustainable Chemistry & Engineering*, 5(4):3243–3249, 2017.

A

Appendix A

A.1 XC40 simulink model

This section contains simulink model used for the drive cycle analysis.

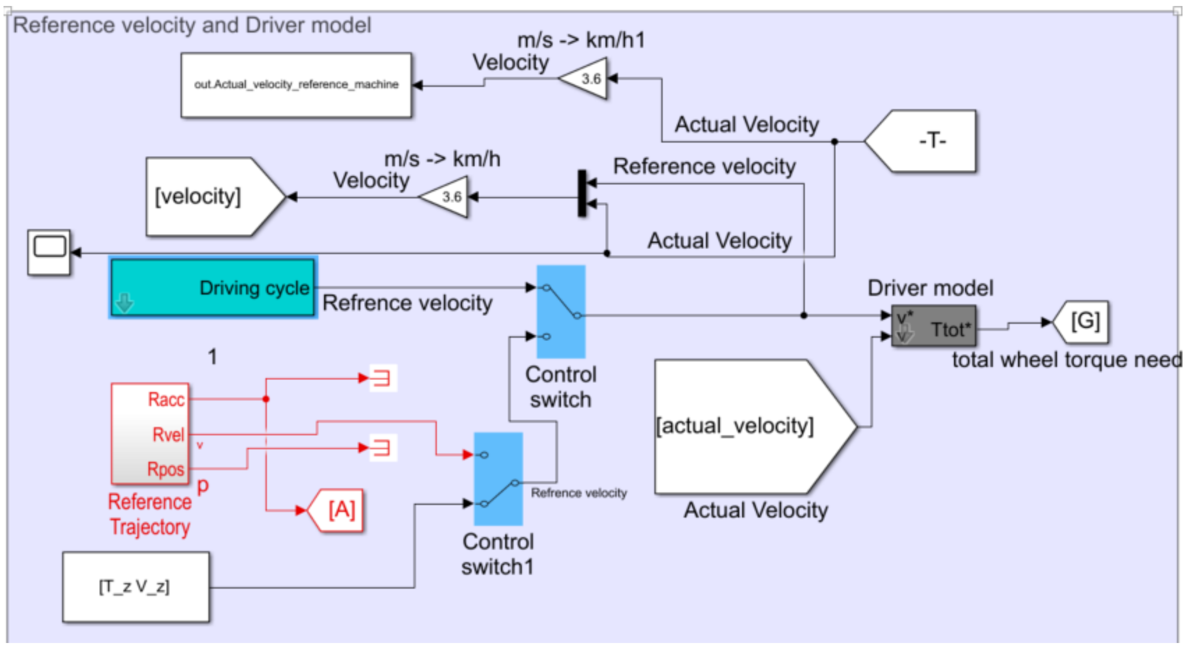

Figure A.1: Reference velocity and driver model

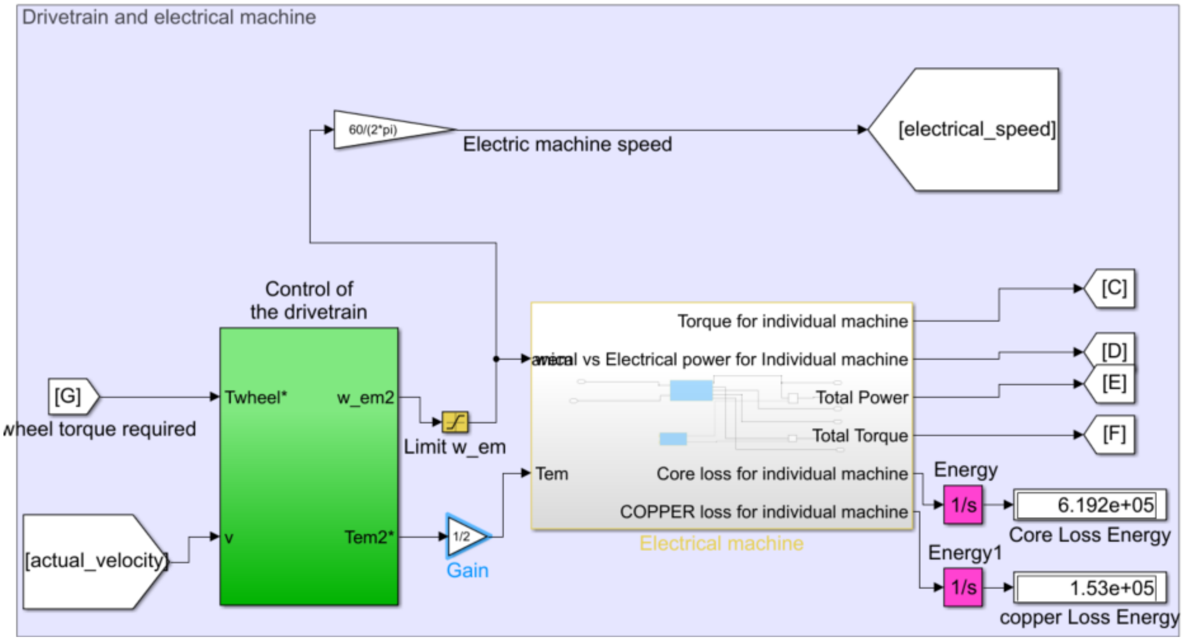

Figure A.2: Drive train and electrical machine model

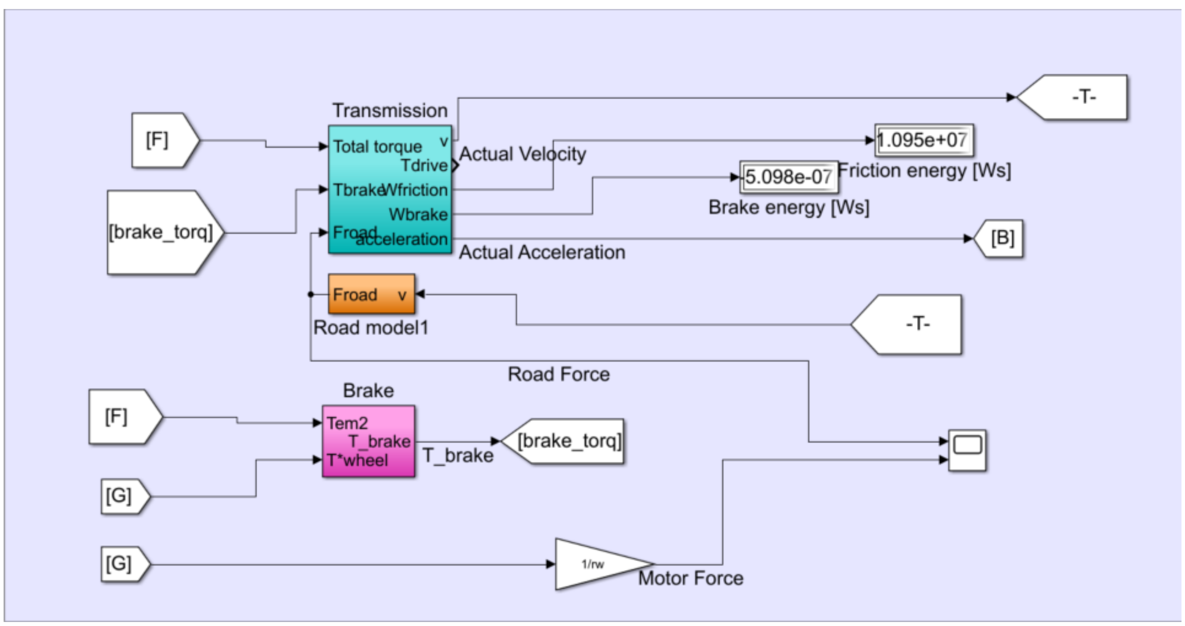

Figure A.3: Transmission and road force model

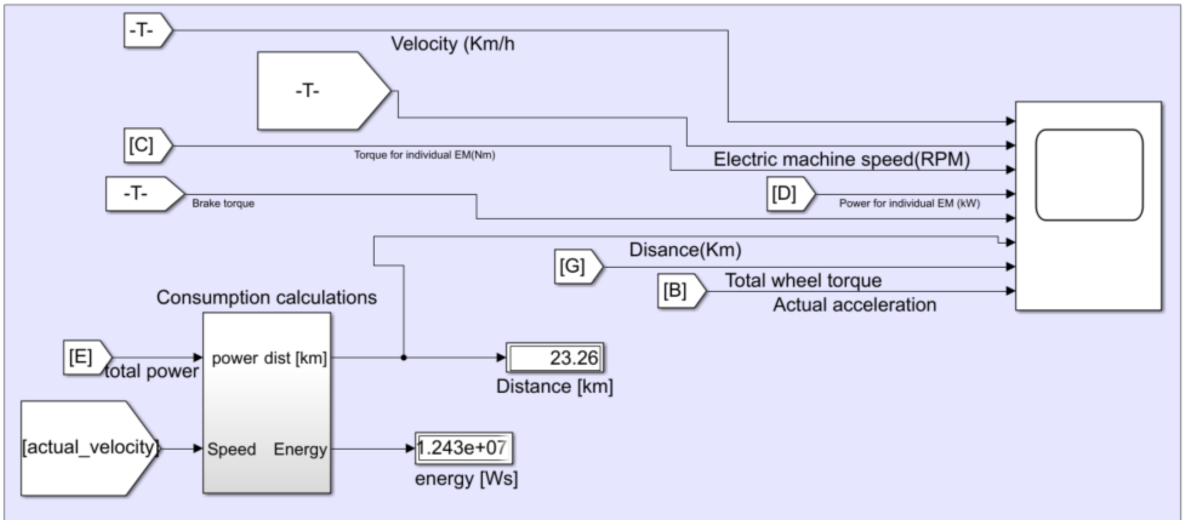

Figure A.4: Results

A.2 Stator parameter

This section contains stator parameter of the machine.

Table A.1: Stator Parameters

Stator Parameters	**Value**
Stator Outer Diameter	252 mm
Stator Inner Diameter	169.3 mm
Winding Type	Double layer distributed winding
Number of poles	8
No of stator slots /pole/phase	2
Fill factor	0.45
Total number of stator slots	48
Current loading	120 kA/m
Current density	20*10ˆ6 A/mˆ2
Tooth Width	7.01 mm
Slot opening width	5.7277 mm
Area of slot	1.56e-04 mˆ2
Area of coil	3.5e-05 mˆ2
Area of each copper conductor	8.75e-06 mˆ2
Winding resistance	0.0064 Ohm
Coil Pitch	6
Pole Pitch	7
Winding Pitch factor	1
Distribution factor	0.9417
Stack length	162 mm
No. of turns per coil	4
No. of parallel path	4
Air gap length	1 mm

A.3 Demagnetisation

This section contains results from the demagnetisation study of the machine.

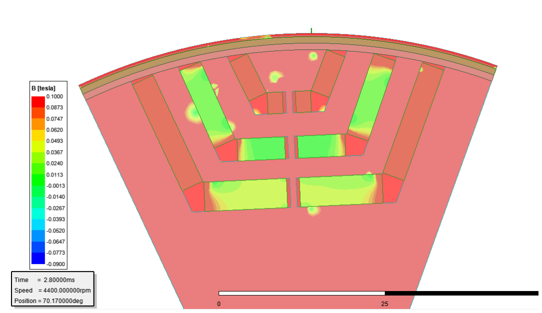

(a) Demagnetisation of 3 layer machine at -1230 A of d axis current and 20 °C magnet temp

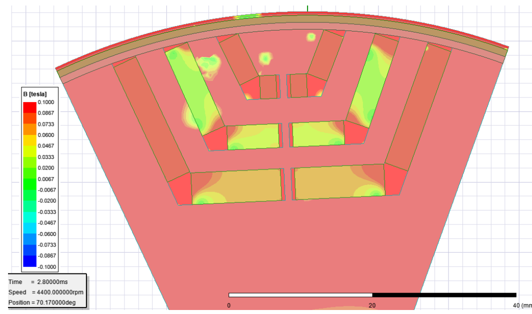

(b) Demagnetisation of 3 layer machine at -1230 A of d axis current and 60 °C magnet temp

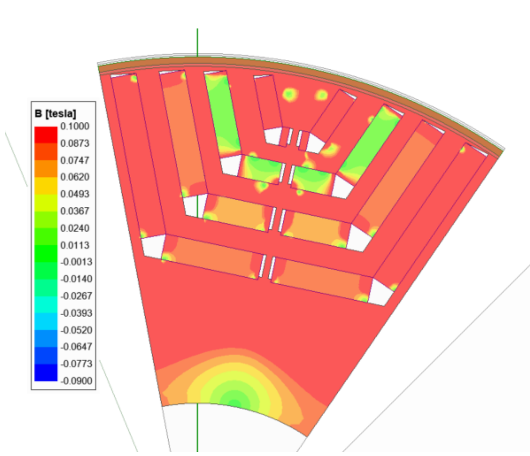

(c) Demagnetisation of 4 layer machine at -1500 A of d axis current and 20 °C magnet temp

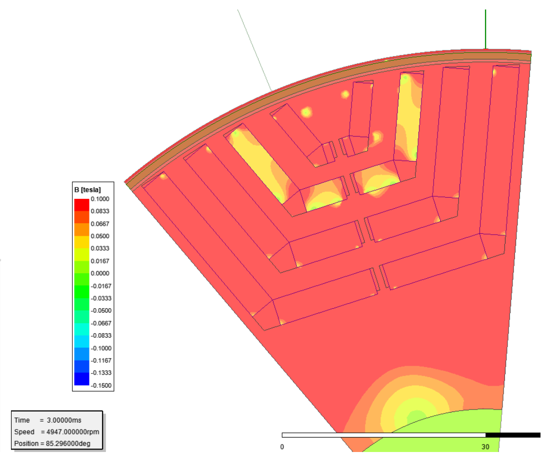

(d) Demagnetisation of 4 layer machine at -1500 A of d axis current and 60 °C magnet temp

Figure A.5: Demagnetisation of ferrite machines at different temperature for maximum possible negative d axis current

A.4 Material property

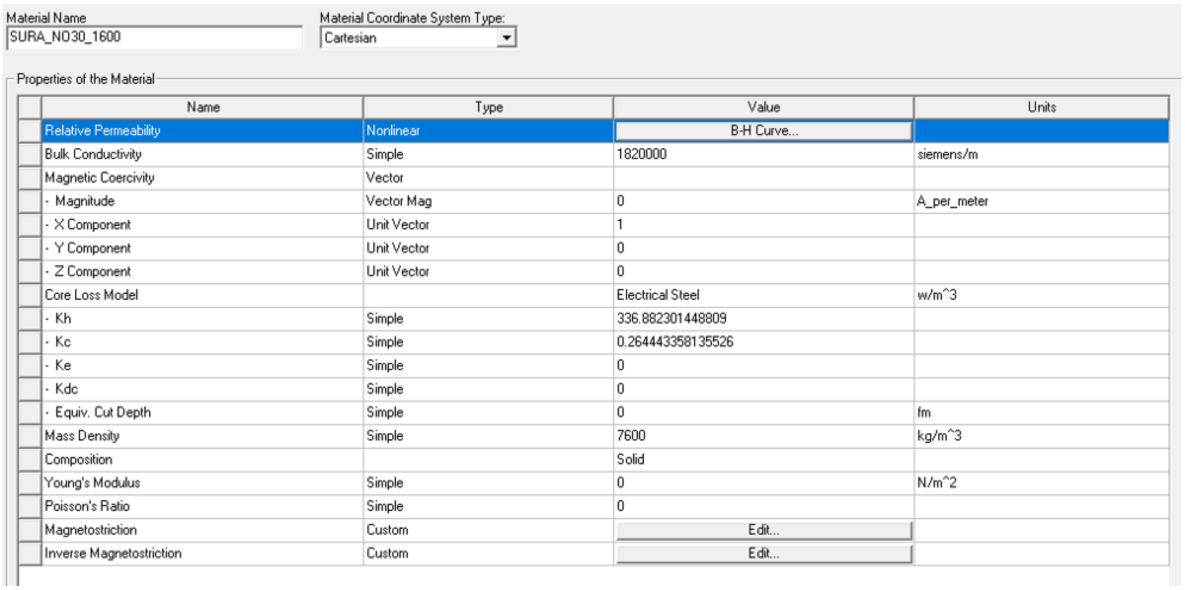

Material Name: SURA_NO30_1600

Material Coordinate System Type: Cartesian

Properties of the Material

Name	Type	Value	Units
Relative Permeability	Nonlinear	B-H Curve...	
Bulk Conductivity	Simple	1820000	siemens/m
Magnetic Coercivity	Vector		
- Magnitude	Vector Mag	0	A_per_meter
- X Component	Unit Vector	1	
- Y Component	Unit Vector	0	
- Z Component	Unit Vector	0	
Core Loss Model		Electrical Steel	w/m^3
- Kh	Simple	336.882301448809	
- Kc	Simple	0.264443358135526	
- Ke	Simple	0	
- Kdc	Simple	0	
- Equiv. Cut Depth	Simple	0	fm
Mass Density	Simple	7600	kg/m^3
Composition		Solid	
Young's Modulus	Simple	0	N/m^2
Poisson's Ratio	Simple	0	
Magnetostriction	Custom	Edit...	
Inverse Magnetostriction	Custom	Edit...	

Figure A.6: Property of steel lamination